Effects of Microstructure on Fracture Behavior of Hydrogenated Notched 4340 Steel: A Quantitative Study

by

Mobbassar Hassan Sk

A dissertation submitted to the Graduate Faculty of
Auburn University
in partial fulfillment of the
requirements for the Degree of
Doctor of Philosophy

Auburn, Alabama
May 4, 2014

Keywords: Hydrogen embrittlement of 4340 steel, prior austenitic grain size, martensitic hardness, intergranular fracture, quasi-cleavage, fracture behavior

Approved by

Ruel A. Overfelt, Chair, Professor of Mechanical Engineering
Jeffrey W. Fergus, Professor of Mechanical Engineering
Barton C. Prorok, Professor of Mechanical Engineering
Curtis Shannon, Professor of Chemistry & Biochemistry

Abstract

Hydrogen based fuel has been identified as a promising alternative to fossil fuel to reduce the emission of greenhouse gases and to enable sustainable energy supplies worldwide. In spite of such promising applications of hydrogen as a prime energy source, serious technical challenges exist due to metallurgical interactions of hydrogen with fracture sensitive metals and alloys. Atomic hydrogen can be generated at the surface of metals and alloys by thermal dissociation of gaseous diatomic hydrogen or by electrochemical decomposition of hydrogen bearing aqueous solutions and vapor condensates. Once inside hydrogen-sensitive materials, e.g., high strength steel, hydrogen atoms can interact with various microstructural features resulting in enhanced tendency for brittle fracture. The focus of this work was to study the embrittling effects of hydrogen on low alloy 4340 steel introduced from two different sources (i) vapor condensate of vaporized hydrogen peroxide and (ii) electrolytically generated from electrochemical solution of 0.5 M H_2SO_4 + 5mg/l As_2O_3.

The compatibility of vaporized hydrogen peroxide treatments with high strength 4340 steel was studied in the first phase of the work. Embrittlement of high strength AISI 4340 steel was observed as a result of condensation of the vapor during exposure to the vaporized hydrogen peroxide. Notched four point bending samples of AISI 4340 steel were tested using the standard test methods of ASTM F519-06 to quantify susceptibility to hydrogen embrittlement in this aggressive service environment. No embrittlement effects were observed for samples exposed to strictly vapor phase hydrogen peroxide for concentrations up to 1000 ppm H_2O_2 and exposure times of 4.8 h. Higher concentrations of 1300 and 1600ppm H_2O_2 led to the condensation of the

vapor throughout the process chamber and brittle fracture of samples. These results were confirmed by examination of the fracture surfaces of samples using scanning electron microscopy. Samples that were not considered embrittled possessed dimpled fracture surfaces consistent with ductile failure. Embrittled samples exhibited intergranular fractures along prior austenitic grain boundaries near the root of the notch.

In the second phase of the work, the effects of hydrogen on embrittlement characteristics of low alloy 4340 steel was studied using double-notched tensile samples that were electrochemically charged in-situ with hydrogen in a 0.5 M H_2SO_4 + 5 mg/l As_2O_3 solution. The mechanical response of samples with prior austenitic grain sizes of 10, 40 and 100 μm with martensitic hardness of 41-52 HRC were examined after hydrogen charging times of 0-40 min. As expected, increases in hydrogen charging time and hardness resulted in decreased failure strains and decreased evidence of ductile fracture. Harder samples showed predominant intergranular fracture close to the notch and a combination of ductile and apparent cleavage fracture away from the notch. Softer samples showed quasi-cleavage fracture close to the notch and predominant ductile fracture as the distance from the notch increased. Increasing the strain rate for hydrogen charged samples resulted in decreased failure strains and increased evidence of brittle fracture. Finally, increasing the size of the prior austenitic grains was found to lead to sample failure via brittle transgranular quasi cleavage for the large-grained softer samples while brittle intergranular fracture dominated the large-grained hardest samples.

Acknowledgments

Praises and glory be to the Allah, the Lord of the worlds, my cherisher, sustainer and evolver. Without His mercy I could not have done any good. Following appreciation goes to my parents who have borne a lot of hardship to raise me to this stage. No lesser than my parents, I indebted to my advisor Prof. Ruel A Overfelt, who played a fatherly role during my entire PhD with his constant guidance, instruction, and academic as well as mental support in every aspect of this study. It would have been impossible to complete this work during the years without his continuous effort of supervision and encouragement. I would also like to express my gratitude to my former advisor Professor W. F. Gale for his support and advice at the early stage of my Ph.D. I indebted to Prof. J. W. Fergus for his invaluable advice and instructions during this work. Sincere thanks are also owed to my committee members: Prof. B. C. Prorok and Prof. C. G. Shannon for their help and suggestions on this dissertation. I am thankful to Prof. M. Bozack for agreeing to be the outside reader for this dissertation. I would like to express my gratitude to Mr. M. Crumpler, Mr. R. Howard, Mr. S. Moore and Mr. L.C. Mathison (late) for their technical help in my research. Sincere thanks to my former colleagues: Dr. N Sofyan, Dr. S F Chou, Dr. R. L Haney Dr. C Kang, Mr. R Viswanathan, Mr. J Andress and Ms. A Neer and my current colleagues: Dr. S. Horikawa, Ms. B Brook, Ms. A. Buck and Mr. M. Roberts. I certainly indebted to my wife for her constant mental support, patience and sacrifice during my PhD.

Table of Contents

Abstract.....ii

Acknowledgement.....iv

List of Figures.....ix

List of Tables.....xx

List of Abbreviations.....xxi

1. Introduction.....1

2. Scientific Background.....4

2.1 Vaporized Hydrogen Peroxide (VHP) Sterilization/Decontamination Processes.....4

2.1.1 Condensation during VHP Treatments.....5

2.1.2 Material Compatibility Issues with VHP Treatments.....7

2.2 Hydrogen in Metals.....9

2.3 Degradation of Mechanical Properties.....10

2.4 Fractographic Characterization of Major Fracture Modes.....21

2.5 Hydrogen Embrittlement Mechanisms.....25

2.6 Tempered Martensitic Embrittlement.....30

2.7 Grain Size Effects of Embrittlement Behavior of Martensitic Steel.....33

3. Experimental Procedures 39

3.1 Sample Configuration and Preparation

3.1.1 V-notch 4-point Bend Sample.....39

3.1.2 Double Notch Round Bar Tensile Sample.....41

3.2 Metallography…….....42

3.2.1. Microstructural Evaluation and PAGS Measurements.…….42

3.3 Hydrogen Charging and Mechanical Testing ……...44

3.3.1 Vapor Phase Charging by VHP Exposure and 4-Point Bend Test……44

3.3.2 In-situ Electrochemical Charging and Tensile Test..…….47

3.4 Quantitative Fractographic Measurement……....49

4. Results and Discussions……50

4.1 Microstructural Result…..……50

4.1.1 Microstructure of the V- Notch Bend Sample…….……..50

4.1.2 Microstructure of the Double Notch Tensile Samples……..50

4.2 VHP Exposure Results……54

4.2.1 Mechanical Response……54

4.2.2 Fracture Behavior……...57

4.3 Electrochemical Hydrogenation Results..……59

4.3.1 Effects of Charging Time……...59

4.3.1.1 Mechanical Response……..59

4.3.1.2 Fracture Behavior ……....60

4.3.2 Effects of Strain Rate..……...85

4.3.2.1 Mechanical Response…..……..85

4.3.2.2 Fracture Behavior…….....87

5. Conclusions……104

References.....107

Appendix A: Demonstrations of the Quantitative estimation of the fracture mode…….....113

Appendix B: Tensile Test Result...…….……..119

Appendix C: Various Appearances of the Quasi-Cleavage
And Mixed Mode Quasi Cleavage……..121

List of Figures

Figure 2.1. (a) Schematic of a vaporized hydrogen peroxide sterilization system
(b) Process schematic for vaporized hydrogen peroxide sterilization….. ……. 5

Figure 2.2. Summary of the process and microstructural variable for hydrogen assisted failure. Different ways of hydrogen generation, its transport phenomena in the material and its accumulation and subsequent interaction with the various microstructural features leading to premature fracture is schematically demonstrated…….....9

Figure 2.3. Diffusion of hydrogen from lower binding energy trap sites to the vicinity of the notch for loaded sample with notch (or discontinuity).…….....10

Figure 2.4. Effect of hydrogen charging on reduced ductility of AISI 4340 of three different levels were manifested by reduced % reduction in area……...11

Figure 2.5. The true stress-strain behavior for uncharged and hydrogenated 4340 steel…….12

Figure 2.6. Percent reduction in area with hydrogen concentration for specimen taken from center, side and corner of a chill-cast ingot.……13

Figure 2.7. True fracture strain of uncharged and hydrogenated 1020 steel over a temperature range of -200^{o}C to 100^{o}C at two different strain rates, 5% min^{-1} and 10^{4} % min^{-1} ……....14

Figure 2.8. Variation of four different mechanical properties with hydrogen concentration for Mo steel. Percent elongation and reduction of area deteriorated with increasing hydrogen content but yield strength and UTS did not show any significant change……..14

Figure 2.9. Reduction in failure strength with hydrogen concentration for notched 4340 steel…….16

Figure 2.10.Typical schematic of delayed failure for hydrogenated high strength steel…….……..16

Figure 2.11. Variation of true fracture strain (ln A_o/A) with strain rate ($\dot{\varepsilon}$) over a temperature range of –200^{o}C to 100^{o}C for (a) as-annealed; (b) cathodically hydrogenated for 1h in 4% sulphuric acid solution; and (c) combined for ease of comparison. Surfaces c and d in (b) indicate that the embrittlement effect for hydrogenated sample is most intense close to room temperature…….....18

Figure 2.12. True Fracture strain ln (a_o/a) as function of strain rate for uncharged and hydrogenated SAE 1020 steel……..……..19

Figure 2.13. Fracture strain as function of strain rate in steel……....20

Figure 2.14. Typical intergranular fracture surface features in hydrogenated steel.
(a) intergranular fracture with very little microvoid features,
(b) intergranular fracture associated with significant microvoids..……22

Figure 2.15. Typical cleavage fracture surface features in hydrogenated steel.
(a) strain rates used 2 x10^{-3} s^{-1}
(b) strain rates used 1 x 10^{-6} s^{-1} [51]…….. 23

Figure 2.16. Typical quasi cleavage surface features: (a) predominant quasi [53,54], (b) mixed mode quasi cleavage with associated smooth facets and little random IG fracture 53,54] , (c) quasi-cleavage (QC) [and associated smooth translath boundary facet B) [49] (d) quasi cleavage (at higher magnification showing associated fine lath like features, tear ridges [11]…..……..24

Figure 2.17. (a) Hydrogen occupying dislocation strain filed, enhances dislocation motions and dislocation pile ups against GBs and second phase carbide precipitate at GBs;
(b) Hydrogen induced shielding effect resulting decrease in mutual repulsion between dislocations [61]…….27

Figure 2.18. Presence of hydrogen enhances dislocation movement.
Note the sequential movement of dislocation #4 with respect to the location of dislocation #5. [63].....28

Figure 2.19. Hydrogen enhanced dislocation pile ups [64]……..29

Figure 2.20. Influence of impurity elements on impact strength of hardened, tempered high purity 1.5 Ni-Cr-Mo Alloy [71]……..31

Figure. 2.21.Hall Petch plot of yield strength vs. (prior austenitic grain size)$^{-1/2}$ for 4340 steel [derived from Proctor and Paxton [13]……...35

Figure 2.22. (a) Crack velocity vs grain size , (b) threshold stress intensity vs grain size for 4340steel. derived from Lessar and Gerberich [15]…….....35

Figure 2.23. Typical schematic of lath martensite microstructure.
Prior austenitic grains are subdivided into martensite lath packets which are further subdivided into blocks
and the blocks may further be subdivided into sub-blocks [88]……...36

Figure 2.24. Size of martensitic lath packets vs prior austenitic grain size in Fe- 0.2 wt % C and Fe- 0.2 wt % C – 2 wt% Mn alloy [85]…….37

Figure 2.25. Width of constituting blocks the martensitic lath packets vs prior austenitic grain size in Fe- 0.2 wt % C and Fe- 0.2 wt % C – 2 wt% Mn alloy [85]… ……....37

Figure 2.26. Hall-Petch type plots (a) for yield strength vs. (packet size)$^{-1/2}$ (b) for yield strength vs. (block size)$^{-1/2}$ [85]……..……...38

Figure 3.1. 4 - point bend sample per ASTM F-519 [86]…….....39

Figure 3.2. Typical engineering stress–strain curve of the as-received 4340 steel alloy prior to hydrogen embrittlement testing……...40

Figure 3.3. Double notched round bar tensile sample (measurements are given in inch)……. .42

Figure 3.4. Mechanical test system for application of sustained 4-point bending loads in a vaporized hydrogen peroxide isolation chamber……45

Figure 3.5. Hydrogen charging apparatus was mounted on the tensile instrument (MTS Q-Test). Samples were charged with hydrogen and immediately loaded under tension at cross head speed of 0.01 and 0.03 mm/min and the electrolyte was simultaneously removed……49

Figure 4.1. (a) Martensitic microstructure of the heat treated 4340 steel samples (2% nital etchant, HRC= 52). (b) Prior austenitic grain boundariesof the heat treated steel samples (modified Winsteard's reagent)…….....50

Figure 4.2. SEM images of the modified Winsteard's reagent etched metallographic samples revealing PAGS at six different conditions annotated in the respective pictures……...51

Figure 4.3. Light microscopic images of the modified winstead's reagent etched metallographic samples showing prior austenitic grain sizes (modified Winstead's reagent) achieved at six different heat treatment conditions. Austenitized and tempered at (a) 870^{o}C (1h) and 350^{o}C (2h) , (b) 870^{o}C (1h)and 500^{o}C (2h), (c) 1100^{o}C (1h) and 350^{o}C (2h) , (d) 1100^{o}C(1h) and 500^{o}C, (e) 1250^{o}C (1h) and 350^{o}C (2h) , (f) 1250^{o}C (1h) and 500^{o}C (2h). Prior austenitic grain sizes and hardnesses are shown in the respective pictures..……53

Figure 4.4. Hydrogen embrittlement results for the hydrogen peroxide exposure concentrations, exposure times and mechanical loads shown. Note the indicated appearance of condensation during some treatments……..55

Figure 4.5. Fracture surface of a non-embrittled sample exposed to 500ppm H_2O_2 for 4.8 h exhibiting ductile failure by microvoid coalescence. (a) Fracture surface near (with 150 µm) the notch root. (b) Fracture surface approximately 5mm away from the notch root……58

Figure 4.6. Fracture surface of an embrittled sample exposed to 1600ppm H_2O_2 and condensed liquid (approximately 64 wt.% H_2O_2) for 4.8 h. (a) Fracture surface near the notch root exhibiting extensive intergranular fracture at the prior austenitic grain boundaries. (b) Fracture surface approximately 5mm away from the notch root exhibiting ductile failure by microvoid coalescence……..58

Figure 4.7. Change in failure strain as function of hydrogen charging time for the sample hardnesses and prior austenitic grain sizes (PAGS) shown. Tensile tests were performed using a cross head speed of 0.01 mm/min. The 100 µm PAGS samples were not charged for any times > 10 min. Error bars indicate the 2σ limit of data scatter……...59

Figure 4.8. Fracture characteristics for uncharged 10 and 40 µm PAGS harder samples: (a) and (c) ~ 100 µm from the notch, (b) and (d) ~ 2000 µm away µm from the notch. PAGS and hardnesses are shown in the respective images. Arrows indicate the crack growth direction. Cross-head speed used: 0.01mm/min……61

Figure 4.9. Fracture characteristics for uncharged 10 and 40 µm PAGS softer samples: (a) and (c) ~ 100 µm from the notch, (b) and (d) ~ 2000 µm away µm from the notch. PAGS and hardnesses are shown in the respective images. Arrows indicate the crack growth direction. Cross-head speed used: 0.01mm/min……62

Figure 4.10. Fracture characteristics for 10 min hydrogen charged 10 and 40 µm PAGS harder samples: (a) and (c) ~ 100 µm from the notch, (b) and (d) ~ 2000 µm away µm from the notch. PAGS and hardnesses are shown in the respective images. Arrows indicate the crack growth direction. Cross-head speed used: 0.01mm/min…….....64

Figure 4.11. Fracture characteristics for 10 min hydrogen charged 10 and 40 µm PAGS softer samples: (a) and (c) ~ 100 µm from the notch, (b) and (d) ~ 2000 µm away µm from the notch. PAGS and hardnesses are shown in the respective images. Arrows indicate the crack growth direction. Cross-head speed used: 0.01mm/min……...65

Figure 4.12. Fracture characteristics for 20 min hydrogen charged 10 and 40 µm PAGS softer samples: (a) and (c) ~ 100 µm from the notch, (b) and (d) ~ 2000 µm away µm from the notch. PAGS and hardnesses are shown in the respective images. Arrows indicate the crack growth direction. Cross-head speed used: 0.01mm/min……...66

Figure 4.13. Fracture characteristics with increasing distance from the notch for 20 min hydrogenated 10µm PAGS, 52 HRC samples. Pictures taken from (a) 100µm, (b) 500 µm, (c) 1000µm and (d) 2000µm away from the notch. Arrows indicate the crack growth direction. Cross-head speed used: 0.01mm/min……...69

Figure 4.14. Fracture characteristics with increasing distance from the notch for 20 min hydrogenated 40µm PAGS, 50 HRC samples. Pictures taken from (a) 100µm, (b) 500 µm, (c) 1000µm and (d) 2000µm away from the notch. Arrows indicate the crack growth direction. Cross-head speed used: 0.01mm/min……...70

Figure 4.15. Fracture characteristics with increasing distance from the notch for 40 min hydrogenated 10µm PAGS, 45 HRC samples. Pictures taken from (a) 100µm, (b) 500 µm, (c) 1000µm and (d) 2000µm away from the notch. Arrows indicate the crack growth direction. Cross-head speed used: 0.01mm/min……...71

Figure 4.16. Fracture characteristics with increasing distance from the notch for 40 min hydrogenated 40µm PAGS, 43 HRC samples. Pictures taken from (a) 100µm, (b) 500 µm, (c) 1000µm and (d) 2000µm away from the notch. Arrows indicate the crack growth direction. Cross-head speed used: 0.01mm/min……...72

Figure 4.17. Fracture characteristics for 0 and 10 min hydrogen charged 100 µm PAGS harder (48HRC) samples. Charging times are shown in the respective images : (a) and (c) ~ 100 µm from the notch, (b) and (d) ~ 2000 µm away µm from the notch. Arrows indicate the crack growth direction. Cross-head speed used: 0.01mm/min……...75

Figure 4.18. Fracture characteristics for 0 and 10 min hydrogen charged
100 μm PAGS softer (41HRC) samples. Charging times are shown
in the respective images : (a) and (c) ~ 100 μm from the notch,
(b) and (d) ~ 2000 μm away μm from the notch.
Arrows indicate the crack growth direction.
Cross-head speed used: 0.01mm/min……..76

Figure 4.19. Quantitative variation of percent fracture modes with
increasing distance from the notch for harder samples for
0, 5,10 and 20 min hydrogen charging: PAGS and hardnesses
are shown in the respective pictures (a) and (c) intergranular,
(b) and (d) flat surfaces.Each data point represents average
of 4 samples. Error bars represent 2σ scatter.
Cross-head speed used : 0.01mm/min…….79

Figure 4.20. Quantitative variation of percent fracture modes with
increasing distance from the notch for softer samples for
0, 20, 30 and 40 min hydrogen charging: PAGS and hardnesses
are shown in the respective pictures (a) and (c) intergranular,
(b) and (d) quasi-cleavage. Each data point represents average
of 4 samples. Error bars represent 2σ scatter
Cross-head speed used : 0.01mm/min. ……..……80

Figure 4.21. Quantitative variation of various fracture modes with
increasing distance from the notch for 20 min charged
(a) 10μm PAGS, 52 HRC samples (b) 40μm PAGS, 50 HRC and
40 min charged (c) 10μm PAGS, 45 HRC and (d) 40μm PAGS, 43 HRC.
Each data point represents average of 4 samples.
Error bars represent 2σ scatter.
Cross head speed used 0.01 mm/min.…….81

Figure 4.22.Quantitative variation of percent fracture modes with
increasing distance from the notch for harder and softer 100 PAGS samples
for 0, 5 and 10 min hydrogen charging: Hardnesses are shown
in the respective pictures (a) and (c) intergranular,
(b) and (d) quasi-cleavage. Each data point represents average of 4 samples.
Error bars represent 2σ scatter.
Cross-head speed used : 0.01mm/min ……..83

Figure 4.23.Quantitative Variation of various fracture modes with
increasing distance from the notch for 10 min charged, 100μm PAGS
harder and softer samples. (a) Harder :48 HRC samples
(b) Softer :41 HRC sample.
Each data point represents average of 4 samples.
Error bars represent 2σ scatter.
Cross-head speed used: 0.01 mm/min……...84

Figure 4.24.Change in failure strain as function of two strain rates
2.85 x 10^{-6} s^{-1} (CHS: 0.01 mm/min) & 8.55 x 10^{-6} s^{-1}
(CHS: 0.03 mm/min): (a) 10 and 40 μm harder samples
(50-52 HRC) hydrogen charged for 0 and 5 min,
(b) at 10 and 40 μm softer samples (43-45 HRC)
hydrogen charged for 0,10 and 20 min.
Error bars indicate 2σ scatter……..……...86

Figure 4.25. Fracture characteristics with increasing distance from
the notch for uncharged 10μm PAGS, 52 HRC samples
for two different strain rates 2.85 x 10^{-6} s^{-1} (CHS: 0.01 mm/min) (a- c)
and 8.55 x 10^{-6} s^{-1} (CHS: 0.03 mm/min) (a´- c´).
Strain rates and distances from the notch are shown.
Arrows indicate the crack growth direction…….……..89

Figure 4.26. Fracture characteristics with increasing distance from
the notch for uncharged 40μm PAGS, 50 HRC samples
for two different strain rates 2.85 x 10^{-6} s^{-1} (CHS: 0.01 mm/min)
(a- c) and 8.55 x 10^{-6} s^{-1} (CHS: 0.03 mm/min) (a´- c´).
Strain rates and distances from the notch are shown.
Arrows indicate the crack growth direction.……..90

Figure 4.27. Fracture characteristics with increasing distance from
the notch for 5 min charged 10μm PAGS, 52 HRC samples
for two different strain rates 2.85 x 10^{-6} s^{-1} (CHS: 0.01 mm/min)
(a- c) and 8.55 x 10^{-6} s^{-1} (CHS: 0.03 mm/min) (a´- c´).
Strain rates and distances from the notch are shown.
Arrows indicate the crack growth direction……..91

Figure 4.28. Fracture characteristics with increasing distance from
the notch for 5 min charged 40μm PAGS, 50 HRC samples
for two different strain rates 2.85 x 10^{-6} s^{-1} (CHS: 0.01 mm/min)
(a- c) and 8.55 x 10^{-6} s^{-1} (CHS: 0.03 mm/min) (a´- c´).
Strain rates and distances from the notch are shown.
Arrows indicate the crack growth direction……..92

Figure 4.29. Fracture characteristics with increasing distance from
the notch for uncharged 10μm PAGS, 45HRC samples
for two different strain rates 2.85 x 10^{-6} s^{-1} (CHS: 0.01 mm/min)
(a-c) and 8.55 x 10^{-6} s^{-1} (CHS: 0.03 mm/min) (a´ - c´).
Strain rates and distances from the notch are shown.
Arrows indicate the crack growth direction……..93

Figure 4.30. Fracture characteristics with increasing distance from the notch for uncharged 40μm PAGS, 43HRC samples for two different strain rates 2.85 x 10^{-6} s^{-1} (CHS: 0.01 mm/min) (a-c) and 8.55 x 10^{-6} s^{-1} (CHS: 0.03 mm/min) (a′ - c′). Strain rates and distances from the notch are shown. Arrows indicate the crack growth direction……..94

Figure 4.31. Fracture characteristics with increasing distance from the notch for 20 min charged 10μm PAGS, 45HRC samples for two different strain rates 2.85 x 10^{-6} s^{-1} (CHS: 0.01 mm/min) (a-c) and 8.55 x 10^{-6} s^{-1} (CHS: 0.03 mm/min) (a′ - c′). Strain rates and distances from the notch are shown. Arrows indicate the crack growth direction……..95

Figure 4.32. Fracture characteristics with increasing distance from the notch for 20 min charged 40μm PAGS, 43HRC samples for two different strain rates 2.85 x 10^{-6} s^{-1} (CHS: 0.01 mm/min) (a-c) and 8.55 x 10^{-6} s^{-1} (CHS: 0.03 mm/min) (a′ - c′). Strain rates and distances from the notch are shown. Arrows indicate the crack growth direction……..96

Figure 4.33. Quantitative variation of percent intergranular and flat surface modes with increasing distance from the notch for 10 and 40 μm PAGS harder (50-52 HRC) samples for two different strain rates speeds of 2.85 x 10^{-6} s^{-1} (CHS: 0.01 mm/min) and 8.55 x 10^{-6} s^{-1}(CHS: 0.03 mm/min) after 0 and 5 min hydrogen charging. (a) and (c) intergranular , (b) and (d) flat surfaces. Each data point represents average of 4 samples. Error bars represent 2σ scatter……100

Figure 4.34. Quantitative variation of various fracture modes with increasing distance from the notch 10 and 40 μm harder (50-52 HRC) samples for two different strain rates speeds of 2.85 x 10^{-6} s^{-1} (CHS: 0.01 mm/min) and 8.55 x 10^{-6} s^{-1} (CHS: 0.03 mm/min) after 5 min hydrogen charging. Each data point represents average of 4 samples. Error bars represent 2σ scatter……101

Figure 4.35. Quantitative variation of percent intergranular and flat surface modes with increasing distance from the notch for 10 and 40 μm PAGS softer (43-45 HRC) samples for two different strain rates speeds of 2.85 x 10^{-6} s^{-1} (CHS: 0.01 mm/min) and 8.55 x 10^{-6} s^{-1}(CHS: 0.03 mm/min) after 0 and 20 min hydrogen charging. (a) and (c) intergranular , (b) and (d) quasi-cleavage surfaces. Each data point represents average of 4 samples. Error bars represent 2σ scatter……102

Figure 4.36. Quantitative variation of various fracture modes with increasing distance from the notch 10 and 40 μm softer (43-45 HRC) samples for two different strain rates speeds of 2.85 x 10^{-6} s^{-1} (CHS: 0.01 mm/min) and 8.55 x 10^{-6} s^{-1} (CHS: 0.03 mm/min) after 20 min hydrogen charging. Each data point represents average of 4 samples. Error bars represent 2σ scatter……103

Figure A-1 Demonstration of the quantitative estimation of various fracture features for 20 min hydrogenated 10 μm 52 HRC sample loaded at 0.01 mm/min. The yellow lines represent regions of intergranular fracture; red lines represent regions of microvoid coalescence and the brown lines represents regions of flat surfaces (unsure if they are intergranular or quasi) on the entire image length at a distance ~1000μm from the notch. Sum of each set of colored lines over the entire length (indicated by the black line) determines the fraction of each……113

Figure A-2 Demonstration of the quantitative estimation of various fracture features for 20 min hydrogenated 40 μm 50 HRC sample loaded at 0.01 mm/min. The yellow lines represent regions of intergranular fracture; red lines represent regions of microvoid coalescence and the brown lines represents regions of flat surfaces (unsure if they are intergranular or quasi) on the entire image length at a distance ~1000μm from the notch. Sum of each set of colored lines over the entire length (indicated by the black line) determines the fraction of each……114

Figure A-3. Demonstration of the quantitative estimation of various fracture features for 40 min hydrogenated 10 µm 45 HRC sample loaded at 0.01 mm/min. The yellow lines represent regions of intergranular fracture; red lines represent regions of microvoid coalescence and the green lines represent regions of quasi-cleavage surfaces and its associated smooth facets on the entire image length at a distance ~500 µm from the notch. Sum of each set of colored lines over the entire length (indicated by the black line) determines the fraction of each……..115

Figure A-4. Demonstration of the quantitative estimation of various fracture features for 40 min hydrogenated 40 µm 43 HRC sample loaded at 0.01 mm/min. The yellow lines represent regions of intergranular fracture; red lines represent regions of microvoid coalescence and the green lines represent regions of quasi-cleavage surfaces and its associated smooth facets on the entire image length at a distance ~500 µm from the notch. Sum of each set of colored lines over the entire length (indicated by the black line) determines the fraction of each……....116

Figure A-5. Demonstration of the quantitative estimation of various fracture features for 10 min hydrogenated 100 µm 48 HRC sample loaded at 0.01 mm/min. The yellow lines represent regions of intergranular fracture; red lines represent regions of microvoid coalescence and the green lines represent regions of quasi-cleavage surfaces on the entire image length at a distance ~200 µm from the notch. Sum of each set of colored lines over the entire length (indicated by the black line) determines the fraction of each…….....117

Figure A-6. Demonstration of the quantitative estimation of various fracture features for 10 min hydrogenated 100 µm 41 HRC sample loaded at 0.01 mm/min. The red lines represent regions of microvoid coalescence and the green lines represent regions of quasi-cleavage surfaces on the entire image length at a distance ~200 µm from the notch. Sum of each set of colored lines over the entire length (indicated by the black line) determines the fraction of each……118

Figure B-1. Representative tensile test result. 10-100 µm harder and softer samples hydrogenated for 0-40 min and loaded at a cross head speed of 0.01mm/min……....119

Figure B-2. Representative comparison of the Tensile results at two different strain rates for 10-40 μm harder (charged for 0 and 5 min) and softer (charged for 0, 10 and 20 min) and loaded at a cross head speeds of 0.01mm/min and 0.03 mm/min. 100 μm samples were not subjected to loading at 0.03 mm/min……120

Figure C-1. Typical quasi-cleavage features and smooth surfaces associated to it for 10 μm 45 HRC 40 min hydrogenated sample. The associated smooth surfaces are broken parts along the martensite lath boundaries.CHS : 0.01 mm/min. ……...121

Figure C-2. Typical quasi-cleavage features and smooth surfaces associated to it for 10 μm 45 HRC 40 min hydrogenated sample. The associated smooth surfaces are broken parts along the martensite lath boundaries.CHS : 0.01 mm/min……..122

Figure C-3. Typical quasi-cleavage features and smooth surfaces associated to it for 10 μm 45 HRC 20 min hydrogenated sample. The associated smooth surfaces are broken parts along the martensite lath boundaries.CHS : 0.01 mm/min …….....123

Figure C-4. Typical quasi-cleavage features and smooth surfaces associated to it for 10 μm 45 HRC 20 min hydrogenated sample. The associated smooth surfaces are broken parts along the martensite lath boundaries. CHS : 0.01 mm/min……...….124

Figure C-5. Typical quasi-cleavage features for 40 μm 43 HRC 40 min hydrogenated sample. CHS : 0.01 mm/min ……..…….....125

Figure C-6. Typical quasi-cleavage features for 40 μm 43 HRC 40 min hydrogenated sample. CHS : 0.01 mm/min ……126

Figure C-7. Typical quasi-cleavage features and smooth surfaces associated to it for 40 μm 43 HRC 40 min hydrogenated sample. CHS : 0.01 mm/min…….…….127

List of Tables

Table I. Composition of the 4-point bend test specimens of AISI 4340 (provided by vendor)……40

Table II. Composition of the double notch tensile specimens of AISI 4340 (provided by vendor)……41

Table III. Post heat treatment PAGS and Martensitic Hardnesses……....41

Table IV. Average size of the martensitic packets and their constituent blocks as function of grain size……...53

List of Abbreviations

ACER	Airliner Cabin Environment Research
AISI	American Iron and Steel Institute
ASTM	American Society for Testing and Materials
BI	Biological Indicator
CHS	Cross Head Speed
FAA	Federal Aviation Administration
FDA	Food and Drug Administration
HE	Hydrogen Embrittlement
HELP	Hydrogen-Enhanced Local Plasticity
HEPA	High Efficacy Particulate Air
HRC	Rockwell Hardeness
LM	Light Microscopy (also termed as OM : Optical Microscopy)
NFS	Notch Fracture Strength
PAGS	Prior Austenitic Grain Size
PAGB	Prior Austenitic Grain Boundary
RITE	Research in the Intermodal Transport Environment
UTS	Ultimate Tensile Strength
SAE	Society of Automotive Engineers
S/TEM	Scanning / Transmission Electron Microscopy
VHP	Vaporized Hydrogen Peroxide

1. Introduction

Hydrogen based fuel has been identified as a promising alternative to fossil fuel to reduce the emission of greenhouse gases and to enable sustainable energy supplies worldwide [1, 2]. In spite of such promising applications of hydrogen as a prime energy source, serious technical challenges exist due to metallurgical interactions of hydrogen with fracture sensitive metals and alloys [2]. Hydrogen has caused major failures [2] in the oil and gas industries. The uptake of hydrogen into steel tanks, pressure vessels and pipelines has induced unexpected and premature fracture of such structures.

Atomic hydrogen can be generated at the surface of metals and alloys by thermal dissociation of gaseous diatomic hydrogen [3] or by electrochemical decomposition of hydrogen bearing aqueous solutions [4] and vapor condensates [5]. The atomic hydrogen generated is first adsorbed onto the surface and then either interstitially diffuses or is transported by dislocations into the interior of the metals [6]. Once inside hydrogen-sensitive materials, e.g., high strength steel, hydrogen atoms can interact with various microstructural features resulting in enhanced tendency for brittle fracture.

Hydrogen is believed to primarily diffuse along the prior austenitic grain boundaries from the steel surface resulting in weakening those grain boundaries and inducing their decohesion [7]. Hydrogen is also attracted to the triaxial stresses at material discontinuities (e.g., notches, microcracks) reducing the strain energy for crack initiation and propagation [7]. Additionally, hydrogen can be trapped within the stress fields surrounding dislocations leading to either reduction in dislocation mobility [8] or enhancements to dislocation mobility [9]. Reductions in

plastic flow would reduce the fracture while hydrogen-enhanced local plasticity (HELP) could induce grain boundary failures from amplified dislocation pile-ups. Hydrogen induced brittle fracture is microscopically manifested as (i) intergranular fracture along the prior austenitic grain boundaries and/or martensitic lath boundaries or (ii) transgranular fracture along the cleavage planes as well as mixtures of these two fracture modes. Another interesting fractographic feature often associated with hydrogen embrittlement is termed quasi-cleavage and displays characteristics often associated with brittle fracture and plasticity. Recent results [10, 11] discuss some mechanistic aspects associated with quasi-cleavage but the precise details and applicable models remain the subject of controversy [12]. Unfortunately, quantitative explanation of the details of these fracture processes has been difficult over the years due to oftentimes subtle differences.

Although hydrogen levels as low as 1 – 2 wt. ppm are known to induce embrittlement in high strength steel, few investigations have been published which provide specific and quantitative relationships of hydrogen concentration with strain rate, sample mechanical behavior and fracture mode. Shim and Byrne [4] present one such investigation and these researchers report a quantitative relationship of hydrogen concentration with the fracture strength of high strength 4340 steel. However, the prime focus of the paper was to describe the effect of various recombination poisons and current density in the electrochemical hydrogen charging process.

The effects of prior austenitic grain size, alloying elements and impurities on the hydrogen sensitivity of fracture of 4340 high strength steel has been studied by a number of investigators [e.g., 7, 13-16]. Most of the previous research has focused on the function of austenite grain size on (i) crack velocity, (ii) threshold stress intensity or (iii) time to failure. The results of these prior investigations are sometimes in apparent contradiction.

Strain rate is another important parameter that continues to confound researchers studying hydrogen embrittlement of 4340 steel. Effects of strain rate on the hydrogen induced mechanical property degradation are found in the literature over a strain rate range as low as 10^{-4} per sec to as high as 10^{2} per sec [17-20]. According to the available literature, in presence of hydrogen, fracture strain was established to be lower at slower strain rates compared to that for the faster strain rates over a range of strain rate of 10^{3} to 10^{-5} per sec. However, the study on the effect of strain rate below 10^{-5} per sec on the failure strain is hardly found in the literature. Below this limit the effect of strain rate on ductility (failure strain) may show a completely different behavior because of the time available for the hydrogen to diffuse out of the sample before the mechanical driving force needed to propagate the crack reaches the required limit.

This work has been divided into two phases. In the first phase of the work, compatibility of vaporized hydrogen peroxide sterilant/decontaminant of low alloy, high strength 4340 steel was studied using V-notched 4-point bend sample after exposure to various VHP concentrations. Embrittlement of high strength AISI 4340 steel was observed as a result of condensation of the vapor during exposure to vaporized hydrogen peroxide. In the second phase of the work the effects of hydrogen on embrittlement characteristics of low alloy 4340 steel was studied using double-notched tensile samples that were electrochemically charged in-situ with hydrogen in a 0.5 M H_2SO_4 + 5 mg/l As_2O_3 solution. The mechanical response and fracture behavior of samples with prior austenitic grain sizes of 10-100 μm, with martensitic hardness of 41-52 HRC were examined after hydrogen charging times of 0-40 min and loaded at two different strain rates of 2.85×10^{-6} & 8.55×10^{-6} s^{-1}. Data quantifying the observed fracture modes were observed using scanning electron microscopy (i.e., intergranular, quasi-cleavage, flat cleavage-like or dimpled).

2. Scientific Background

2.1 Vaporized Hydrogen Peroxide (VHP) Sterilization/Decontamination Processes

Hydrogen peroxide vapor has been proposed as a sterilant/decontaminant for usage in buildings and transportation vehicles including emergency vehicles, buses, trains and aircraft. Vaporized hydrogen peroxide technology has been utilized for 20 years to sterilize medical and pharmaceutical instruments, devices and clean rooms [21,22]. Vaporized hydrogen peroxide biodecontamination treatments provide rapid sterilization, intrinsic environmental friendliness (*i.e.*, simple by-products composed of only water and oxygen), ease of usage and general compatibility with many materials and systems.

A schematic of a typical, closed-loop hydrogen peroxide vapor generation system and process isolation chamber is shown in Figure 2.1 (a). Most hydrogen peroxide vapor generators use 35% (by weight) H_2O_2 in water solution and flash vaporize the solution on a heated plate. Flash vaporization ensures that the concentration of H_2O_2 in the generated vapor is the same as that in the original solution. As shown in Figure 2.1(b), typical sterilization/decontamination cycles consist of an initial phase where the temperature of the process chamber is stabilized and the relative humidity decreased to a predetermined level. During this dehumidification phase, warm, dry HEPA-filtered air flows into the enclosure to lower the relative humidity which allows a higher concentration of hydrogen peroxide vapor to be injected into the enclosure without condensation. The next phase is to flash vaporize the hydrogen peroxide and water solution to rapidly increase the amount of hydrogen peroxide vapor to the desired concentration as well as minimize the total cycle time. During the sanitization/decontamination phase, a steady

concentration of hydrogen peroxide vapor (typically 250 ppm for 90 min) is maintained to give the desired sanitization/decontamination cycle as often measured by the 6-log kill (*i.e.*, 10^6 reduction) of a commercial biological indicator (BI) spore population of *Geobacillus stearothermophilus*. Once the sanitization/decontamination phase is completed, the enclosure is then aerated with fresh air while any residual hydrogen peroxide vapor breaks down into environmentally benign water and oxygen.

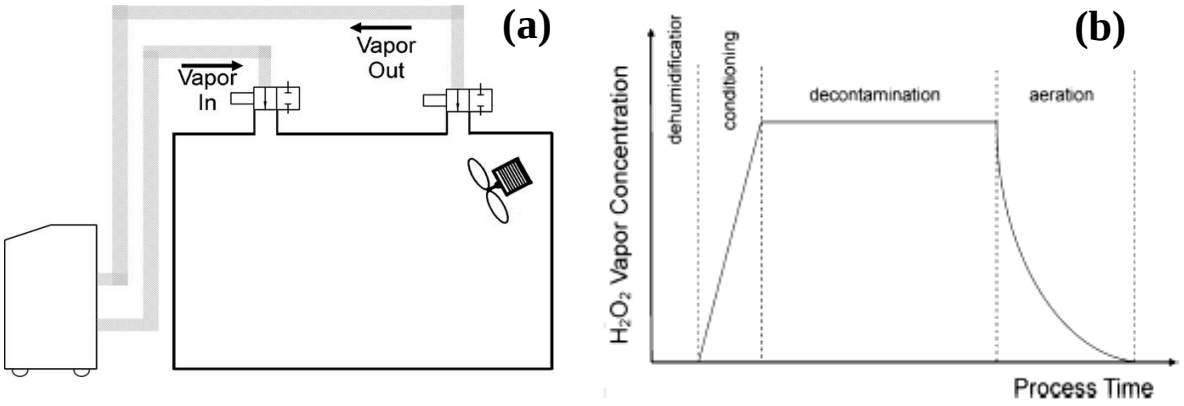

Fig.2.1 (a) Schematic of a vaporized hydrogen peroxide sterilization system
(b) Process schematic for vaporized hydrogen peroxide sterilization

2.1.1 Condensation during VHP Treatments

Unger-Bimczok *et al.* [23] noted that the literature contains considerable disagreement on the optimum process conditions for vaporized hydrogen peroxide treatments. The levels of hydrogen peroxide and relative humidity in the process chamber are particularly important for antimicrobial efficacy. Unger-Bimczok *et al.* [23] found that the higher the levels of H_2O_2 vapor, the less important was the actual level of relative humidity. Conversely, high microbe inactivation rates were found at low levels of H_2O_2 vapor when the levels of relative humidity were high. In fact, sub-visible levels of micro-condensation were found to be necessary for high

microbial inactivation rates. Unger-Bimczok *et al* [23] note that sub-visible levels of micro-condensation are associated with the formation of a thin film of condensate on surfaces prior to the actual appearance of visible droplets. Micro-condensation can be detected with optical dew point sensors. Higher levels (i.e., visible levels) of condensation apparently did not increase the antimicrobial efficacy.

Watling *et al* [24] investigated the thermodynamics and mass transport conditions for the binary H_2O_2-H_2O liquid/vapor system. These researchers show that the maximum concentration of H_2O_2 vapor in the process isolation chamber can be increased when the initial humidity in the chamber is reduced. The upper limit on H_2O_2 vapor concentration is reached when liquid begins to condense from the vapor solution. This limit is the primary reason for the initial dehumidification step as shown in Figure 1(b). Condensation is considered to be problematical and can result in non-uniform decontamination as well as prolonged aeration times when porous materials are involved. A hydrogen peroxide vapor treatment process that is designed to avoid condensation is often referred to as a "dry" process.

Watling *et al* [24] note that the concentrations of the initial bead of condensed liquid can be as high as 50-75 wt. % H_2O_2 even though the original flash vaporized liquid was only 35 wt. % H_2O_2. Such high concentrations of the condensate can naturally lead to the very high microbial inactivation rates seen by Unger-Bimczok *et al.* [23]. Commercial systems have been developed that control the temperature, humidity and hydrogen peroxide vapor concentrations so that the decontamination process provides so-called "micro-condensation" on the surfaces being cleaned [25] . A hydrogen peroxide vapor treatment process that is designed to provide minute levels of condensation is often referred to as a "wet" process.

2.1.2. Material Compatibility Issues with VHP Treatments

Vaporized hydrogen peroxide treatments have been investigated for possible usage in disinfection/decontamination of buildings [26], spacecraft [27], aircraft [28, 29] and railcars [30]. The aircraft studies used vaporized hydrogen peroxide concentrations in the range of 150 - 600 ppm and cycle times of 80 - 120 min. Maximum concentrations of hydrogen peroxide vapor were carefully controlled to avoid condensation in cool locations within the large aircraft cabins.

Previous studies of the compatibility of vaporized hydrogen peroxide exposures as well as 35% liquid hydrogen peroxide exposures to a range of aerospace grade metals (2024-T351, 2024-T6, 7075-T6 and 304 stainless steel) indicated that the 0.2% offset yield strength, ultimate tensile strength and % elongation to failure were unaffected by the exposures [31,32]. Compatibility tests on aerospace grade composite materials (carbon fiber/epoxy, glass fiber/carbon fiber epoxy and FR4 printed circuit board materials) exhibited no significant changes in flexural strength or flexural strain at peak load after ten sequential 4.8 hr exposures to 450 ppm vaporized hydrogen peroxide. However, some mechanical degradation in the composite samples was observed after a 168 hour exposure to 35 wt. % liquid hydrogen peroxide. Delamination of the 1B31 acrylic confocal coating was observed on FR4 printed circuit board materials when exposed to 35 wt. % liquid hydrogen peroxide. Finally, crazing of acrylics was also detected when the vapor process conditions enable condensation to form [31].

Compatibility test results with textiles have been more complex due to the ease of absorption of both hydrogen peroxide and water molecules in typical textiles. Absorbed water is known to decrease the strengths and increase the elongations of many textiles. The tensile strength of nylon was minimally degraded (<10% loss), polyester was slightly degraded (~10% loss), and wool was moderately degraded (~20-30% loss) by exposure to 450 ppm vaporized

hydrogen peroxide. The tensile strength and the elongation to failure of leather were severely degraded (~50% loss) by exposure to 450 ppm vaporized hydrogen peroxide. The tensile strength and the elongation to failure of Nomex were unchanged by exposure to 450 ppm vaporized hydrogen peroxide [33, 34]

The compatibility of vaporized hydrogen peroxide treatment with construction materials of buildings has been recently evaluated [35] and minimal deleterious effects were found. Finally, as a part of the present investigation and reported below, the resistance of high strength 4340 steel to hydrogen embrittlement from exposure to a range of conventional vaporized hydrogen peroxide treatments was evaluated.

2.2 Hydrogen in Metals

Atomic hydrogen can be generated at the surface of metals and alloys by thermal dissociation or electrochemical decomposition of hydrogen bearing compounds. The atomic hydrogen generated is first adsorbed onto the surface and, as shown in Figure 2.2 below, either interstitially diffuses or is transported by dislocations into the interior of the metals. Once inside hydrogen-sensitive materials hydrogen atoms can interact with various microstructural features resulting in enhanced tendency for brittle fracture.

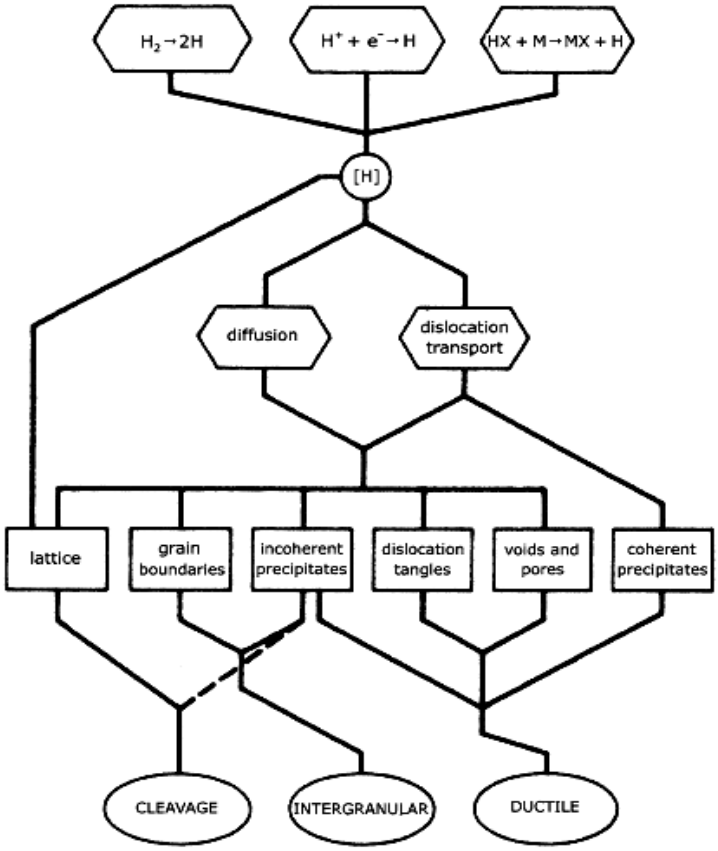

Fig. 2.2 Summary of the process and microstructural variable for hydrogen assisted failure. Different ways of hydrogen generation, its transport phenomena in the material and its accumulation and subsequent interaction with the various microstructural features leading to premature fracture is schematically demonstrated [36].

Figure 2.3 shows the various microstructural traps sites for hydrogen in a metal like 4340 steel [37]. For a notched sample under loading, hydrogen from the lower binding energy trap sites (e.g., interstitial sites) would tend to diffuse to the zone of maximum stress in the vicinity of the notch. This phenomenon is known as stress induced hydrogen diffusion and is explained in detail in Ref. 38. Due to this phenomenon, the embrittling effects of hydrogen have been observed to be most prominent closer to notches in samples. However, extensive quantitative investigations of the effects of hydrogen as function of depth from crack-generating notches are not available in the literature.

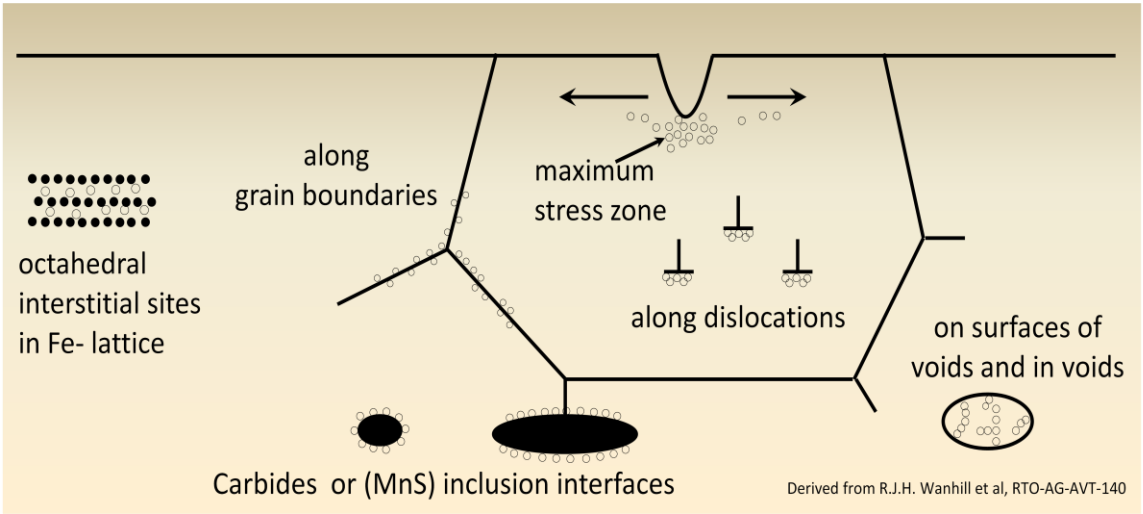

Fig. 2.3 Diffusion of hydrogen from lower binding energy trap sites to the vicinity of the notch for loaded sample with notch (or discontinuity) [37].

2.3. Degradation of Mechanical Properties

Figure 2.4 [39] demonstrates the effect of hydrogen charging on the ductility (reduction in area) of AISI 4340 steel heat treated to different tensile strengths. The sample with the highest strength level (190 kg/mm^2 ≈ 270 ksi ≈ 1860 MPa) was severely embrittled after only two min of hydrogen charging. Additional charging had little effect on further loss of ductility for samples

of these high strength materials. On the other hand, the lowest strength specimen (140 kg/mm^2 ≈ 200 ksi ≈ 1370 MPa) did not show any loss of ductility for the first two min of hydrogen charging and the degree of embrittlement observed after 8 min of hydrogen charging was much smaller compared to specimens with the highest strengths. This indicates a strong hydrogen embrittlement susceptibility for high strength 4340.

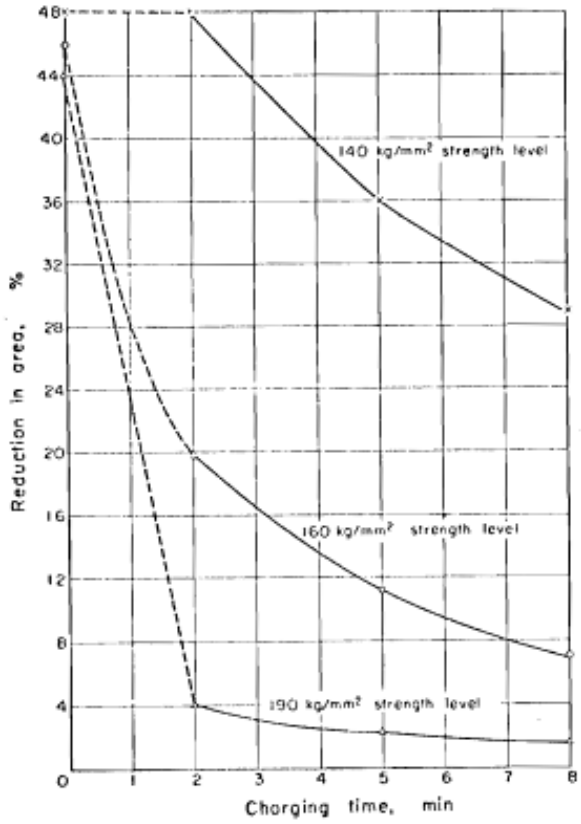

Fig. 2.4 Effect of hydrogen charging on reduced ductility of AISI 4340 of three different levels were manifested by reduced % reduction in area [39]

Figure 2.5 shows Frohmberg et al.'s [39] comparison of the true stress – true strain behavior for an uncharged 4340 sample and a sample hydrogenated for 5 min. The only apparent effect of hydrogenation observed was a dramatic reduction in failure strain.

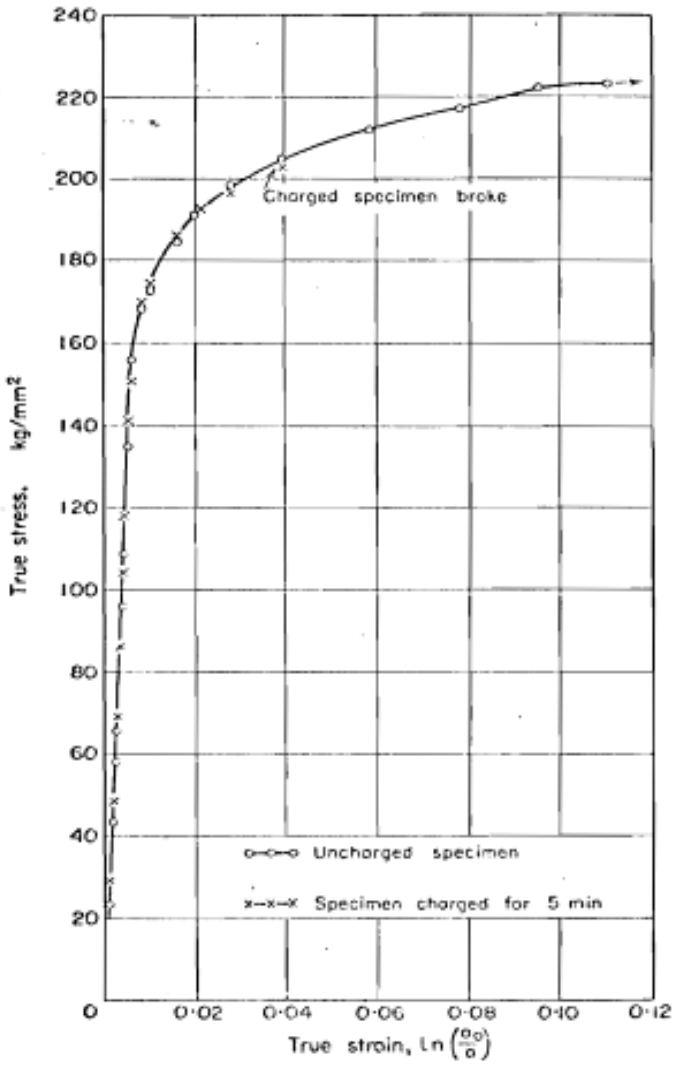

Fig. 2.5 The true stress-strain behavior for uncharged and hydrogenated 4340 steel [39]

Sims et al. [40] also reported on the reduction in ductility due to hydrogen absorption in 4340 steel. The reduced ductility appeared to reach a limit at a hydrogen concentration of 5 cc per 100 g (approximately 9 wt. ppm H) of the sample. High levels of hydrogen content did not induce additional reductions in ductility.

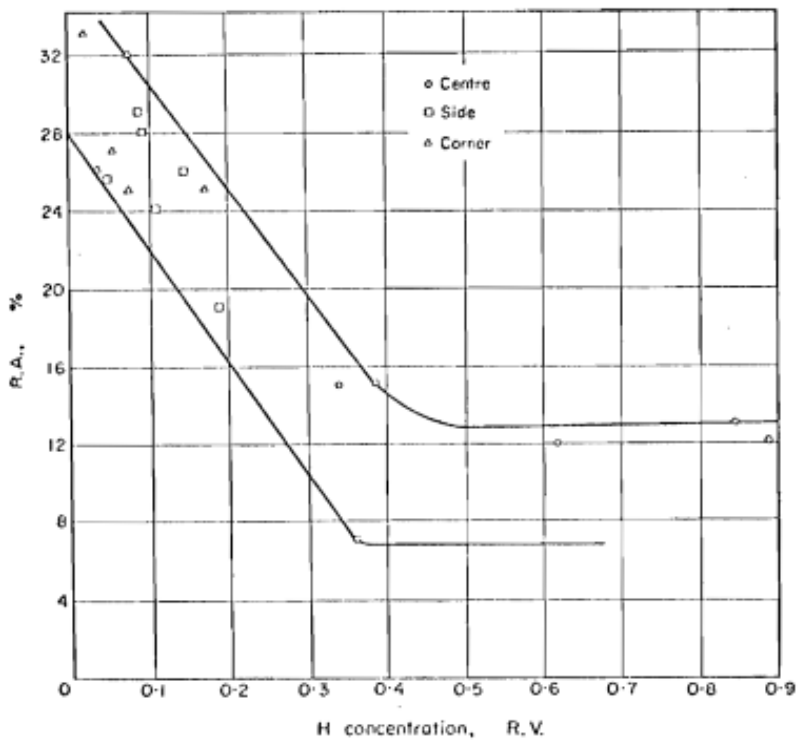

Fig. 2.6 Percent reduction in area with hydrogen concentration for specimen taken from center, side and corner of a chill-cast ingot [40]

Fig. 2.7 demonstrates true fracture strains for uncharged and hydrogenated 1020 steel over a temperature range of -200^{o}C to 100^{o}C for two different strain rates [19]. These data clearly demonstrate that reductions of tensile fracture strain in presence of hydrogen within a temperature range where the atomic movement is not suppressed by very low test temperatures.

Fig. 2.8 demonstrates the trends of various mechanical properties as functions of hydrogen concentration for Mo steel (C ~ 0.5 wt. %) [41]. Mechanical responses in terms of yield strength (σ_y), ultimate tensile strength (UTS), percent elongation and reduction of area were evaluated. Significant decreases in both percent elongation and reduction in area were observed while yield strength and tensile strength exhibited slight increases.

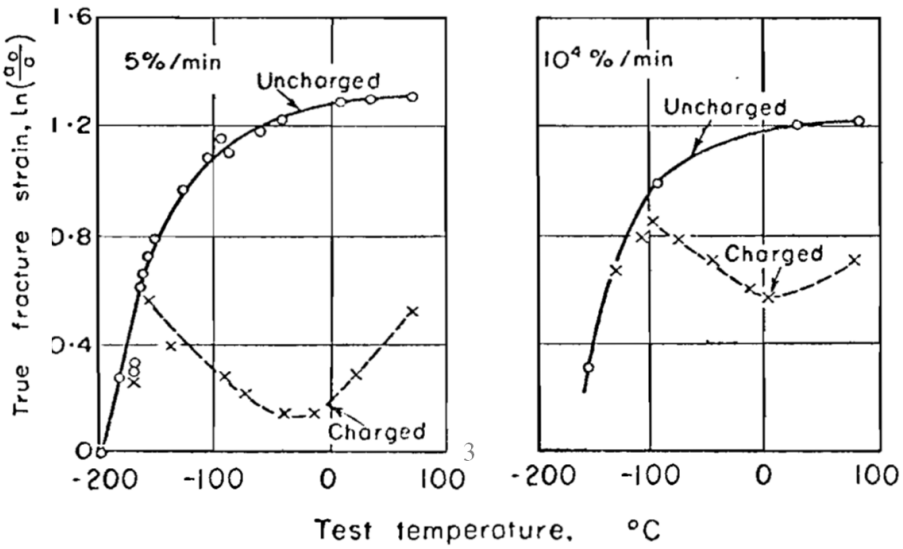

Fig. 2.7 True fracture strain of uncharged and hydrogenated 1020 steel over a temperature range of -200°C to 100°C at two different strain rates, 5% min^{-1} and 10^4 % min^{-1} [19] .

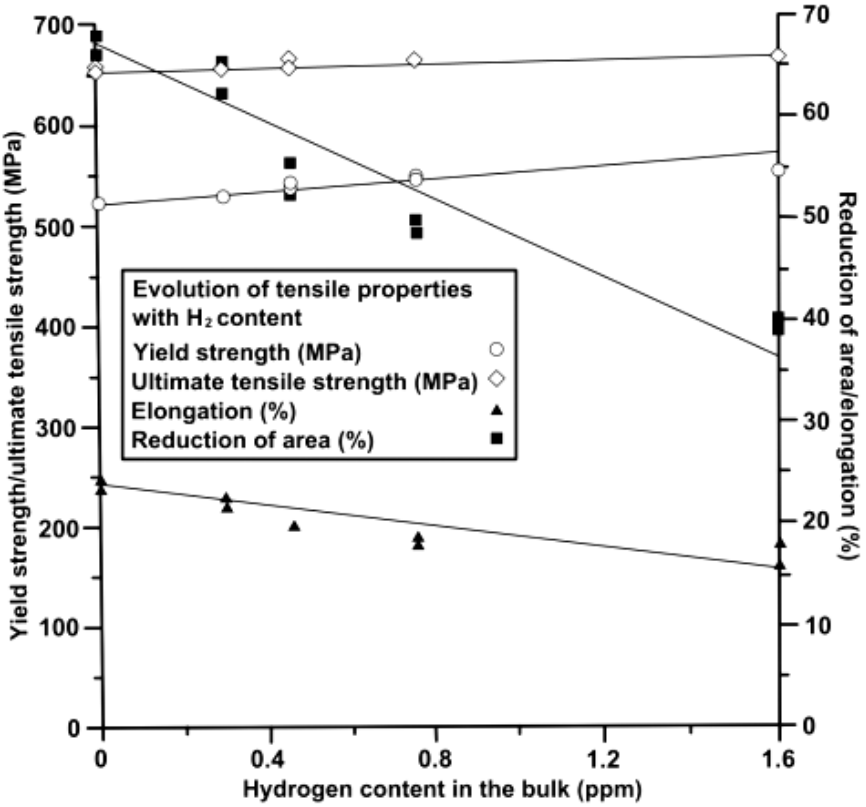

Fig. 2.8 Variation of four different mechanical properties with hydrogen concentration for Mo steel. Percent elongation and reduction of area deteriorated with increasing hydrogen content but yield strength and UTS did not show any significant change [41]

Researchers have reported differing effects of hydrogen on the yield strength of steels. Evidence of yield strength enhancement [e.g., 42 and 42], as well as yield strength reductions [e.g., 43] plus no effects [44] due to the presence of absorbed hydrogen have been reported. These differences in yield strength results may be attributed to differences in temperature range, strain rate and hydrogen concentration used as well as the absolute magnitude of the reported changes being typically quite small. Changes in these parameters modify the intermittent pinning of dislocations and, under certain experimental conditions, even though hydrogen might cause a local (microscopic) softening, that might not be observed macroscopically unless the softening effect is greater than the effect of shear localization [45].

Unnotched samples generally do not exhibit hydrogen-induced reductions in tensile strength [41] although reductions in tensile strength from hydrogen effects are observed for notched samples [4, 46]. The raised tensile stresses in the vicinity of the notch result in higher concentrations of hydrogen in those areas from stress-induced hydrogen diffusion to those areas. Figure 2.9 demonstrates [4] the reduction in notched tensile strength as function of hydrogen concentration for electrochemically hydrogenated notched 4340 steel (tempered at 200^{o}C) loaded at a cross head speed of 0.5 mm/min. Hydrogen was cathodically charged into the samples from 1N sulphuric acid solution poisoned with 5 mg arsenic oxide per liter solution. Obviously, the extent of tensile strength reductions of notched sample would be determined by the combined effects of parameters such as dimensions of the notch, the resultant stress concentration profile, strength level of the steel, hydrogen concentration, strain rate, etc.

Mechanical property degradation of fracture sensitive materials in presence of hydrogen is also manifested in delayed failures under constant load. Hydrogenated samples can show delayed failure under certain static loading conditions (stresses lower than the actual failure

strength but above a so-called lower critical stress level) as shown schematically in Figure 2.10. The lower critical stress is the stress level below which no failure will occur for an extended time.

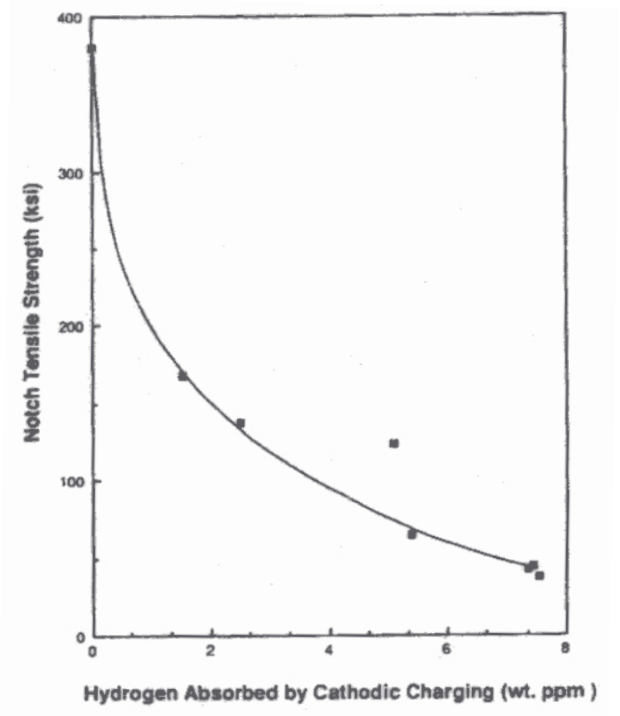

Fig. 2.9 Reduction in failure strength with hydrogen concentration for notched 4340 steel [4].

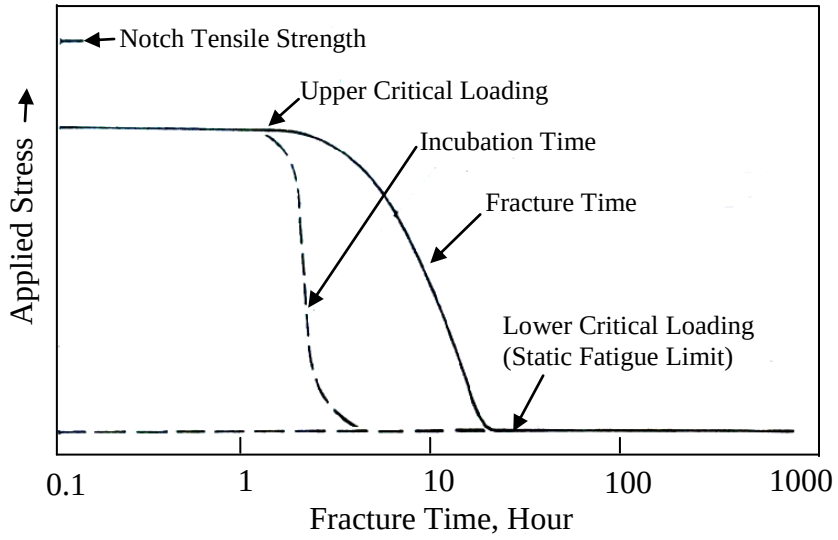

Fig. 2.10 Typical schematic of delayed failure for hydrogenated high strength steel [38].

Hydrogen-induced mechanical property degradation can also cause reductions of fracture toughness [41,43, 46], decreases in threshold stress intensity factor [46-48] and enhanced crack growth rates [46,48].

Effects of strain rate on the hydrogen induced mechanical property degradation are found in the literature over a strain rate range as low as 10^{-5} per sec to as high as 10^{3} per sec. Toh and Baldwin [17] studied the mechanical responses of uncharged and hydrogenated steel over a strain rate over a range of 1 to 10^{5} % per min (1.67×10^{-4} to 1.67×10^{1} per sec). They observed a decrease in the true failure strain with decreasing strain rate while yield strength remained unaffected. See Figure 2.11. Similar result was also reported by Robertson et al. [18] over a strain rate range of 0.01 to 100 per min (1.67×10^{-4} to 1.67×10^{0} per sec) for temperature range of -200 to 200 F.

Brown and Baldwin [19] studied the effect of strain rate on true fracture strain of spherodized SAE 1020 steel over a strain rate range of 1 to 10^{6} % per min (1.67×10^{-4} to 1.67×10^{2} per sec) . Their results shown in Figure 2.12 indicate the fracture strain for the hydrogenated sample was lower for the lower strain rates and increased significantly at the higher strain rates. This is presumably due to the enough time hydrogen gets to interact with microstructural feature in order to cause embrittlement and also at that strain rates the effect of hydrogen is not subjugated by fast atomic movement due to mechanical driving force. Conversely, the uncharged samples showed a very gradual decrease in failure strain with increasing strain rate presumably due to the restricted atomic movement possible at the faster strain rates.

According to the available literature, hydrogen-induced fracture strain is expected to be lower at slower strain rates over a range of strain rate from10^{3} to 10^{-5} per sec. Figure 2.13

summaries fractures strain data as a function of strain rate for steel samples from a number investigations over a range of strain rate of 10^{3} to 10^{-5} per sec [19]. These results indicate that the embrittling effect of hydrogen is strongest within an intermediate strain rate range of 10^{-1} to 10^{-4} per sec and thus the fracture strains over this range are observed to be a minimum.

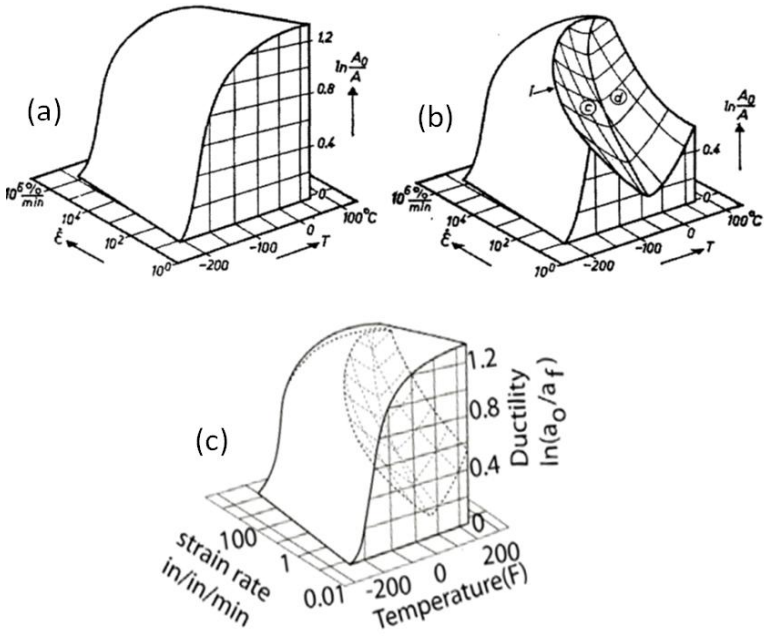

Fig. 2.11 Variation of true fracture strain ($\ln A_o/A$) with strain rate ($\dot{\varepsilon}$) over a temperature range of -200^{o}C to 100^{o}C for (a) as-annealed; (b) cathodically hydrogenated for 1h in 4% sulphuric acid solution; and (c) combined for ease of comparison. Surfaces c and d in (b) indicate that the embrittlement effect for hydrogenated sample is most intense close to room temperature. Adapted from [17] and [18].

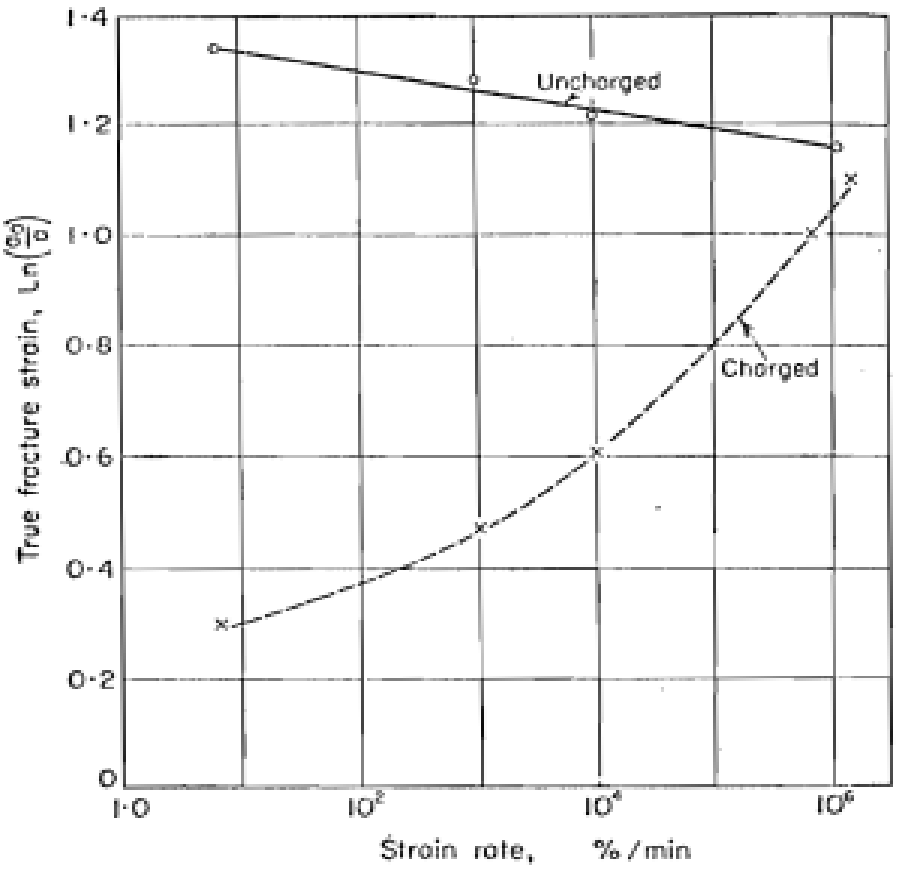

Fig. 2.12 True Fracture strain ln (a_o/a) as function of strain rate for uncharged and hydrogenated SAE 1020 steel [19].

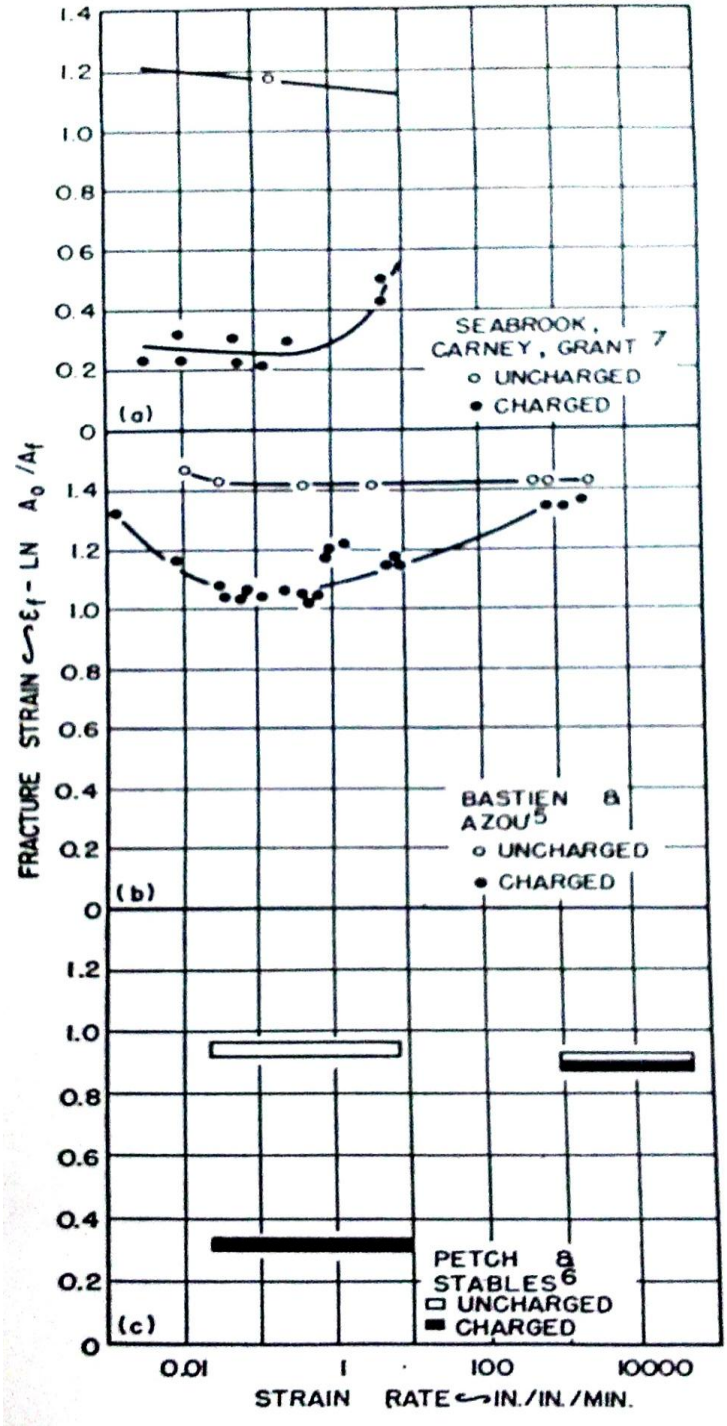

Fig. 2.13 Fracture strain as function of strain rate in steel [19].

2.4. Fractographic Characterization of Major Fracture Modes

Perhaps the greatest area of controversy that has been emerged from hydrogen embrittlement (HE) study is related to the modes of hydrogen induced cracking on the microstructural level. Hydrogen induced brittle fracture characteristics are microscopically manifested as intergranular fracture, cleavage fracture and quasi-cleavage fracture (also known as brittle transcrystalline [49]). These primary fracture modes are often associated to microvoid coalescence. The evidences of secondary cracks are also found with these primary fracture features.

Irrespective of the various mechanisms proposed (see section 2.5) on a microscopic and/or atomic level, intergranular fracture eventually occurs as a result of grain boundary weakening induced by hydrogen. Fig.2.14. (a) and (b) show the typical intergranular fracture mode which is most commonly observed in hydrogen embrittled microstructures. 2.14 (a) shows intergranular fracture with very little evidence of microvoid coalescence associated with it while 2.14 (b) shows intergranular fracture significantly associated to dimples.

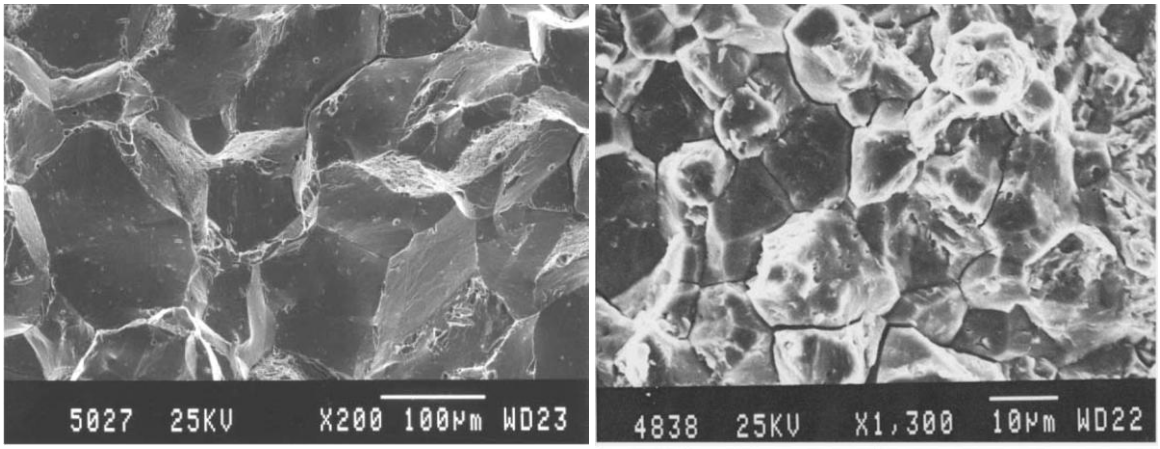

Fig. 2.14. Typical intergranular fracture surface features in hydrogenated steel. (a) intergranular fracture with very little microvoid features, (b) intergranular fracture associated with significant microvoids [50]

Fig. 2.15 (a) and (b) shows the typical cleavage mode fracture features in Fe_3Al-based intermetallics in presence of hydrogen at two different strain rates of 2×10^{-3} s^{-1} and 1×10^{-6} s^{-1} [51]. At both strain rates similar fracture features were observed. Qiao and Mao [51] asserted the fracture features to be predominant cleavage with partial intergranular fracture. Typical river pattern is evident is the cleavage fracture features. This river pattern is due to dislocation threading across the cleavage planes. Random evidence of ductile dimples is also found.

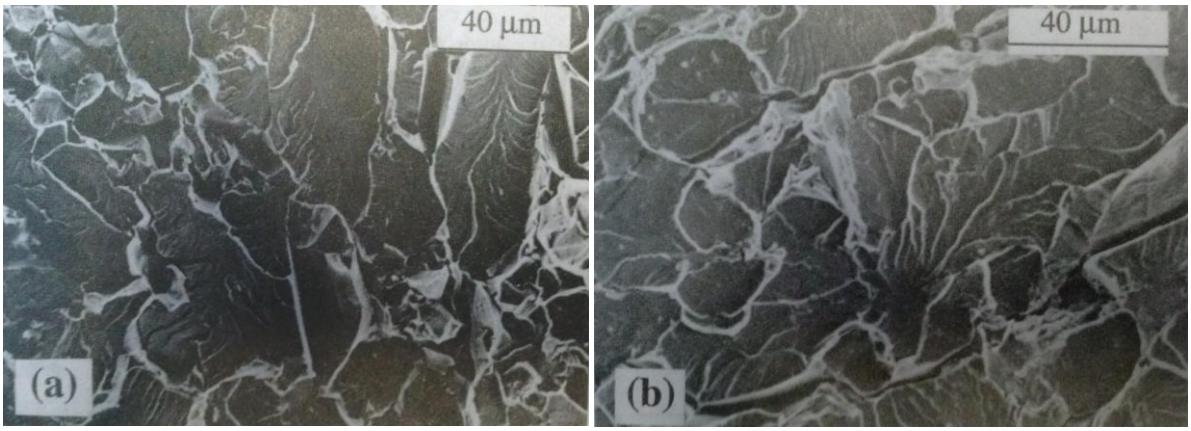

Fig. 2.15. Typical cleavage fracture surface features in hydrogenated steel. (a) strain rates used 2×10^{-3} s^{-1} (b) strain rates used 1×10^{-6} s^{-1} [51]

Quasi-cleavage is the name originated when the fracture features look neither like classical cleavage or typical microvoid coalescence. Martin et al. [10] asserted that quasi-cleavage can result from the growth and coalescence of microvoids that initiate and grow within intense slip band intersections. Lynch [49] also called quasi cleavage as brittle transcrystalline cleavage and argued that quasi-cleavage occurs across martensitic laths and/or along the martensitic lath boundaries. The lath plane associated with the quasi cleavage in martensitic steel is typically {110} plane [52]. According to Lynch [49], these brittle transcrystalline fractures are accompanied with two types of associated features – (i) decorated with tear ridges and striation when occurring across the martensitic lath and (ii) smooth featureless facets are the result of fracture paths along martensitic lath boundaries. Figure 2.16 shows typical appearances of quasi-cleavage.

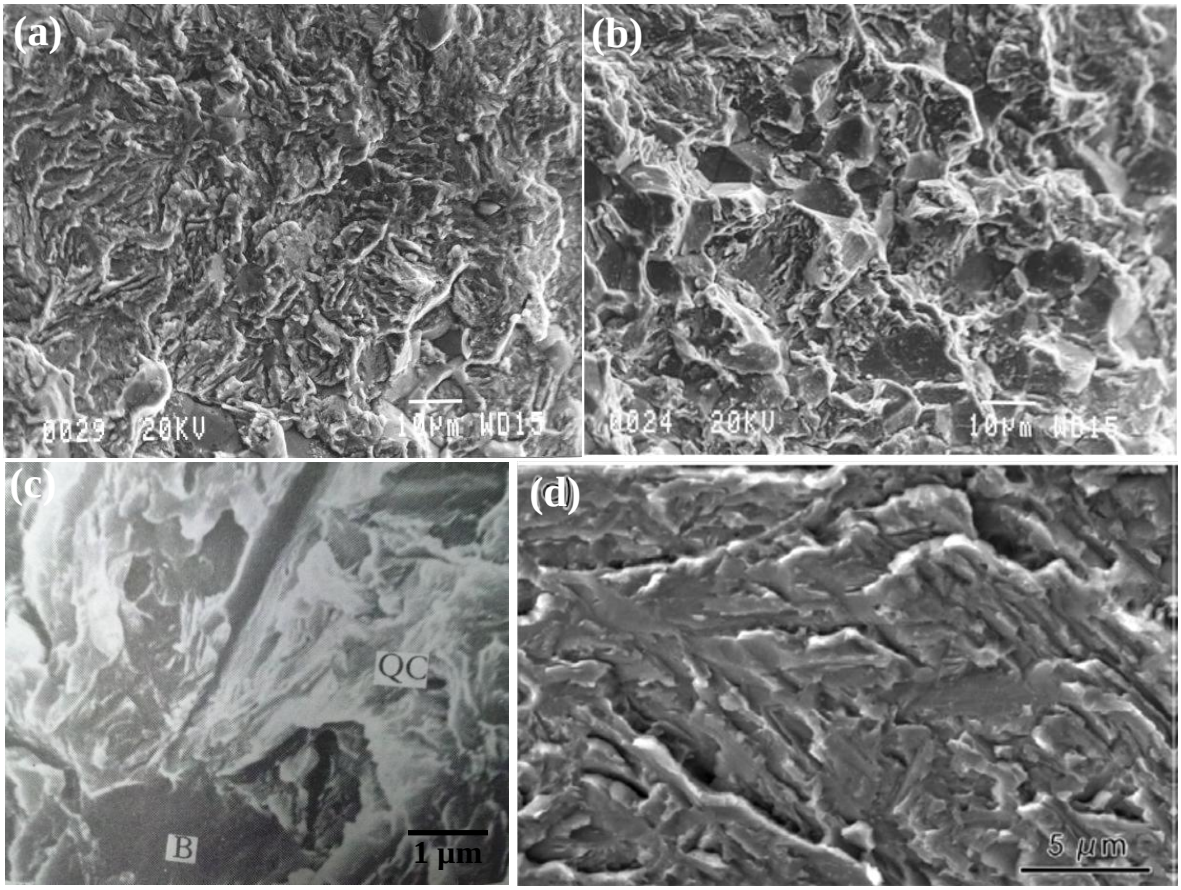

Fig. 2.16. Typical quasi cleavage surface features: (a) predominant quasi [53,54], (b) mixed mode quasi cleavage with associated smooth facets and little random IG fracture [53,54] , (c) quasi-cleavage (QC) and associated smooth translath boundary facet (B) [49] (d) quasi cleavage at higher magnification showing associated fine lath like features, tear ridges [11]

2.5 Hydrogen Embrittlement Mechanisms

2.5.1 Pressure theory:

Zappfe [55] proposed the pressure theory in 1950 which postulates that hydrogen, after entering the material, preferentially saturates the internal voids and the pores. Large internal gaseous hydrogen pressure builds up until a critical pressure when the lattice ruptures. The simple pressure theory cannot explain hydrogen assisted failure at low hydrogen partial pressures.

2.5.2 Hydride formation theory:

In 1969 the hydride formation theory was proposed by Westlake [56]. In this model, after entering the material hydrogen interacts with those alloying elements (Zr, Ti, Ta, Ni, V, etc.) susceptible to forming hydrides as shown symbolically in Eqn. 1. The brittle hydride particles offer a low energy fracture path thus facilitating fracture. However, hydrides do not form in many alloys known to be susceptible to hydrogen embrittlement and thus has very limited potential applicability.

$$M^{x+} + xH = MH_x \quad (M = Zr, Ti, Ta, Ni, V \text{ etc}) \qquad (1)$$

2.5.3 Crack tip surface adsorption theory:

Petch and Stables [57] introduced the surface adsorption theory in 1952 that considered hydrogen adsorption at the crack tip surface lowers the surface energy at crack tip. Reduced surface energies would certainly facilitate crack propagation, but many details of the hydrogen-induced fracture process were left unexplained.

2.5.4 Hydrogen enhanced decohesion:

Over the span of approximately a decade in the late 1950s through the early 1970s, Troiano et al. [38], Oriani et al. [58], Johnson et al. [59] advanced concepts involving hydrogen enhaced lattice decohesion. After a sufficient amount of hydrogen migrates to a local region, the electrons contributed by the atomic hydrogen interfere with the electron cloud of metallic atoms in the parent lattice and reduce the cohesive bonding between the atoms of the parent lattice. Although decohesion theory explains interaction of hydrogen on an atomic scale, decohesion theory fails to explain hydrogen assisted failure at low hydrogen concentrations.

2.5.5 Hydrogen enhanced localized plasticity (HELP):

In 1972 Beachem [60] postulated that the presence of hydrogen in the lattice could lead to a macroscopically brittle failure by enhancing local plasticity. This somewhat surprising proposal is called hydrogen enhanced localized plasticity (HELP) and the mechanism considers the interaction of hydrogen atoms and dislocations at the atomic level to better understand hydrogen-induced brittle failures.

The HELP theory asserts that hydrogen, after entering the material, preferentially migrates to the tensile zone of an edge dislocation strain field [see Figure 2.17 (a)] and reduces the lattice strain energy associated with the tension locally. Reduction of the strain energy of dislocations in a dislocation pile-up as shown in Figure 2.17 (a) would lower the repulsive forces between adjacent dislocations, decrease the spacing between adjacent dislocations and enable more dislocations to join the pile-up [61,62] as shown schematically in Figure 2.17 (b) [61]. Increased numbers of dislocations in pile-ups would naturally lead to amplified stresses and

strains imposed against the microstructural features responsible for the pile-up, e.g., grain boundaries (GB), carbide particles, etc., and facilitate crack nucleation at the front of the pile-up.

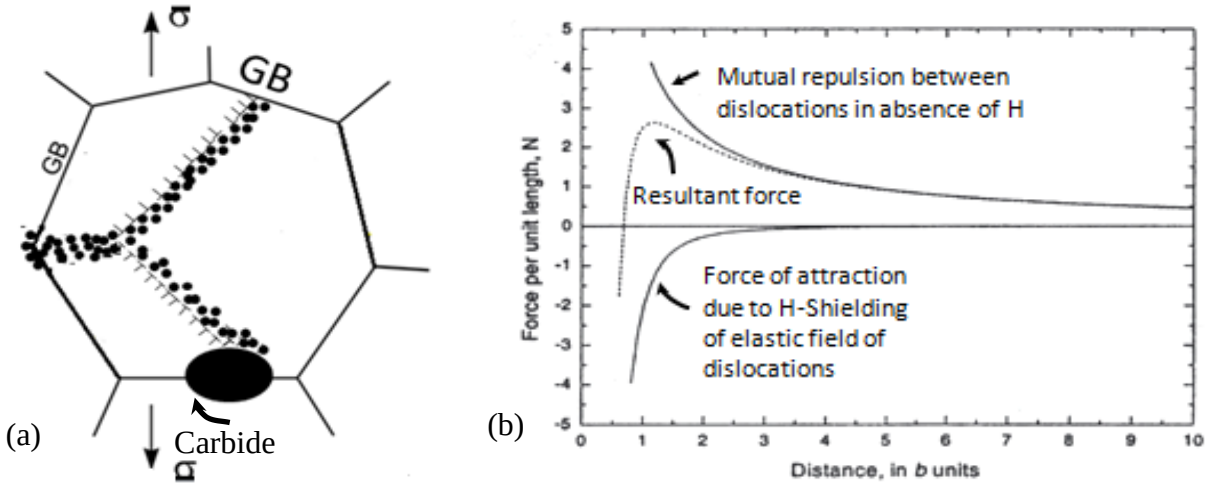

Figure 2.17 (a) Hydrogen occupying dislocation strain filed, enhances dislocation motions and dislocation pile ups against GBs and second phase carbide precipitate at GBs; (b) Hydrogen induced shielding effect resulting decrease in mutual repulsion between dislocations [61]

Figure 2.18 [63] is a set of transmission electron micrograph (TEM) images of α-Ti alloy. The pictures were taken in-situ at different points of time after hydrogen absorption in an atmosphere of 100 torr H_2. The pictorial sequence illustrates how the presence of hydrogen in the lattice enhances dislocation movement in the field of view of the image while the experimental stage was kept fixed in place. Note in Figure 2.18 the sequential movement of dislocation #4 with respect to the location of dislocation #5. [63]

Figure 2.19 [64] shows TEM images of a dislocation pile-up in stainless steel. The pictures were taken in-situ for a sample that was initially hydrogen-free (i.e., 0 Torr hydrogen) and then in a hydrogenated condition (i.e., 95 Torr hydrogen). A negative image (i.e., black

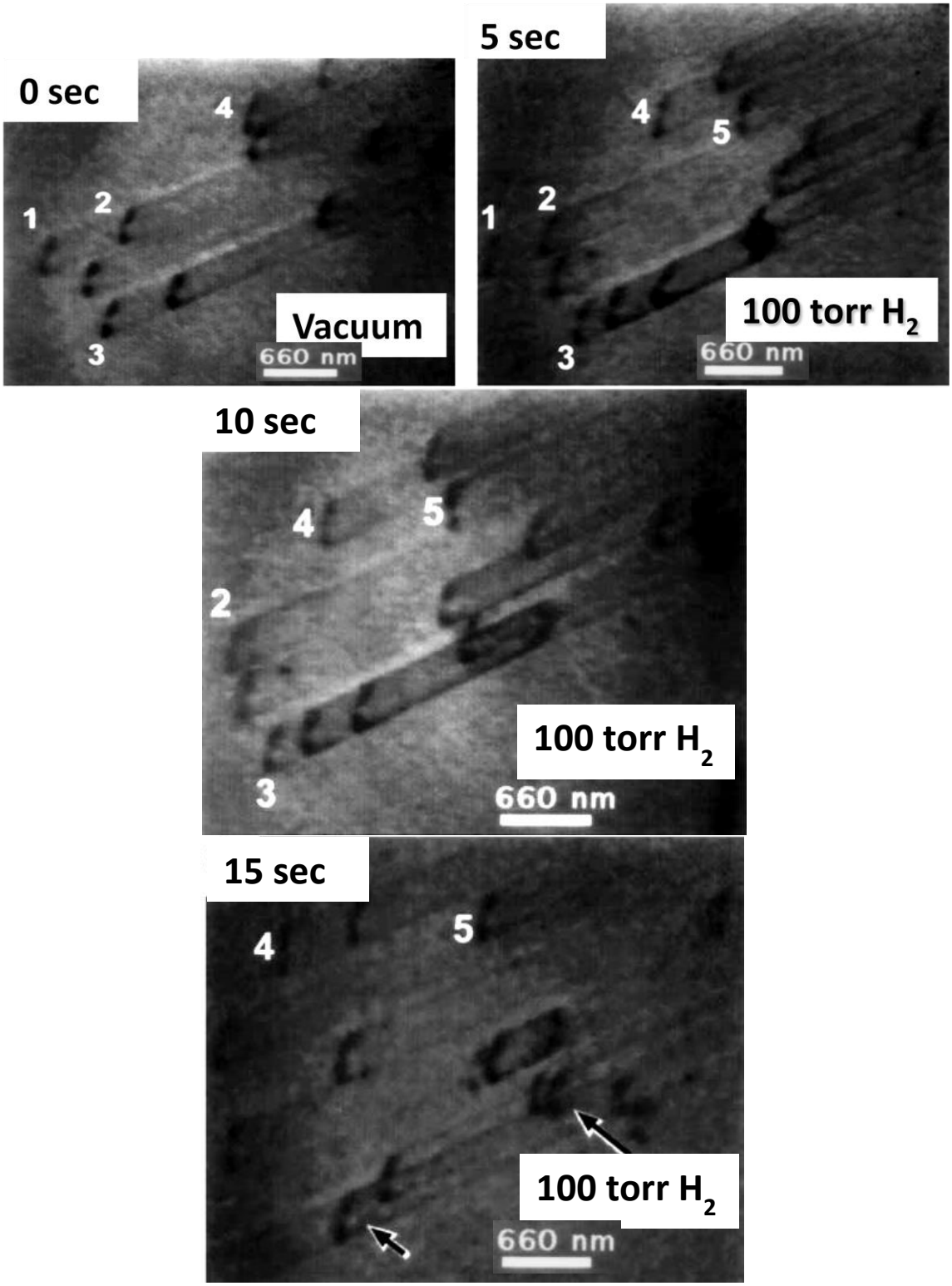

Figure 2.18. Presence of hydrogen enhances dislocation movement. Note the sequential movement of dislocation #4 with respect to the location of dislocation #5. [63]

becomes white) of the hydrogenated sample is then superimposed on the positive image of the hydrogen-free sample to facilitate comparison of the positions of the dislocations in the pile-up. The separation distances between the dislocations in the pile-up clearly decrease in the presence of hydrogen.

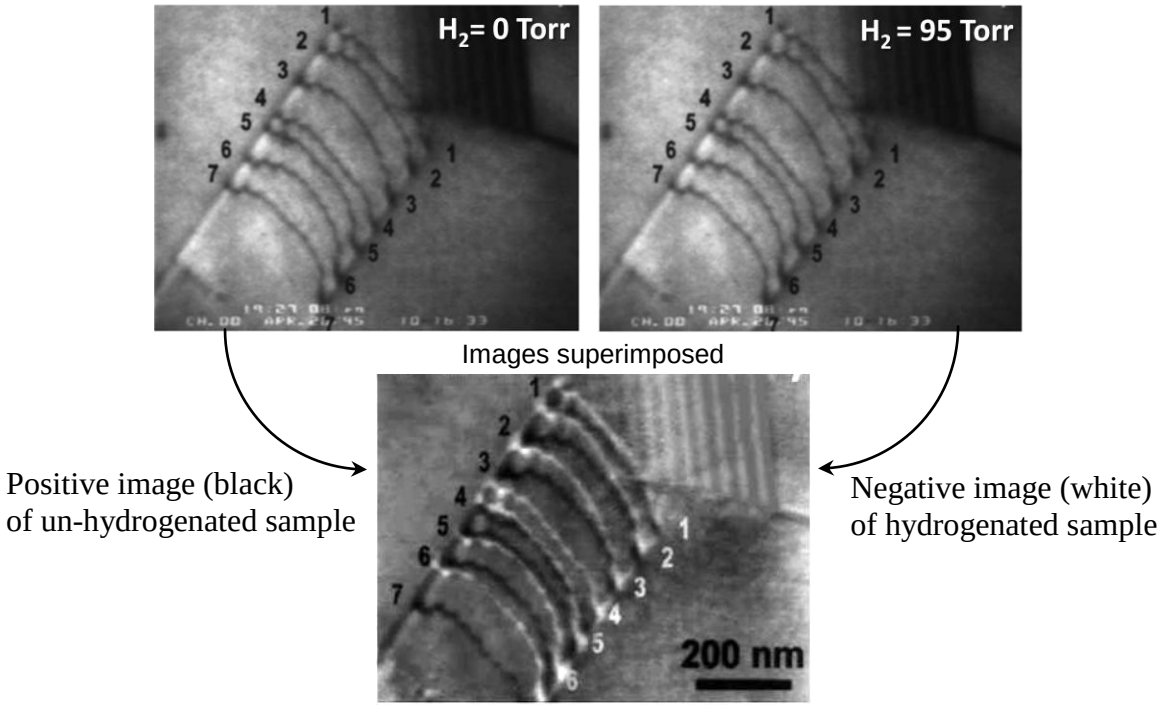

Fig. 2.19 Hydrogen enhanced dislocation pile ups [64].

Unfortunately, none of these individual mechanisms can explain all the observations related to hydrogen-induced failures and researchers are currently looking to integrate multiple mechanisms to more systematically explain experimental results. This is known as the synergistic approach [3, 65, 66].

2.6. Tempered Martensite Embrittlement

Tempered martensite embrittlement (TME) is commonly observed in commercial high strength, low alloy steel (σ_y > = 200 ksi) and is often known as 350^{o}C embrittlement or one step embrittlement. TME embrittlement is observed when the as-quenched martensite is tempered in the temperature range of 250 -350^{o}C for relatively short times (<= 2h) [67]. Tempered martensite embrittlement causes brittle intergranular failures even in absence of hydrogen.

Early researchers suggested that the mechanism of tempered martensitic embrittlement to be the result of formation of a fine dispersion of transition metal carbides (mainly cementite) during tempering in a specific temperature range (usually < 350^{o}C). The carbides were thought to be globular carbide particle dispersed in the matrix or elongated carbide films at martensitic boundaries (or prior austenitic grain boundaries) or as both globular and platelet carbides within the martensite laths or plates [68, 69]. However, the onset of the embrittlement was always coincident with the beginning of the precipitation of cementite platelets at PAGBs. Tempering above 370^{o}C resulted in coalescence of the cementite particles, softening of the matrix and increased toughness [69].

Schrader et al. [70] suggested TME intergranular embrittlement to be effect of precipitation of nitrides of chromium or magnesium at grain boundaries when he observed the elimination of toughness trough in magnesium steel in presence of ~ 0.01% Al. However, nitride formation did not explain why an increase in P and/or S would increase the severity of hydrogen embrittlement as often reported in these steels.

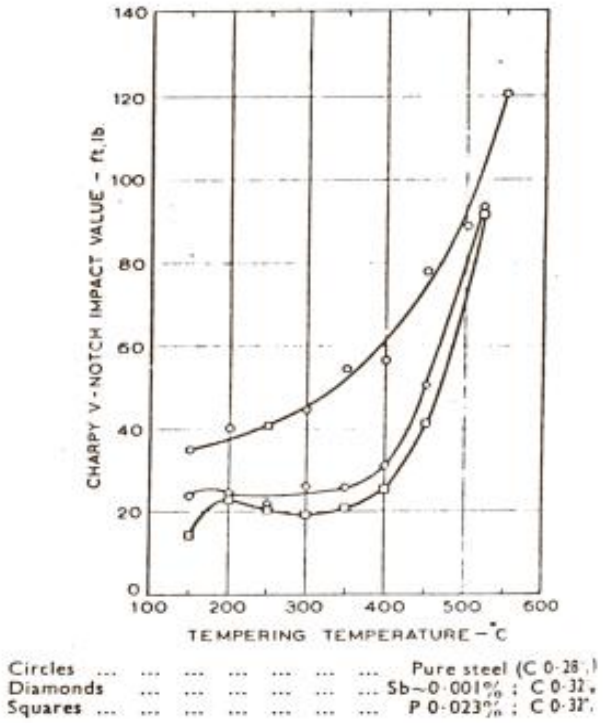

Fig. 2.20 Influence of impurity elements on impact strength of hardened, tempered high purity 1.5 Ni-Cr-Mo Alloy [71]

Capus et al. [71] studied the effect of trace elements on tempered martensite embrittlement by analyzing the impact properties of high purity and commercial purity Ni-Cr-Mo steel. Within the tempering range of 300 - 350^{o}C they found a typical embrittlement trough (i.e., reduction in toughness) in case of commercial Ni-Cr-Mo but no such trough for the high purity alloy. See Figure 2.20. Capus et al. [71] concluded that the structural changes associated with the tempering of martensite were not solely responsible for tempered martensite embrittlement but that segregation of some impurity elements at the grain boundaries in the prior austenite phase played a significant role.

A number of segregation mechanisms of the impurity elements have been suggested. Of them, Kula and Anctil [72] proposed that the alloying elements in the cementite and ferrite phases would tend to diffuse and redistribute themselves after completion of cementite precipitation at higher temperatures. Certain impurity elements which are more soluble in ferrite would be preferentially rejected from the precipitated carbides, enriching the ferrite phase immediate adjacent to the thin elongated cementite platelets and causing embrittlement by lowering the ferrite-carbide interfacial energy. Rellick and McMahon [73] noted that P or S impurity rejection at the time of carbide precipitation is more important than redistribution after precipitation.

King et al. [74] performed low temperature (0 and -100^{o}C) toughness measurements and fractographic observation on quenched and tempered 0.6 % c steel. The minimums for the K_{IC} vs T_{temper} curve were observed to be at 297^{o}C for the 0^{o}C toughness measurements and 392^{o}C for the 100^{o}C toughness measurements. The corresponding fracture behavior was observed to be 100 % transgranular cleavage across the martensitic packets rather than intergranular failure along prior austenitic grain boundaries or crack paths along martensitic lath edges. King et al believed these observations to result from formation of larger crack nuclei by coarsening of the interlath cementite particles during tempering.

Some researchers [75-77] have examined the role of retained austenitic and its subsequent transformation into interlath cementite during tempering. Horn and Ritchie [76] postulated a fracture mechanism of interlath cleavage when the volume fraction of retained austenite is relatively large and a mixture of cleavage and microvoid coalescence when volume fraction of retained austenite is less.

However, these carbide-induced mechanisms of tempered martensitic embrittlement do not satisfactorily explain how an increase in P and/or S content in commercial steels would enhance the susceptibility to embrittlement. Krauss et al. [77] performed impact property measurements and fractographic analysis of quenched and tempered 4340 steels with two different P compositions (0.003 wt % and 0.03 wt %). They found that for lower P content steels, the mechanism of brittle fracture involved interlath cementite platelets and subsequent crack propagation across the martensite laths. The interlath cementite platelets are formed by the transformation of retained austenite during the tempering stage. Steels containing higher amounts of phosphorous exhibited extensive intergranular fracture along the prior austenitic grain boundaries. In the latter case, the embrittlement mechanism is suggested to be the combined effect of phosphorous segregation and grain boundary carbides formed during tempering.

In brief, the three major mechanisms of tempered martensite embrittlement can be summarized as (i) embrittlement resulting from grain boundary weakening due to the combined effects of impurity (P, S, Sn, Sb) segregation and post tempering (>150^{o}C) carbide formation, (ii) embrittlement resulting from the sole involvement of carbides without the involvement of any impurity element and (iii) embrittlement resulting from the involvement the interlath cementite formed from retained austenite during the tempering process.

2.7. Grain Size Effects of Embrittlement Behavior of Martensitic Steel

The role of prior austenite grain size in modifying the mechanical properties of quenched and tempered low alloy steels was originally recognized by Cotterill [78] , Troiano [79] and Elsea and Fletcher [80]. They found that a fine austenite grain size is desirable to achieve a good combination of strength and ductility in low alloy steel. However, the effects of prior austenitic

grain size on environmentally-induced cracking of 4340 steel was not extensively studied until the investigations of Proctor and Paxton [13], Quadrini [14], Lessar and Gerberich [15], Zackay et al [81], Wood [82], Lai et al. [83] and Parker and Zackay [84]. Unfortunately, the literature reports are in some disagreement regarding the effects of prior austenite grain sizes on crack nucleation and growth process in quenched and tempered low alloy steel.

Most of the research carried out until now have either directly or indirectly emphasized the function of austenite grain size on crack nucleation and growth rate and threshold stress intensity. Proctor and Paxton [13] demonstrated increasing failure times with decreasing prior austenite grain-size over a grain diameter range of 6-35 μm (ASTM grain size: 7-12). See Figure 2.21. In somewhat contradiction to this and as shown in Figure 2.22 (a, b), Lessar and Gerbarich [15] observed decreases in crack velocity and increases in threshold stress intensity with increase in the prior austenite grain size. However, Lessar and Gerberich [15] observed no significant grain size dependence of fracture behavior below 40 μm of grain size.

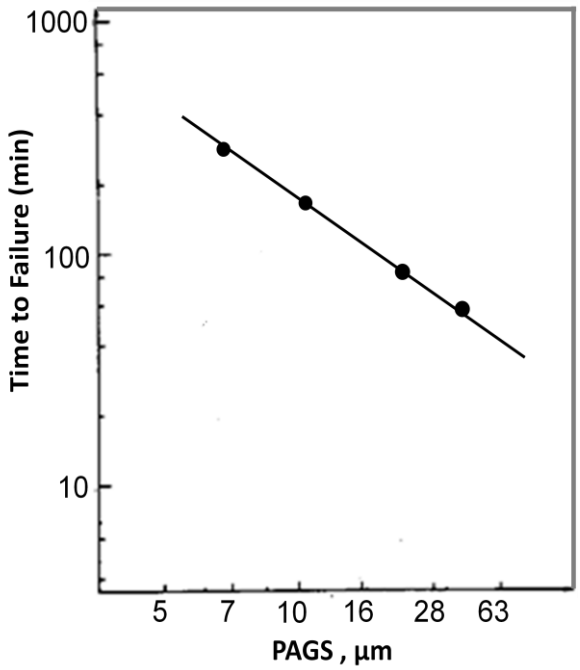

Fig. 2.21. Hall Petch plot of yield strength vs. (prior austenitic grain size)$^{-1/2}$ for 4340 steel [derived from Proctor and Paxton [13]

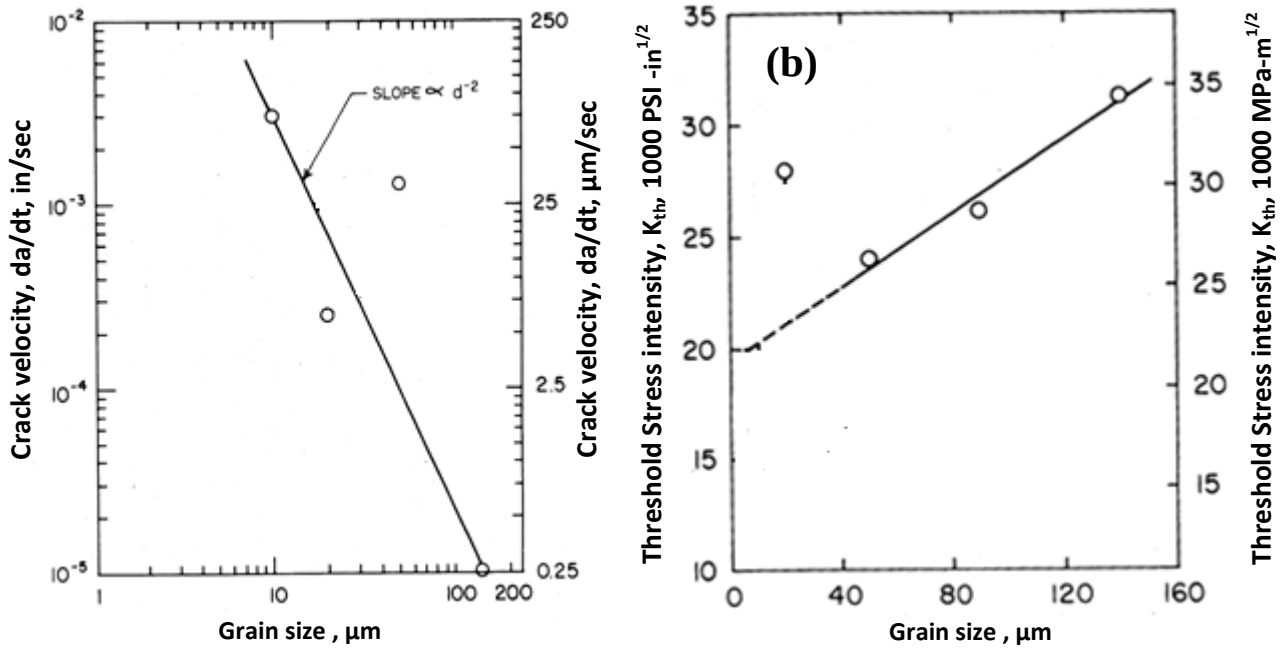

Fig. 2.22. (a) Crack velocity vs grain size , (b) threshold stress intensity vs grain size for 4340 steel. derived from Lessar and Gerberich [15].

In martensitic steel, the martensitic lath packet is one of the most important parameters controlling the mechanical properties and failure behavior. The morphology, size, orientation and the internal structure (block) and substructures (sub-block) of the martensitic lath packets are strongly related to prior austenitic grain size. Detailed discussions about the crystallographic orientation relationships are available elsewhere [85-88]. A schematic of lath martensitic microstructure is shown in Figure 2.23 [88].

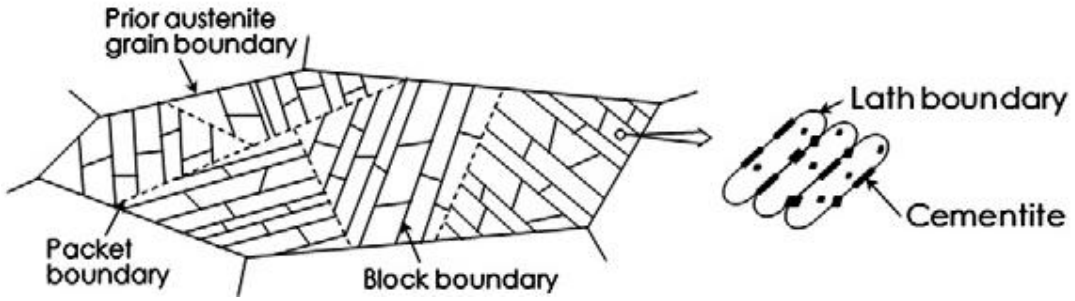

Fig. 2.23. Typical schematic of lath martensite microstructure. Prior austenitic grains are subdivided into martensite lath packets which are further subdivided into blocks and the blocks may further be subdivided into sub-blocks [88]

Morito et al. [80] presented the relationship of PAGS on the size of martensitic lath packets for Fe - 0.02 wt % C and Fe- 0.2 wt % C – 2 wt% Mn alloy and compared their findings with the result of Maki et al. [89]. Figure 2.24 shows that the size of the martensitic lath packets formed within the individual grains increase with increase in PAGS. No effect was reported for Mn additions. However, Mn additions were observed to increase the number blocks constituting the martensitic lath. As a result, for a given PAGS, the block sizes constituting the martensitic lath were observed to be smaller in presence of Mn. See Figure 2.25.

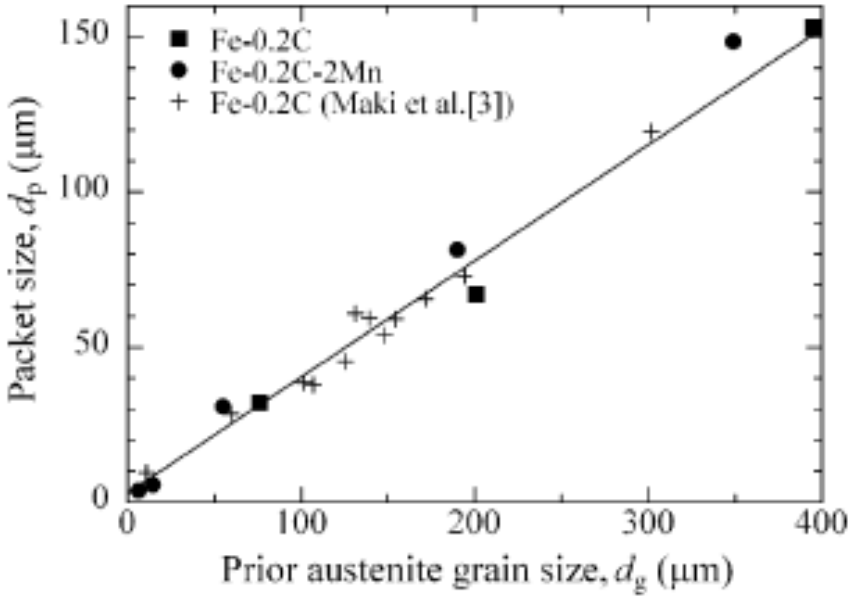

Fig. 2.24. Size of martensitic lath packets vs prior austenitic grain size in Fe- 0.2 wt % C and Fe- 0.2 wt % C – 2 wt% Mn alloy [85] .

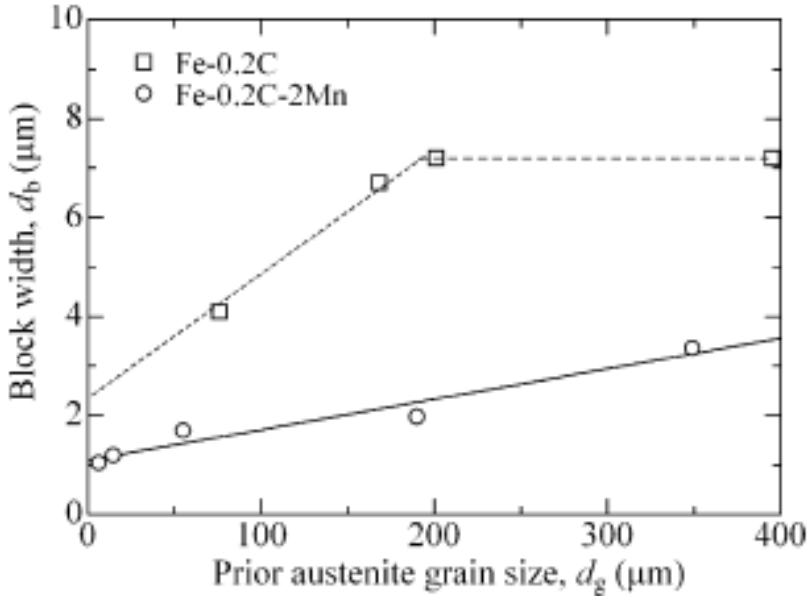

Fig. 2.25. Width of constituting blocks the martensitic lath packets vs prior austenitic grain size in Fe- 0.2 wt % C and Fe- 0.2 wt % C – 2 wt% Mn alloy [85].

Morito et al. [85] observed the size effect of the martensitic lath packets as well as the size of their constituent blocks on the mechanical behavior of Fe – 0.2 wt% C – 2 wt% Mn alloy. They compared their results with the results of Swarr and Krauss [90] for Mn-free Fe- 0.2 wt% C as shown in Figure 2.26. Reductions in mechanical strength in terms of 0.2 % yield stress were observed with increasing lath packet size and block size.

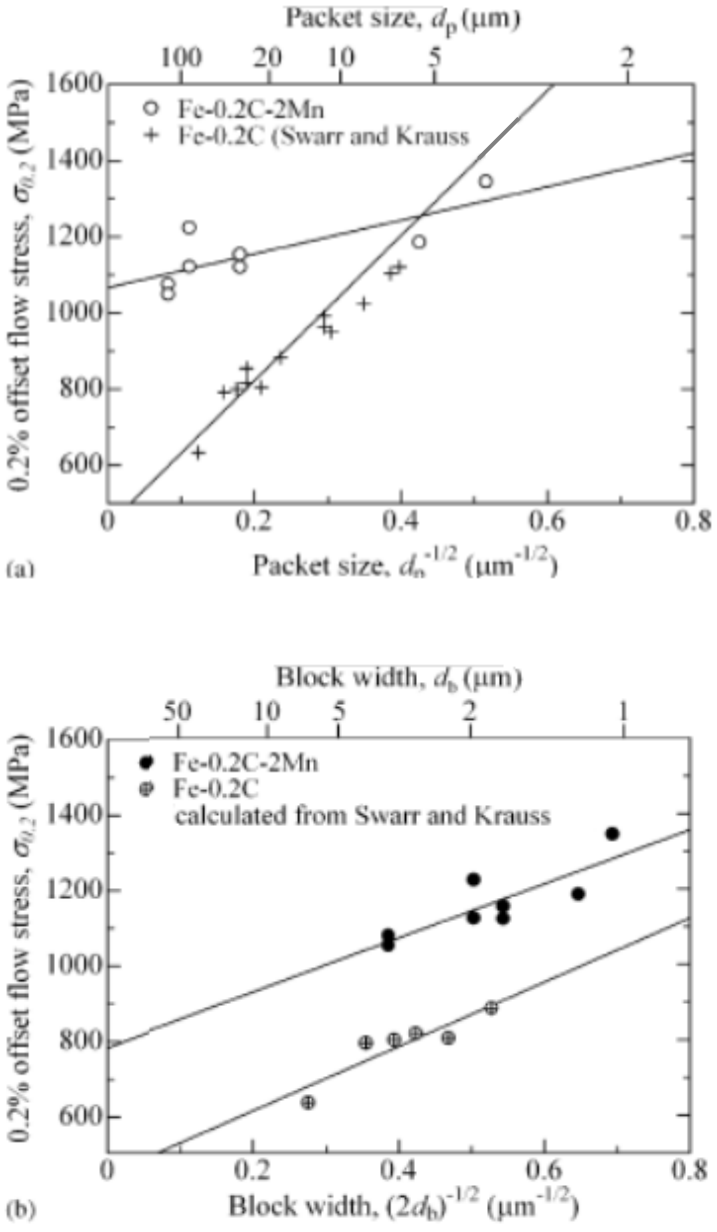

Fig. 2.26. Hall-Petch type plots (a) for yield strength vs. (packet size)$^{-1/2}$ (b) for yield strength vs. (block size)$^{-1/2}$ [85]

3. Experimental Procedures

3.1 Sample Configurations and Preparations

3.1.1 V-notch 4-point Bend Sample

V-notch 4-point bend samples per ASTM F-519 (See Figure 3.1) [91] were used to perform the compatibility study of vaporized hydrogen peroxide (VHP) on 4340 steel. Aerospace grade, low alloy high-strength AISI 4340 plate (thickness 63.5mm, AMS 6359, see Table 1) was acquired from Lukens Steel (Coatesville, PA) and machined by Metal Samples Company (Munford, AL) into round tensile bars and square blanks for 4-point ending samples. The original longitudinal orientation of the plate was maintained in the machined tensile bars and the 4-point bending samples. The rough-machined, square bar blanks were 56 mm in length and 10 mm on each side.

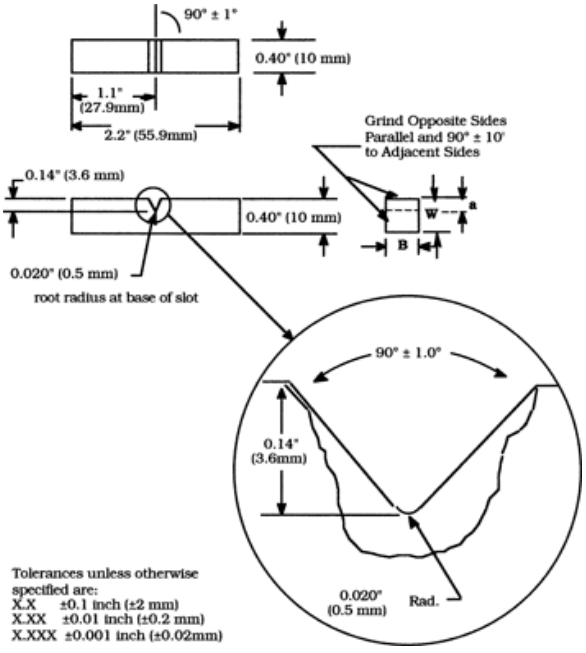

Fig. 3.1 4 - point bend sample per ASTM F-519 [86].

Table I. Composition of the 4-point bend test specimens of AISI 4340 (provided by vendor)

Element	C	Cr	Mn	Ni	P	Si	S	Al	Fe
Composition (Wt %)	0.39	0.88	0.65	1.69	0.005	0.25	0.1	0.03	Bal

The rough machined blanks and accompanying tensile bars were austenitized at 830±10°C in argon atmosphere, oil quenched, and then double tempered (220±10°C for 2 hours) at Auburn University (Auburn, AL). Finish machining of the test samples suitable for sustained-load, 4-point bend testing per ASTM F519-06 [86] was performed by Metal Samples Company (Munford, AL). The four-point bending samples exhibited center notches 3.5 mm deep with a radius of 0.25 mm and 90° included angle (Type 1e Specimen). The notch was machined into the short transverse direction of the original plate. The stress concentration factor of the notch was 3.1. All samples were stress relieved at 190±10°C for 4.5 hours after final machining. The heat treat response of the material was verified by tensile and hardness testing of four samples per ASTM E8-00b [92]. A typical engineering stress – engineering strain curve is shown in Figure 3.2. The 0.2% yield strength, the tensile strength and the percent elongation (1.25 inch gage length) of the samples were measured as 1690±10 MPa, 1980±10 MPa and 14.5%±0.1%, respectively. The hardness was 52±1 on the Rockwell C scale.

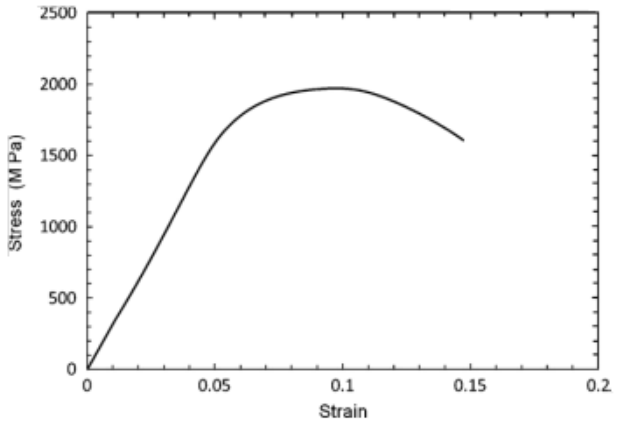

Fig. 3.2. Typical engineering stress–strain curve of the as-received 4340 steel alloy prior to hydrogen embrittlement testing.

3.1.2 Double Notch Round Bar Tensile Sample

Double notched tensile samples as shown in Figure 3.3 were used to study the hydrogen embrittlement effects due to electrochemical in-situ hydrogen charging. 4340 round bar tensile samples from the same heat [see Table II] were procured from Laboratory Devices Company (Placerville, CA). The diameter and the gage length of the samples were 6 mm and 58.5 mm, respectively. As received samples were austenitized in argon atmosphere, oil quenched, and then double tempered at Auburn University (Auburn, AL). The various austenitizing and tempering conditions and the resultant prior austenitic grain sizes (PAGS) and hardnesses are shown in Table III. All austenitizing at 1175^{o}C was accomplished by encapsulating the samples in a sealed quartz tube at 2-3 psi of argon pressure at room temperature. These samples were quenched by breaking the quartz tube after austenitization and then immediately quenching the samples.

Table II. Composition of the double notch tensile specimens of AISI 4340 (provided by vendor)

Element	C	Cr	Mn	Ni	P	Si	S	Cu	Al	Mo	N
Composition (wt %)	0.4	0.79	0.74	1.69	0.007	0.29	0.014	0.18	0.036	0.24	0.009

Table III. Post heat treatment PAGS and Martensitic Hardnesses

Austenitizing (^{o}C) [1h]	Tempering (^{o}C) [1h + 1h]		Tempering @ 350^{o}C	Tempering @ 500^{o}C	Tempering @ 350^{o}C	Tempering @ 500^{o}C
			Prior Austenitic Grain size (PAGS) ~ avg. nominal dia. in μm		Hardness (Rockwell C, HRC)	
870	350	500	10 ± 3	10 ± 3	51.5 ± 0.5	45± 0.5
1100	350	500	40 ± 10	40 ± 10	50 ± 0.5	43 ± 0.5
1175	350	500	100 ± 20	100 ± 20	48.5 ± 0.5	41 ± 0.5

After heat treatment, the samples were shipped to back to Laboratory Devices Company (Placerville, CA) where two semi-circular notches were ground according to the dimensions shown in the Fig. 3.3. After grinding of the notches, all samples were shipped back to Auburn University where they were stress-relieved at 190 ± 10^{o}C for 4.5 hours.

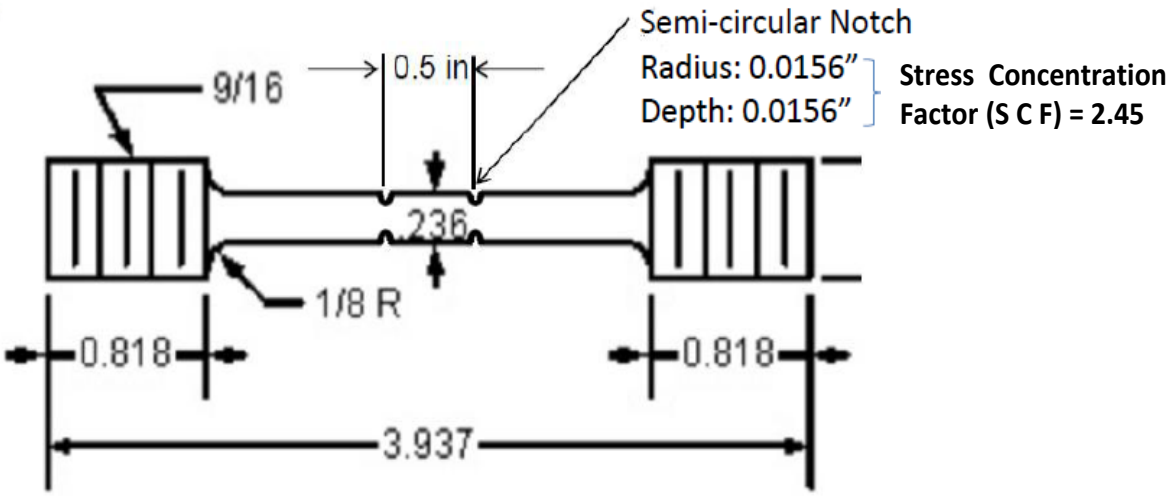

Figure 3.3. Double notched round bar tensile sample (measurements are given in inch)

3.2 Metallography

3.2.1. Microstructural Evaluation and PAGS Measurements

After the heat treatment one representative specimen from the whole batch of 4-point bend samples and one representative specimen from each of the six different heat treatment groups specified in Table III of the double-notched tensile samples were randomly chosen for the microstructural analysis and measurement of the prior austenitic grain sizes. Samples were sectioned transverse to their long axis for metallographic analysis. Sectioned samples were mounted in bakelite, ground and polished by standard metallographic techniques. Observation of the martensitic microstructures of the samples was enabled by etching the samples in 2% Nital (2 ml HNO_3 and 98 mL ethanol) while the prior austenitic grain boundaries were revealed by

etching with modified Winsteard's reagent (100 ml of 1.2% saturated aqueous solution of picric acid, 2.5 ml of 40% solution of sodium do-decyl benzene sulfonate as a wetting agent, 5 ml of ethanol, 10 drops of HCl). All etchants were applied by cotton swabs. Etching with Nital occurred at room temperature while etching with the modified Winstead's reagent was performed at 65-70^{o}C. Metallographic examination of the samples was performed with an Olympus PME3 optical microscope. Grain size measurements used the intercept method per ASTM E112-96 [93].

3.3 Hydrogen Charging and Mechanical Testing

3.3.1 Vapor Phase Charging by VHP Exposure and 4-Point Bend Test

A Model 2410 Lever Arm Tester (ATS, Butler, PA) was used to apply sustained 4-point bending loads to the test samples. See Figure 3.4. The notch fracture strength (NFS) of the 4-point bending samples was determined to be 205 ksi. Nonconductive kapton tape of 0.5 mm total thickness was placed between the 4340 samples and the 4 point-bending fixture to electrically isolate the samples from the loading frame and prevent any galvanic coupling between the dissimilar metals. Per ASTM 519E-06, the sensitivity of the lot of 4340 steel samples to hydrogen embrittlement was verified by electroplating three specimens in a highly-embrittling bright cadmium cyanide bath and three specimens under a less embrittling treatment Plating of the specimens was performed by Westfield Plating Co. (Westfield, MA). The highly embrittling bath contained 33.7 g/L cadmium (as CdO), 104 g/L NaCN, and 18.7 g/L NaOH. The pH of the bath was 12 and the operating temperature was 21-32^{o}C. Samples were electroplated at 108 A/m^2 for 30 min. The composition and process condition of the bath for the less embrittling treatment was the same except that samples were electroplated at 645 A/m^2 for 6 min and then baked in air at 190±14^{o}C for 23 hr. As required by ASTM 519E-06, all three specimens plated in the highly embrittling bath fractured within 24 hours under sustained bending loads of 75% of the net fracture strength of the samples while none of the three samples plated in the less embrittling bath fractured within 200 hours under the same loads.

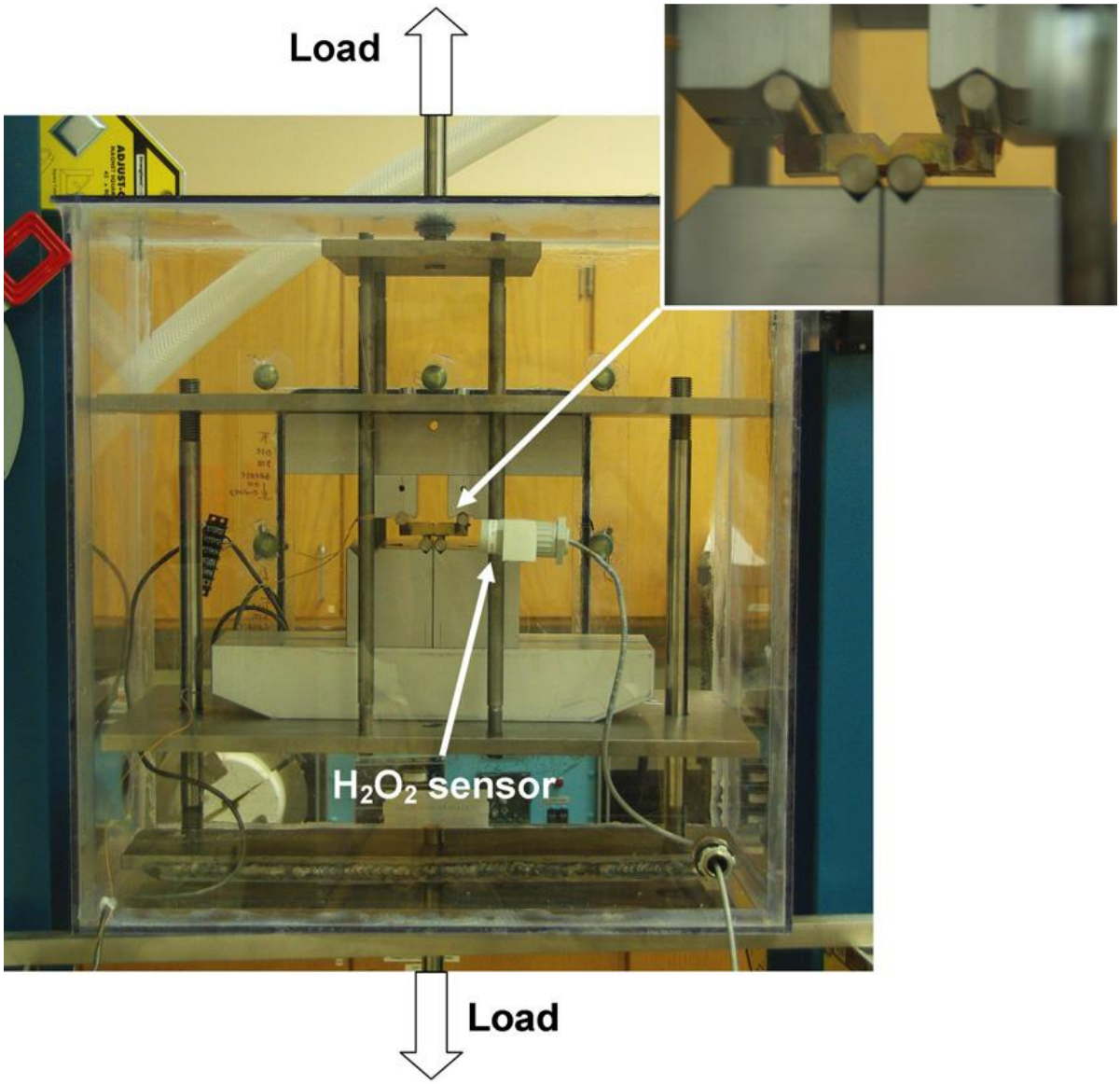

Fig. 3.4 Mechanical test system for application of sustained 4-point bending loads in a vaporized hydrogen peroxide isolation chamber.

All sample exposures to vaporized hydrogen peroxide were performed with a Steris 1000ED Bio-decontamination Unit (Mentor, OH) using Vaprox (35 wt. % H_2O_2) as the sterilant in the enclosed chamber. The exposure chamber was dehumidified to 10% relative humidity prior to hydrogen peroxide injection to minimize any chance of unintended condensation of the

hydrogen peroxide vapor. The ramp-up conditioning phase of hydrogen peroxide injection was accomplished in 10 min. Samples were then subjected to the desired hydrogen peroxide vapor concentration (500, 1000, 1300 or 1600 ppm) under a sustained bending stress level of 45% of the notched fracture strength for 4.8 hr of decontamination without any subsequent aeration. The lack of an aeration phase was intended to provide a worst case exposure to the hydrogen peroxide. After completion of the 4.8 hr exposure, the stress level was immediately increased to 75% of the NFS for 200 hr. Hydrogen peroxide concentrations in the exposure chamber were monitored with ATI Sensors (ATI Inc., Collegeville, PA, USA). These sensors are reported by the manufacturer as having an accuracy of $\pm$5% at concentrations above ~50ppm.

The temperature of the exposure chamber increased from room temperature at the beginning of bio-decontamination to 30-35^{o}C after approximately 75 min of cycle time. The temperature then stayed constant until the end of the 4.8 hr bio-decontamination cycle after which it slowly decreased back to room temperature.

Samples that did not fracture at 75% NFS within the 200 hr test period were incrementally step loaded (ISL) by increasing the load in 5% increments for 2 hours at each incremental load (i.e., 80% NFS for 2 hours, then 85% NFS for 2 hours, then 90% NFS for 2 hours). This procedure was continued until sample failure.

Some exposure conditions led to visible condensation within the chamber and on the samples. Hydrogen peroxide concentrations of liquid condensates from the hydrogen peroxide/water vapor treatments were estimated using the standard sulfuric acid solution titration with potassium permanganate [94].

The susceptibility to hydrogen embrittlement from exposure to low concentrations of hydrogen peroxide/water liquid solutions was examined by placing droplets of 35 wt. % H_2O_2

/ H_2O for 4.8 hours in the notches of loaded samples as well as on the overall sample surface. To ensure that the solution remained fresh, the solutions were replaced each hour during the total exposure period and the chamber was humidified and heated to conditions comparable to vaporized hydrogen peroxide treatment by injecting only water vapor into the chamber from the Steris 1000ED Bio-decontamination Unit.

Note that neither the vapor-exposures nor the liquid-exposures were designed as accelerated aging tests but were designed simply to investigate the susceptibility to hydrogen embrittlement of high-strength 4340 steel under a variety of chemical service environments associated with vaporized hydrogen peroxide processes. The 75% NFS loading for 200 hours is considered "aggressive." The actual applicability of the test results contained in this paper for any specific application should be considered on a case-by-case basis.

Examination of the fracture surfaces of samples was performed using a JEOL JSM 7000F field emission scanning electron microscope operating at 20kV with energy dispersive X-ray spectroscopy (EDS) employing an ultrathin window detector and Princeton Gamma-Tech analyzer.

3.3.2 In-situ Electrochemical Charging and Tensile Test

The in-situ hydrogen charging and tensile loading process is shown in Fig. 3.6. The double-notched tensile samples were electrochemically charged in-situ with hydrogen in 0.5 M H_2SO_4 + 5ml/g As_2O_3 solution for different time durations (0, 5, 10, 20, 30 and 40 min) with a current density of 10 mA/cm^2 (characterized with respect to the surface area of the sample exposed to electrolyte). 99.95 % pure platinum wire with nominal diameter of 0.5 mm (from Alfa Acer) was used as the anode. The samples were always located at the central position of the platinum coil with the coil diameter of approximately 4 cm. To facilitate uniformity in this

arrangement and maintain a constant distance between the platinum coil and the sample, the location of the platinum wire was reliably established by winding the wire against a fixed support. In order maintain electrical isolation between the sample and the fixture of the Q-Test machine, the portions of the fixtures (bolt heads) inside the electrolyte were sealed by using electrolyte resistant and leak resistant silicone rubber sealant. After the samples were screwed into the fixture thread, junctions between the sample and the bolt heads were also sealed using silicone rubber. This arrangement ensured the physical as well as electrical isolation of electrolyte from the tensile machine and the entire electrochemical charging set was isolated from the tensile machine.

After electrochemical charging was completed, the electrolyte was removed (in about 10 sec) from the charging cell and tensile testing started immediately at cross head speeds of 0.01 mm/min and 0.03 mm/min using a Q-Test Elite 100 tensile testing machine (MTS Systems Corporation). All tests were repeated 3-5 times at each test condition.

The samples failed along either of the two notches (top or bottom). No practical bias was seen for fracture preference of either of the two notches. Examination of the fracture surfaces of the broken notch of the samples was performed using a JEOLJSM7000F field emission scanning electron microscope operating at 20 kV with energy dispersive X-ray spectroscopy (EDS) employing an ultrathin window detector and Princeton Gamma-Tech analyzer.

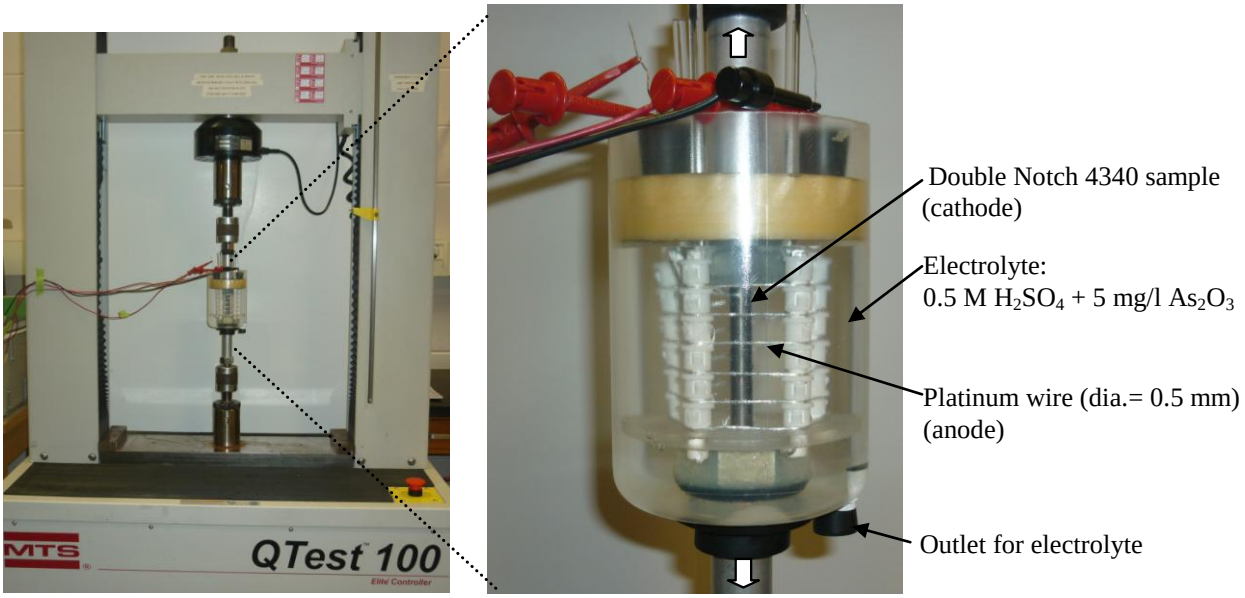

Fig. 3.5 Hydrogen charging apparatus was mounted on the tensile instrument (MTS Q-Test). Samples were charged with hydrogen and immediately loaded under tension at cross head speed of 0.01 and 0.03 mm/min and the electrolyte was simultaneously removed

3.4 Quantitative Fractographic Measurement

Quantitative fractography was performed only for the double notch tensile samples. Data quantifying the percentages of the various fractures modes (i.e., intergranular, quasi cleavage, flat cleavage like or dimpled) were obtained from the notch root along a radial line to a depth of ~1000 μm using intervals of 100μm and then down to the center of the sample using intervals of 500 μm. Sampling lines normal to the radial line were drawn on the micrographs of the fracture surfaces and of the percentages of the fracture modes exhibited estimated visually. Appendix #1 provides a typical example to illustrate the process.

4. Results and Discussions

4.1 Microstructural Result

4.1.1 Microstructure of the V- Notch Bend Sample

Fig. 4.1(a) shows the martensitic microstructure of the quenched and double tempered 4340 V-notch bend sample. No detectable microstructural changes occurred as a result of the various exposures to hydrogen peroxide. The prior austenite grains are shown in Figure 4.1(b) and exhibit an average grain diameter of 14±3 μm, which is equivalent to an ASTM grain size number of 9.

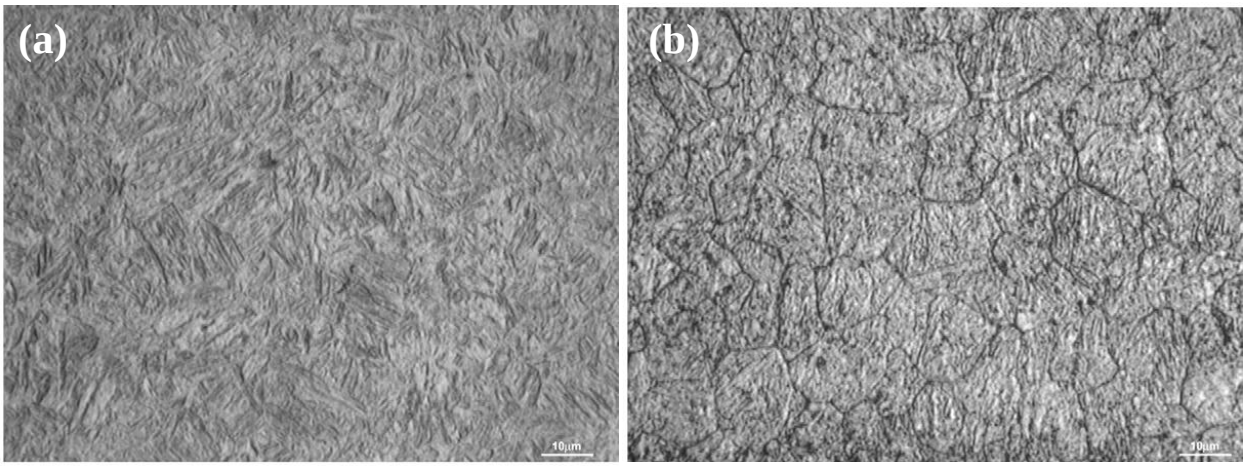

Fig. 4.1 (a) Martensitic microstructure of the heat treated 4340 steel samples (2% nital etchant, HRC= 52). (b) Prior austenitic grain boundaries of the heat treated steel samples (modified Winsteard's reagent).

4.1.2. Microstructure of the Double Notch Tensile Samples

Fig. 4.2 (a)-(f) show SEM images of the prior austenitic grain sizes (PAGS) for the double notch tensile samples subjected to heat treatment at six different conditions (see chap.3,

Table III). As expected, increasing the austenitizing temperatures led to increases in the observed PAGS.

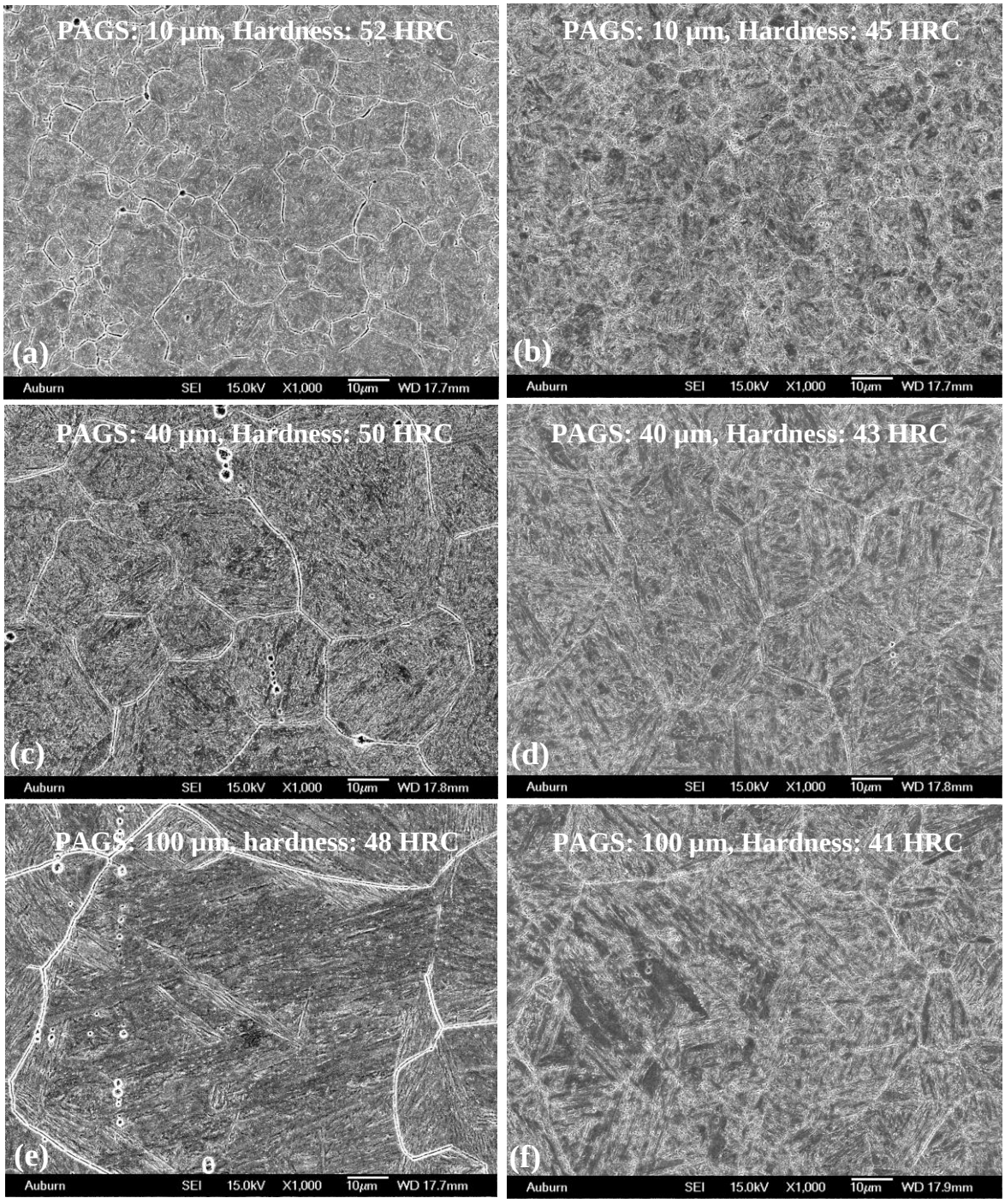

Fig. 4.2 SEM images of the modified Winsteard's reagent etched metallographic samples revealing PAGS at six different conditions annotated in the respective pictures.

Follow-on tempering of the austenitized and quenched samples resulted in a range of martensitic hardnesses as indicated in the Fig. 4.2. No significant differences in PAGS were observed due to the various tempering procedures. However, the PAGB for tempering temperature 350^{o}C were revealed more prominently compared to a tempering temperature of 500^{o}C, presumably because of favorably segregation of alloying elements (like P, S).

Fig. 4.3 (a)-(f) show light microscopic images of the prior austenitic grain sizes (PAGS) for the double notch tensile samples subjected to heat treatment at six different conditions (see chap.3, Table III).

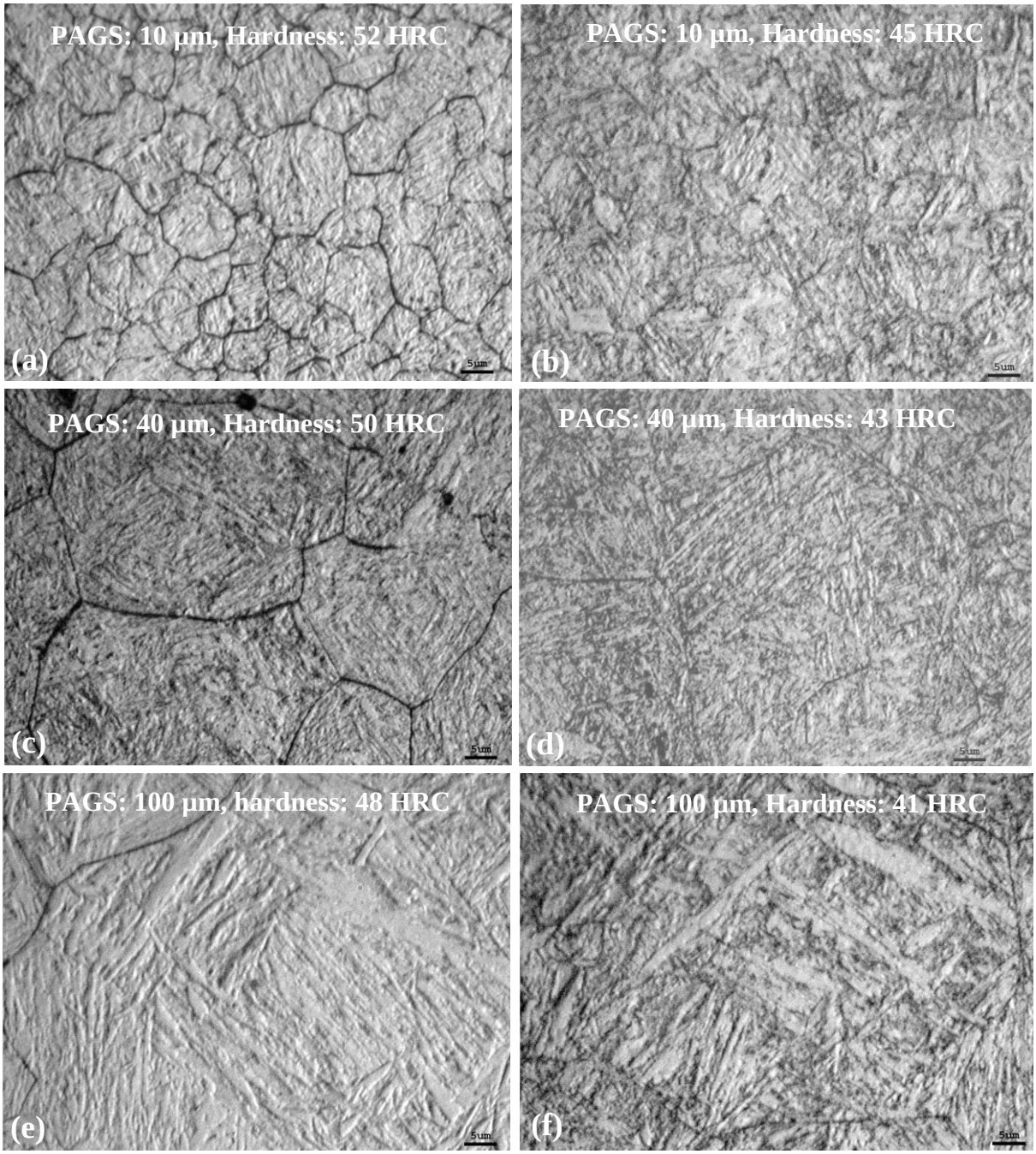

Fig. 4.3 Light microscopic images of the modified Winsteard's reagent etched metallographic samples showing prior austenitic grain sizes (modified Winstead's reagent) achieved at six different heat treatment conditions. Austenitized and tempered at (a) 870^{o}C (1h) and 350^{o}C (2h) , (b) 870^{o}C (1h) and 500^{o}C (2h), (c) 1100^{o}C (1h) and 350^{o}C (2h) , (d) 1100^{o}C(1h) and 500^{o}C, (e) 1175^{o}C (1h) and 350^{o}C (2h) , (f) 1175^{o}C (1h) and 500^{o}C (2h) (2h). Prior austenitic grain sizes and hardnesses are shown in the respective pictures.

In light microscopic images the martensitic packets and the individual blocks are more clearly observed compared to the SEM images. Martensitic packets inside the prior austenitic grains are identified only on the basis of eye observation of the group of blocks/laths with similar alignments. The average sizes of the blocks inside the martensitic grain are also eye estimated. Packets size and block width increased with increasing PAGS but remained unchanged with tempering temperatures. Average number of l packets per grain and average width of block constituting the packets are summarized in Table IV.

Table IV. Average size of the martensitic packets and their constituent blocks as function of grain size.

	~ 10 µm	~ 40 µm	~ 100 µm
Number of lath packets per grain	1	2-3	2-4
Packet size (µm)	10µm	20 ± 5µm	40 ± 10 µm
lath width (µm)	0.5-1 µm	`1-2 µm	1-3 µm

4.2 VHP Exposure Results

4.2.1 Mechanical Response

The hydrogen embrittlement results from the four-point bending tests are summarized in Fig. 4.4. In Fig. 4.4 each "√" mark indicates a sample that survived for the indicated times at the noted H_2O_2 concentration level and applied mechanical load. In contrast, an "X" mark in Fig. 4.4 indicates a sample that fractured during the indicated times at the noted H_2O_2 concentration level and applied mechanical load. ASTM Standard F519-06 states that a chemical service environment can be considered non-embrittling if none of 4 samples exposed to the environment (exposed while loaded at 45% of the notched fracture stress) fracture under sustained load of 75% of the notched fracture stress within 200 hrs after completion of the chemical exposure.

The data shown in Fig. 4.4 indicate that vaporized hydrogen peroxide levels of 500 and 1000 ppm were not embrittling to the 4340 high strength steel samples investigated here.

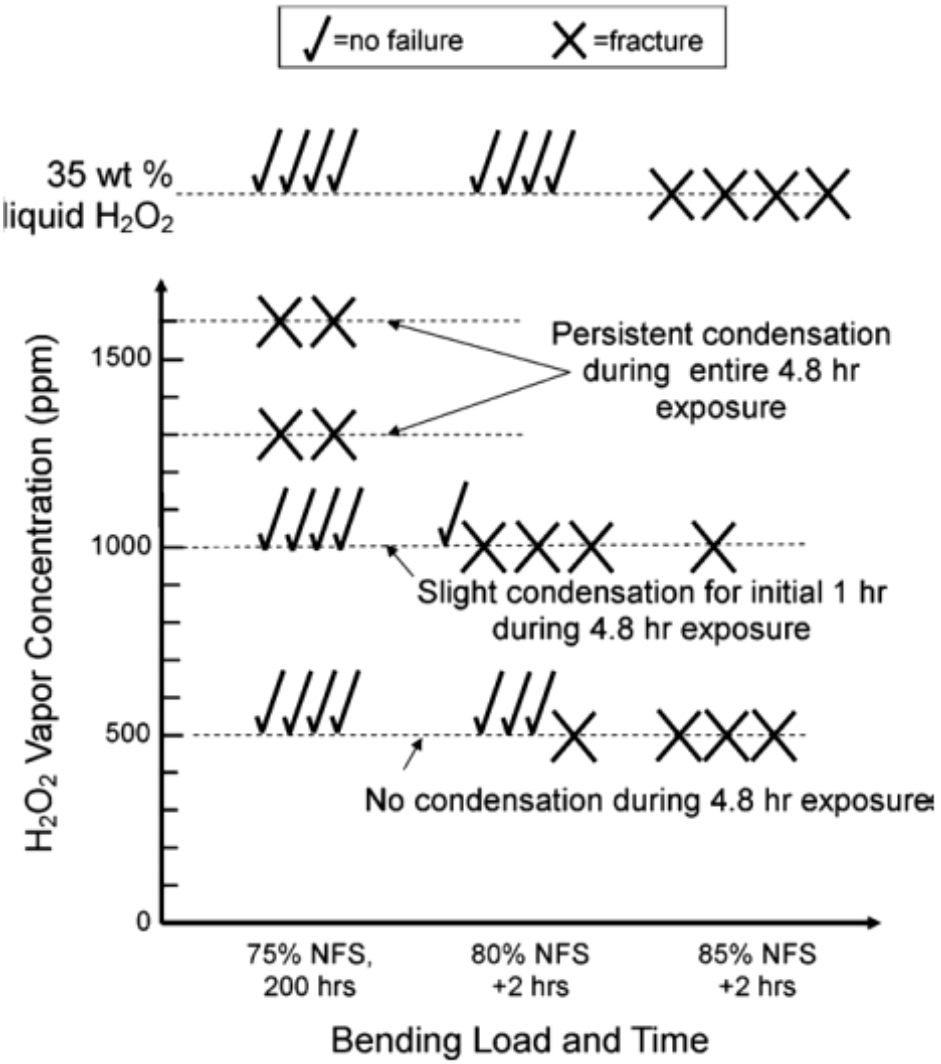

Fig. 4.4 Hydrogen embrittlement results for the hydrogen peroxide exposure concentrations, exposure times and mechanical loads shown. Note the indicated appearance of condensation during some treatments

Atomic hydrogen can be generated from thermal dissociation of hydrogen peroxide vapor according to

$$H_2O_2 \rightarrow H_2 + O_2 \qquad (1)$$

followed by dissociation to surface adsorbed atomic hydrogen as

$$H_2 \rightarrow 2H_{adsorbed} \quad . \qquad (2)$$

The adsorbed atomic hydrogen can then diffuse into the metallic lattice leading to possible hydrogen embrittlement. The equilibrium partial pressure for the reaction of Eq. (1)

$$K = \frac{p_{H_2O_2}}{p_{H_2} * p_{O_2}} \quad ,. \qquad (3)$$

using Eq. (3) and standard data [95] at 27°C with p_{O_2}= 0.21 atm. and $p_{H_2O_2}$ = 0.0016 atm. (equivalent to 1600 ppm), is 10^{-28} atm. This extremely low partial pressure of hydrogen gas generated from purely vapor phase hydrogen peroxide is consistent with the present experimental result of no measured embrittlement of samples in the absence of condensation.

In addition, liquid solutions of 35 wt. % H_2O_2 were also found not to be embrittling to 4340 high strength steel. However, increasing the concentrations of hydrogen peroxide vapor to levels of 1300 and 1600 ppm resulted in fracture of 2 of 2 samples tested under both of these conditions. The two samples exposed to 1300 ppm H_2O_2 failed after only 135 hrs and 180 hrs while loaded at 75% of the NFS. The two samples exposed to 1600 ppm H_2O_2 failed after only 100 hrs and 186 hrs while loaded at 75% of the NFS.

Significant condensation occurred throughout the test chamber during the 1300 and 1600 ppm H_2O_2 exposures. Condensation was noted all over the inside walls of the test chamber, the loading fixtures and the samples. The visible condensation persisted throughout the chamber for the entire duration of the 4.8 hr decontamination cycles. It should be noted that a small amount of condensation was seen in the process chamber during the first hour of the 4.8 hour decontamination cycle when exposing samples to 1000 ppm H_2O_2 vapor. This condensation evaporated after the first hour and was not seen during the remaining 3.8 hours of the exposure.

Chemical titration of the condensate sample following Huckaba and Keyes [94] indicated that the H_2O_2 concentration of the condensate from the 1600 ppm H_2O_2 treatment was 63.7% H_2O_2 , over twice the concentration of the original solution.

4.2.2 Fracture Behavior

The fracture surfaces of a number of samples were examined using scanning electron microscopy. Samples that survived both the H_2O_2 exposure and the 75% NFS load for 200 hrs are considered as not having become embrittled during the hydrogen peroxide exposure per ASTM Standard F519-06. The fracture surfaces of these samples exhibited evidence of failure by fine microvoid coalescence (i.e., ductile fracture) near the root of the notch as well as several millimeters away from the notch root. A typical fracture surface of such a sample is shown in Fig. 4.2 (a) and 4.2 (b) taken from close (~ 50μm from the notch root) to the notch and away (mid surface) from the notch respectively. Note the extensive fine microvoid coalescence. However, samples that did not survive the 75% NFS load for 200 hrs after H_2O_2 exposure exhibited evidence of brittle failure near the root of the notch as shown in Fig. 4.3 (a). Even though some of the fracture surface in the notch root zone exhibits fine microvoid coalescence, extensive evidence of brittle intergranular fracture is clearly seen throughout that region of the sample. The embrittled region in the high-stress notch root zone served to precipitate premature fracture even though evidence of failure primarily by ductile microvoid coalescence can be seen in Fig. 4.3 (b) several millimeters away from the notch root.

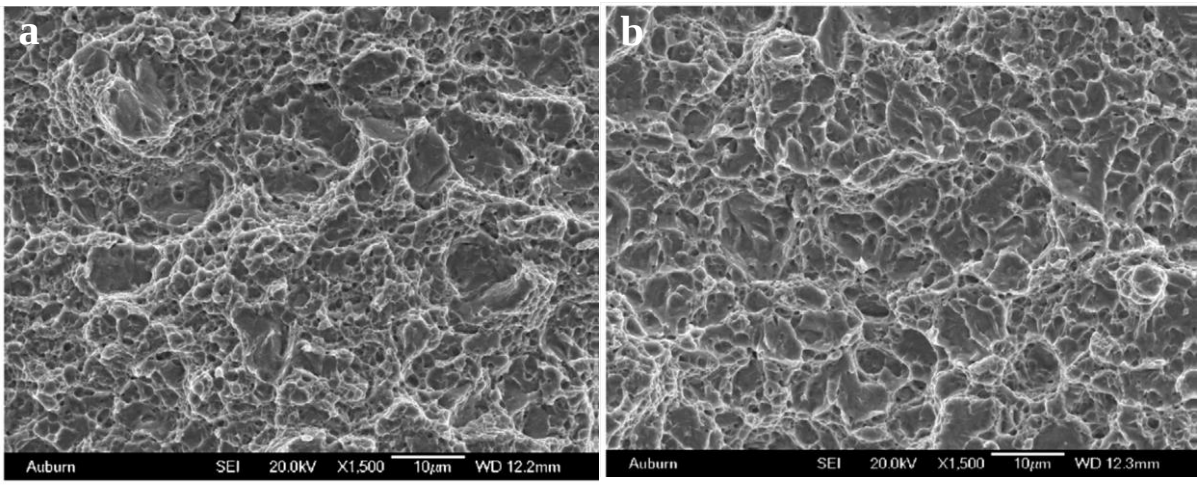

Fig. 4.5 Fracture surface of a non-embrittled sample exposed to 500ppm H2O2 for 4.8 h exhibiting ductile failure by microvoid coalescence. (a) Fracture surface near (with 150 μm) the notch root. (b) Fracture surface approximately 5mm away from the notch root

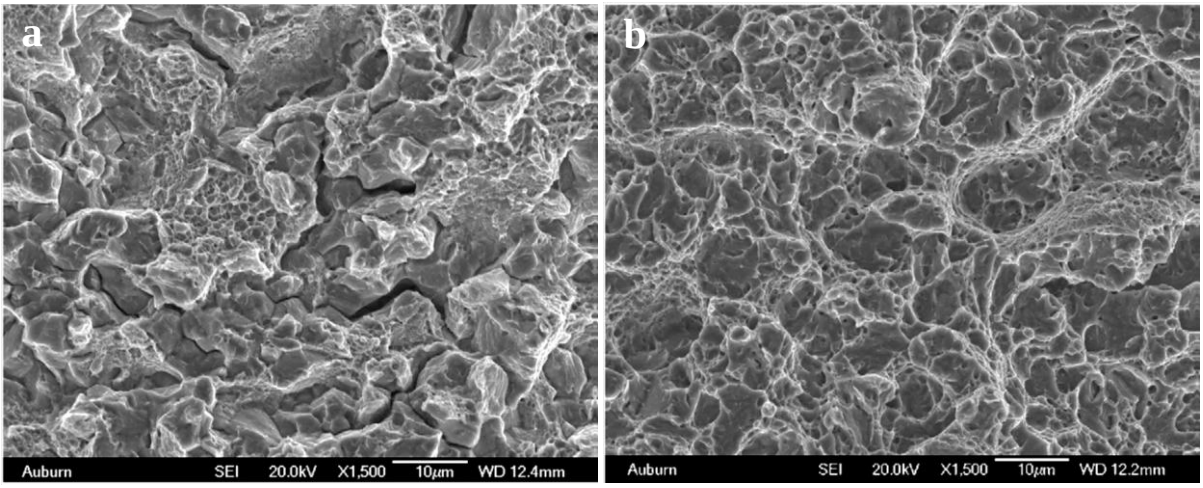

Fig. 4.6 Fracture surface of an embrittled sample exposed to 1600ppm H2O2 and condensed liquid (approximately 64 wt.% H2O2) for 4.8 h. (a) Fracture surface near the notch root exhibiting extensive intergranular fracture at the prior austenitic grain boundaries. (b) Fracture surface approximately 5mm away from the notch root exhibiting ductile failure by microvoid coalescence.

4.3 Electrochemical Hydrogenation

4.3.1 Effects of Charging Time

4.3.1.1 Mechanical Response

Fig. 4.4 shows the average failure strain at 0.01 mm/min cross head speed for the three PAGS investigated and various hardnesses as a function of different hydrogen charging times. The failure strain (ε_f) continually decreased with increasing hydrogen charging time. As expected, larger failure strains were observed with the softer samples compared to the harder samples.

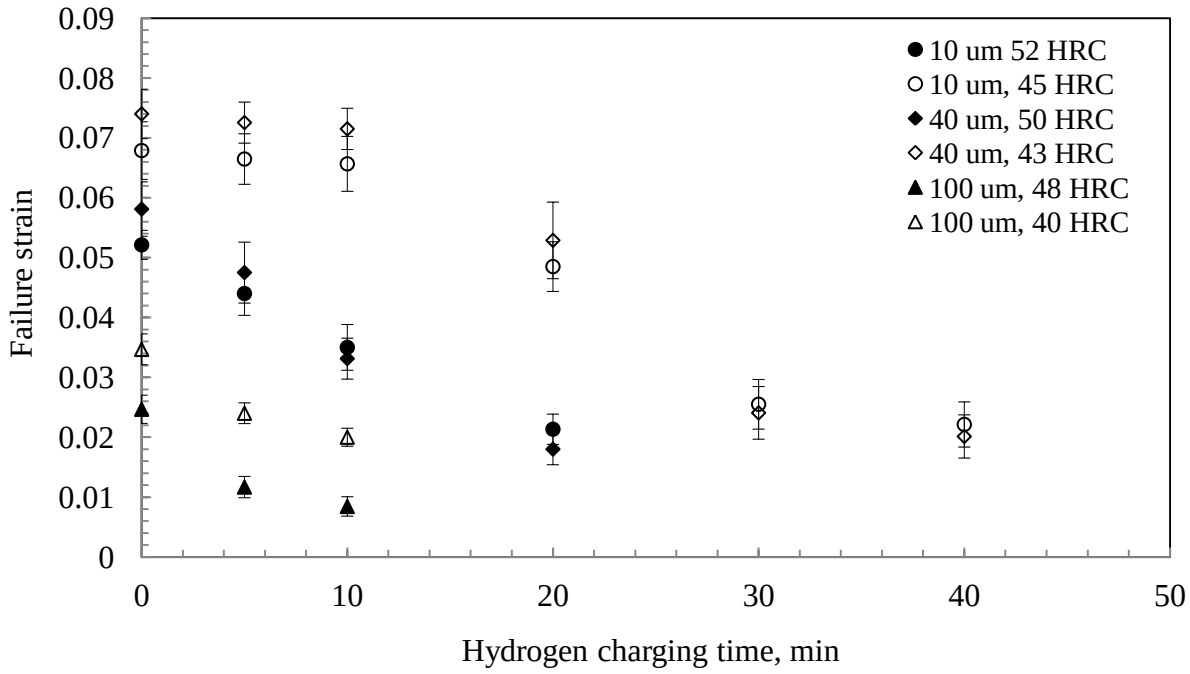

Fig 4.7. Change in failure strain as function of hydrogen charging time for the sample hardnesses and prior austenitic grain sizes (PAGS) shown. Tensile tests were performed using a cross head speed of 0.01 mm/min. The 100 μm PAGS samples were not charged for any times > 10 min. Error bars indicate the 2σ limit of data scatter.

No statistically significant (at 95% confidence level) differences in failure strain values were observed between the 10 and 40 μm PAGS samples. This result agrees with the finding of Lessar and Gerbarich [15] who did not observe any significant difference in fracture behavior of hydrogenated samples up to the prior austenitic grain size range of ~ 40μm However, increasing the PAGS to 100 μm resulted in a significant decrease of ε_f for both levels of hardness investigated here. Representative tensile results are provided in appendix B.

4.3.1.2 Fracture Behavior

Fig. 4.8 shows representative fracture behavior from close to the notch (i.e. ~ 100 μm depth) and sample centerline (i.e. ~ 2000 μm depth) for the harder (50-52 HRC) uncharged samples with 10μm and 40 μm PAGS. Samples were loaded at a cross-head speed of 0.01 mm/min (strain rate : 8.55×10^{-6} s^{-1}). Extensive microvoid coalescence is seen close to the notch (up to a depth of ~ 750 μm). However, from that depth to the sample centerline, the fracture surface of the harder samples exhibited a mixture of dimples and "flat" features. Fig. 4.9. shows representative fracture behavior close to the notch (i.e. ~ 100 μm depth) and sample centerline (i.e. ~ 2000 μm depth) for uncharged 10μm and 40 μm PAGS, softer (43-45 HRC) samples. The uncharged softer samples for both grain sizes showed a fracture surface composed of dimples representative of microvoid coalescence at all distances from the notch.

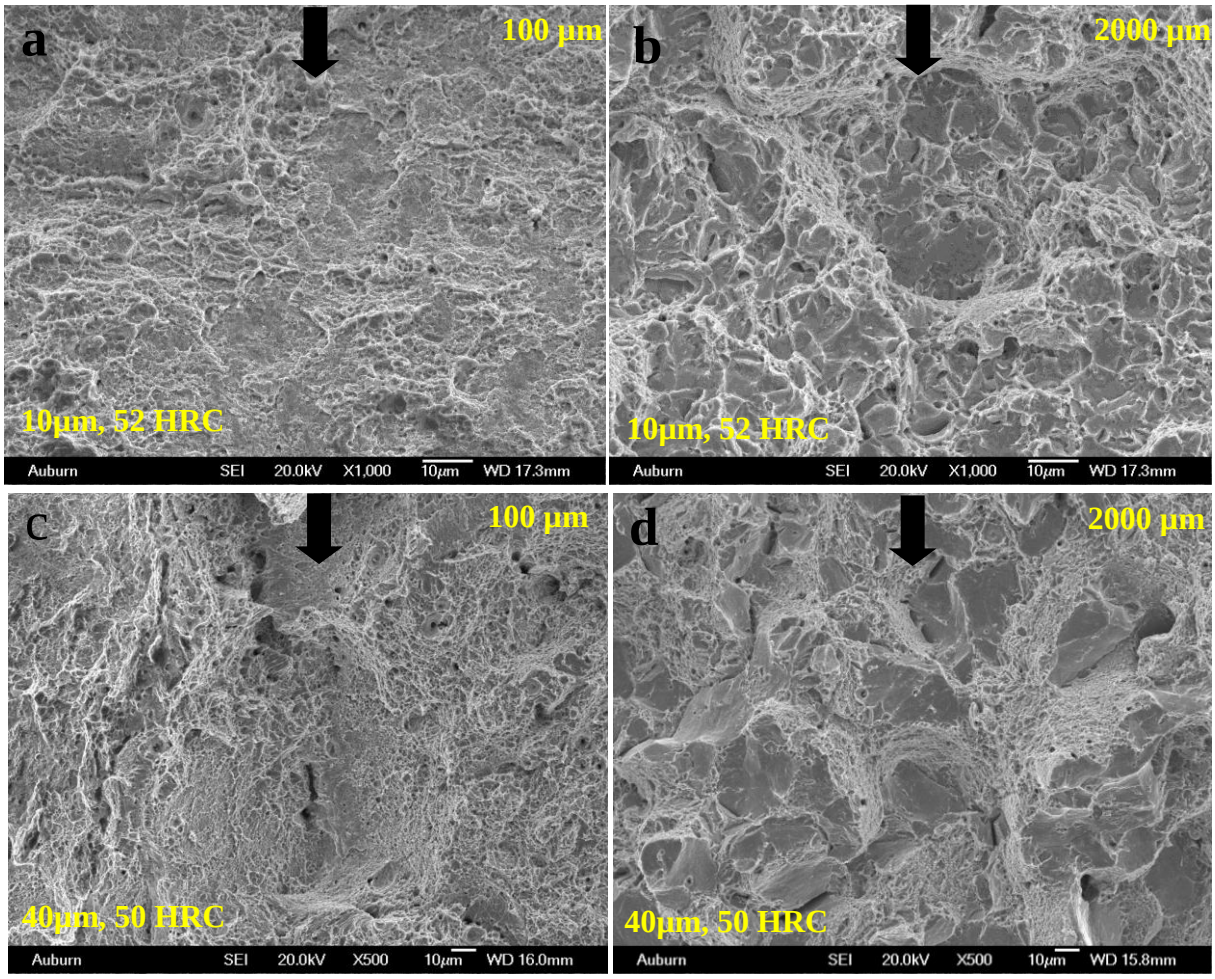

Fig 4.8. Fracture characteristics for uncharged 10 and 40 µm PAGS harder samples: (a) and (c) ~ 100 µm from the notch, (b) and (d) ~ 2000 µm away µm from the notch. PAGS and hardnesses are shown in the respective images. Arrows indicate the crack growth direction. Cross-head speed used: 0.01mm/min

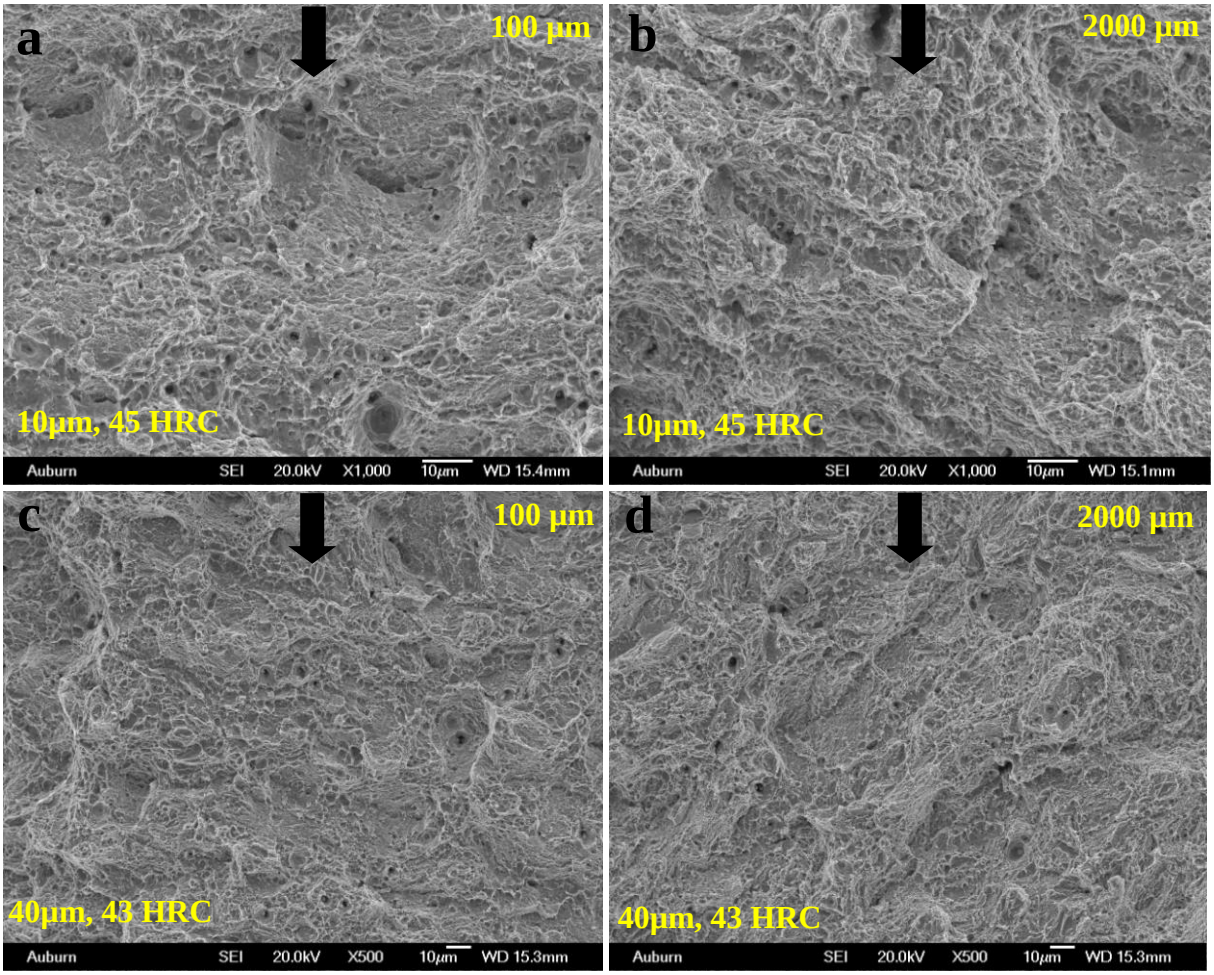

Fig 4.9. Fracture characteristics for uncharged 10 and 40 µm PAGS softer samples: (a) and (c) ~ 100 µm from the notch, (b) and (d) ~ 2000 µm away µm from the notch. PAGS and hardnesses are shown in the respective images. Arrows indicate the crack growth direction. Cross-head speed used: 0.01mm/min

Fig. 4.10 shows representative fracture behavior from close to the notch and sample centerline for the harder (50-52 HRC) 10 min charged samples with 10µm and 40 µm PAGS. Samples were loaded at a cross-head speed of 0.01mm/min (strain rate : 2.85×10^{-6} s^{-1}). A mixture of intergranular fracture and microvoid coalescence was exhibited close to the notch (up to a depth of ~ 500-600 µm) as a result of hydrogen incorporation. From 600µm from the notch to the sample centerline, the fracture surface exhibited a mixture of dimples and "flat" features. Fig. 4.11 shows representative fracture behavior close to the notch and sample centerline for 10 min charged 10µm and 40 µm PAGS, softer (43-45 HRC) samples. The uncharged softer samples for both grain sizes showed similar fractographic behavior as their uncharged counterpart indicating no significant effect of hydrogen at that charging exposure time.

However, the softer 20 min charged 10µm and 40 µm PAGS, softer (43-45 HRC) samples showed some brittle transcrystalline quasi-cleavage in the region only up to 100 - 200 µm from the notch. See Fig. 4.12. The 10µm samples apparently have more smooth facets and secondary cracks compared to 40 µm samples. However, no apparent intergranular fracture was observed for the 20 min charged softer samples. Representative images are taken from ~100 and ~2000 µm away from the ground notch.

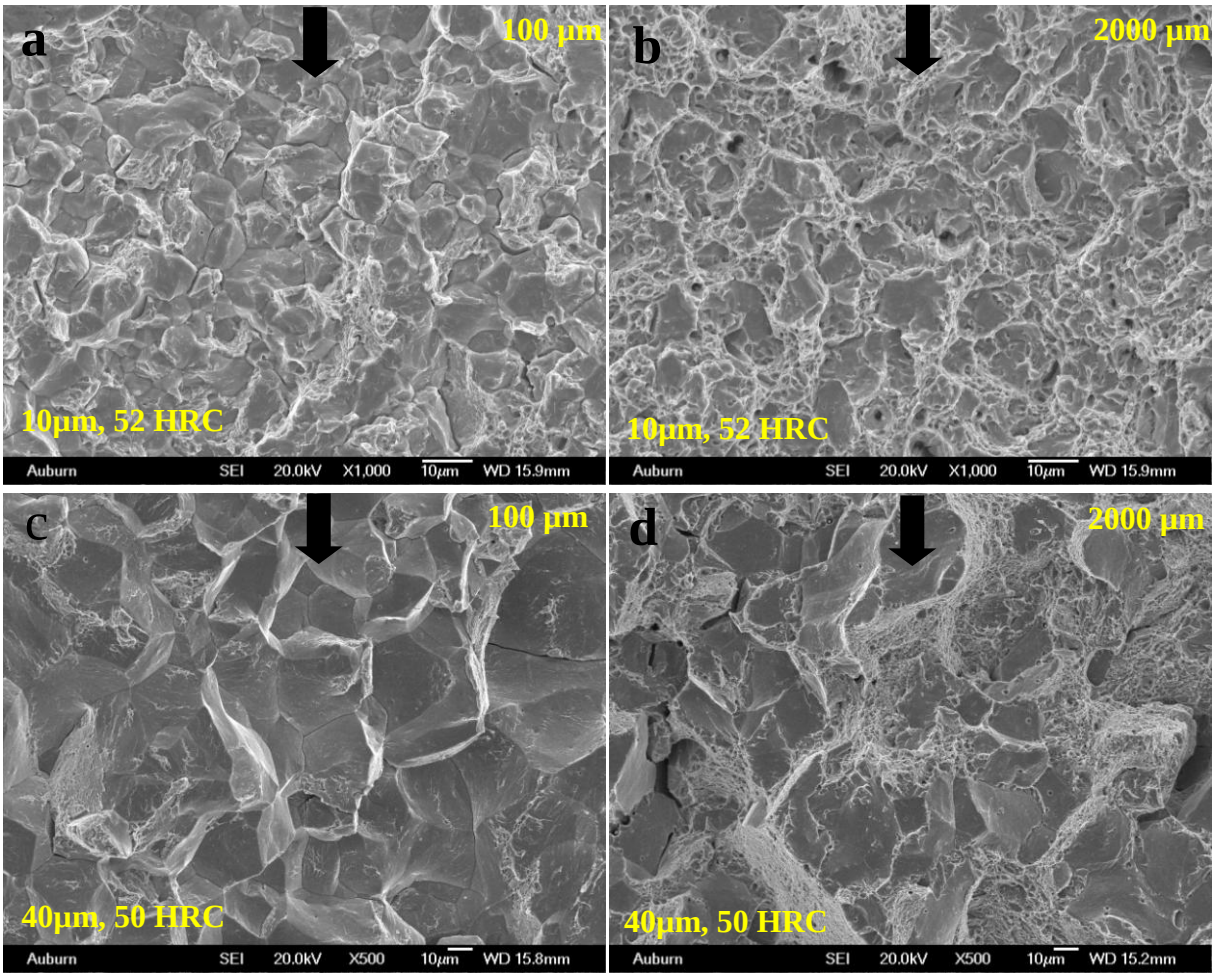

Fig 4.10. Fracture characteristics for 10 min hydrogen charged 10 and 40 µm PAGS harder samples: (a) and (c) ~ 100 µm from the notch, (b) and (d) ~ 2000 µm away µm from the notch. PAGS and hardnesses are shown in the respective images. Arrows indicate the crack growth direction. Cross-head speed used: 0.01mm/min.

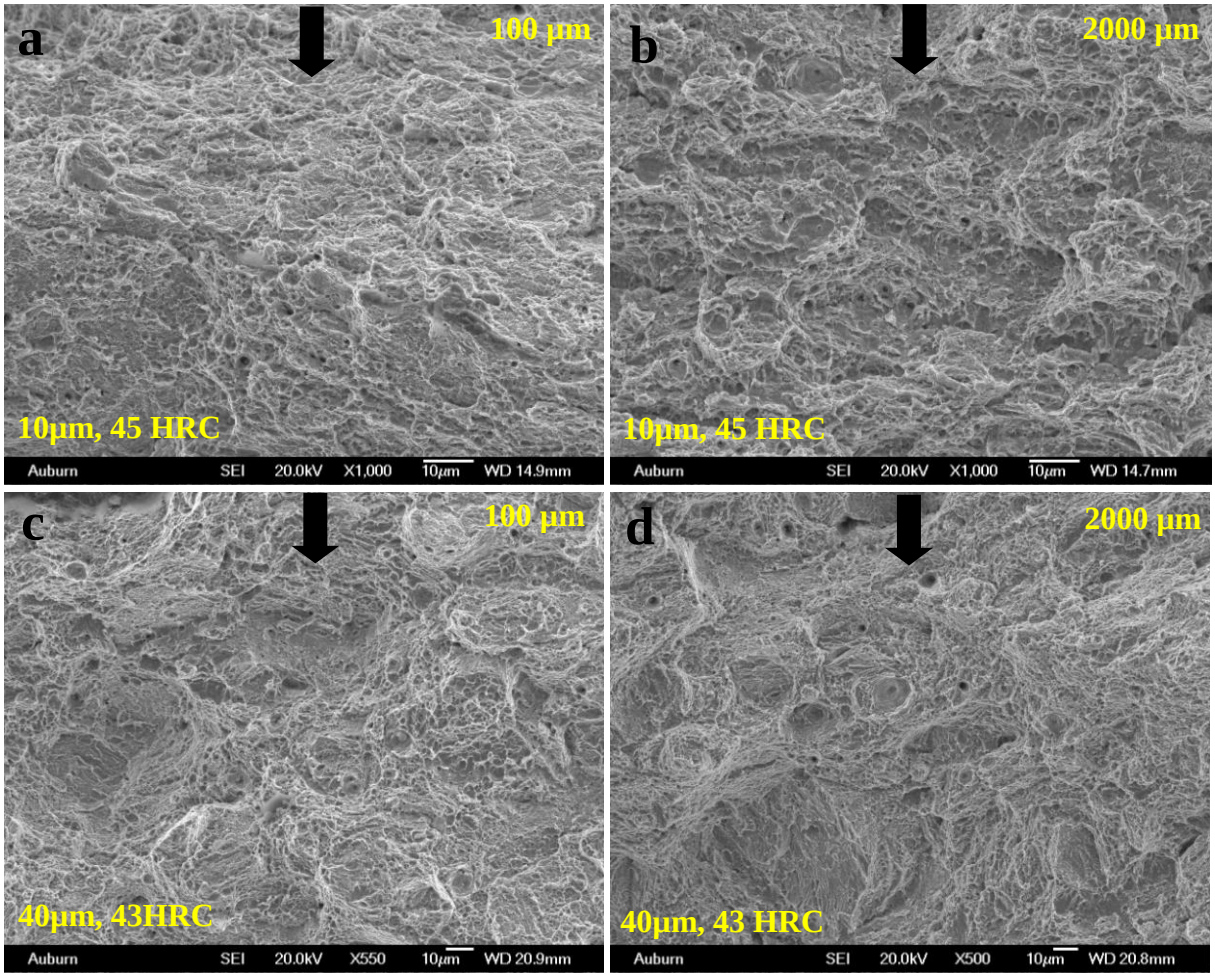

Fig 4.11. Fracture characteristics for 10 min hydrogen charged 10 and 40 µm PAGS softer samples: (a) and (c) ~ 100 µm from the notch, (b) and (d) ~ 2000 µm away µm from the notch. PAGS and hardnesses are shown in the respective images. Arrows indicate the crack growth direction. Cross-head speed used: 0.01mm/min.

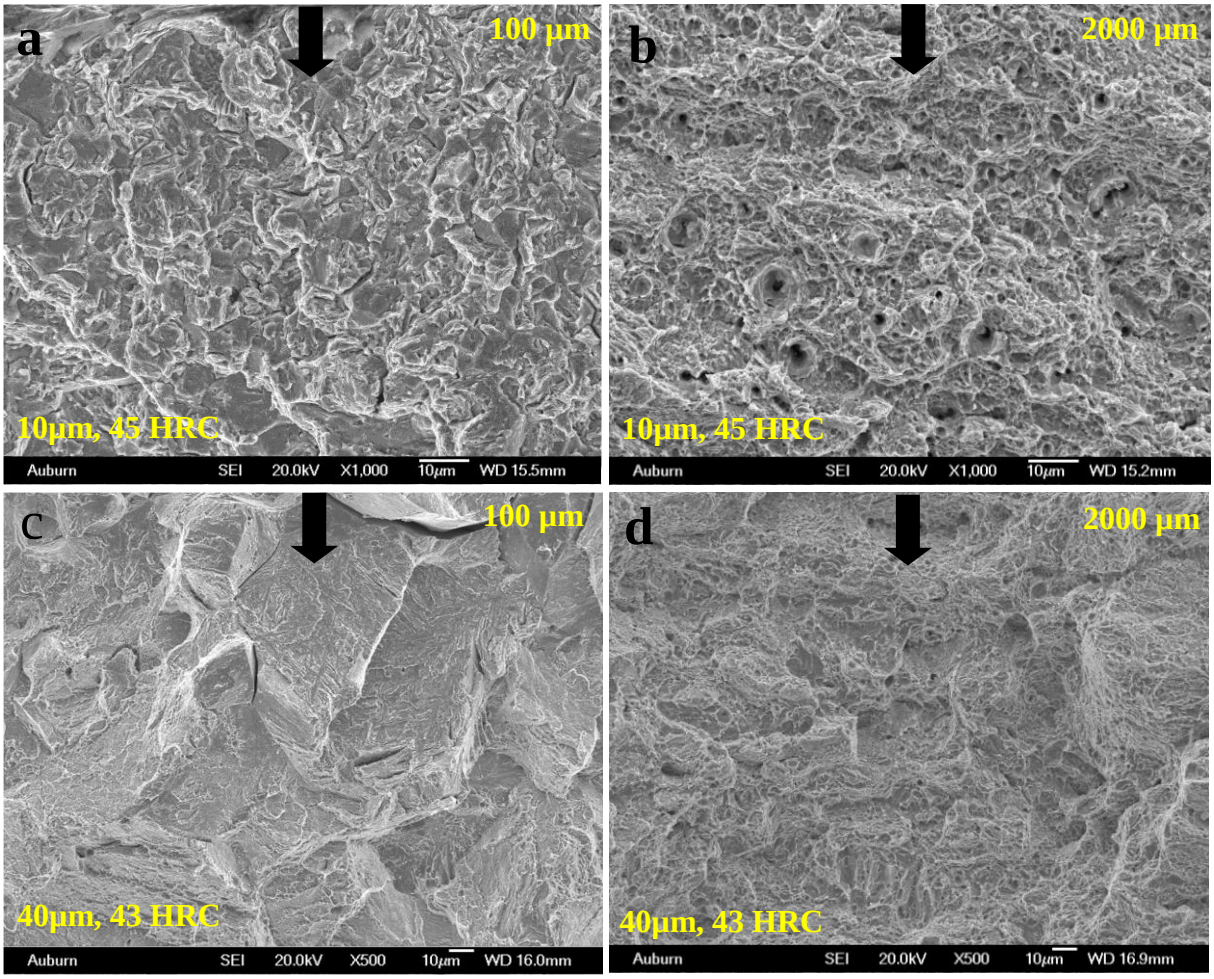

Fig 4.12. Fracture characteristics for 20 min hydrogen charged 10 and 40 µm PAGS softer samples: (a) and (c) ~ 100 µm from the notch, (b) and (d) ~ 2000 µm away µm from the notch. PAGS and hardnesses are shown in the respective images. Arrows indicate the crack growth direction. Cross-head speed used: 0.01mm/min.

The 10 μm and 40 μm PAGS harder (50-52 HRC) samples exhibited a greater degree of intergranular fracture after 20 min charging when compared to 5 min and 10 min charging as expected. Samples were loaded at a cross-head speed of 0.01 mm/min (strain rate : 8.55×10^{-6} s^{-1}). The fracture behavior as a function of distance from the notch to the sample centerline for harder samples hydrogenated for 20 min is shown in Fig. 4.13 (10μm PAGS, 52 HRC) and Fig. 4.14 (40 μm PAGS, 50 HRC). Representative images were taken from 100μm, 500μm, 1000μm and 2000 μm away from the ground notch to show trend of fracture behavior as the distances increase. The fracture surfaces up to 1000 μm depth were dominated by intergranular fracture along with some secondary cracking as well as evidence of dimples. The fracture surface from about 1000 μm depth to the sample centerline exhibited a mixed appearance of flat, cleavage-like features along with dimples. Although some of the flat features exhibited river patterns typical of classical cleavage fracture, the majority of the flat features did not.

Fig. 4.15 and Fig 4.16 show representative fracture behavior from close to the notch towards the sample centerline for softer samples hydrogenated for 40 min: 10μm PAGS (43 HRC) and 40 μm PAGS (45 HRC), respectively. Samples were loaded at a cross-head speed of 0.01 mm/min (strain rate : 8.55×10^{-6} s^{-1}). Representative images were taken from 100μm, 500μm, 1000μm and 2000 μm away from the ground notch to shown trend of fracture behavior as the distances increase. Fracture surfaces are dominated by dimples at large distances from the notch for both samples (2000μm , Fig. 4.15 and 4.16) while a quasi-cleavage fracture mode mixed with some evidence for intergranular fracture is seen in the high stress region closer to the notch. A number of secondary cracks are also evident in the vicinity of the notch.

The quasi-cleavage fracture features seen in this investigation are similar to those reported by Martin et al.[10], Nagao et al.[11] and Lynch[49]. Martin et al. [10] asserted that

quasi-cleavage can result from the growth and coalescence of microvoids that initiate and grow within intense slip band intersections. Lynch [49] argued that quasi-cleavage occurs across martensitic laths and/or along the martensitic lath boundaries. In this work, quasi-cleavage associated with the 40 μm size predominantly showed surfaces decorated with lath-like features and fine tear ridges, consistent with the interpretation of Lynch. According to Lynch [49], the smooth, featureless facets (“flats”) are the result of fracture paths along martensitic lath boundaries. The fracture surfaces of the 10 μm grain size samples in the present work predominantly exhibited smooth facets without significant evidence for trans-lath fracture paths.

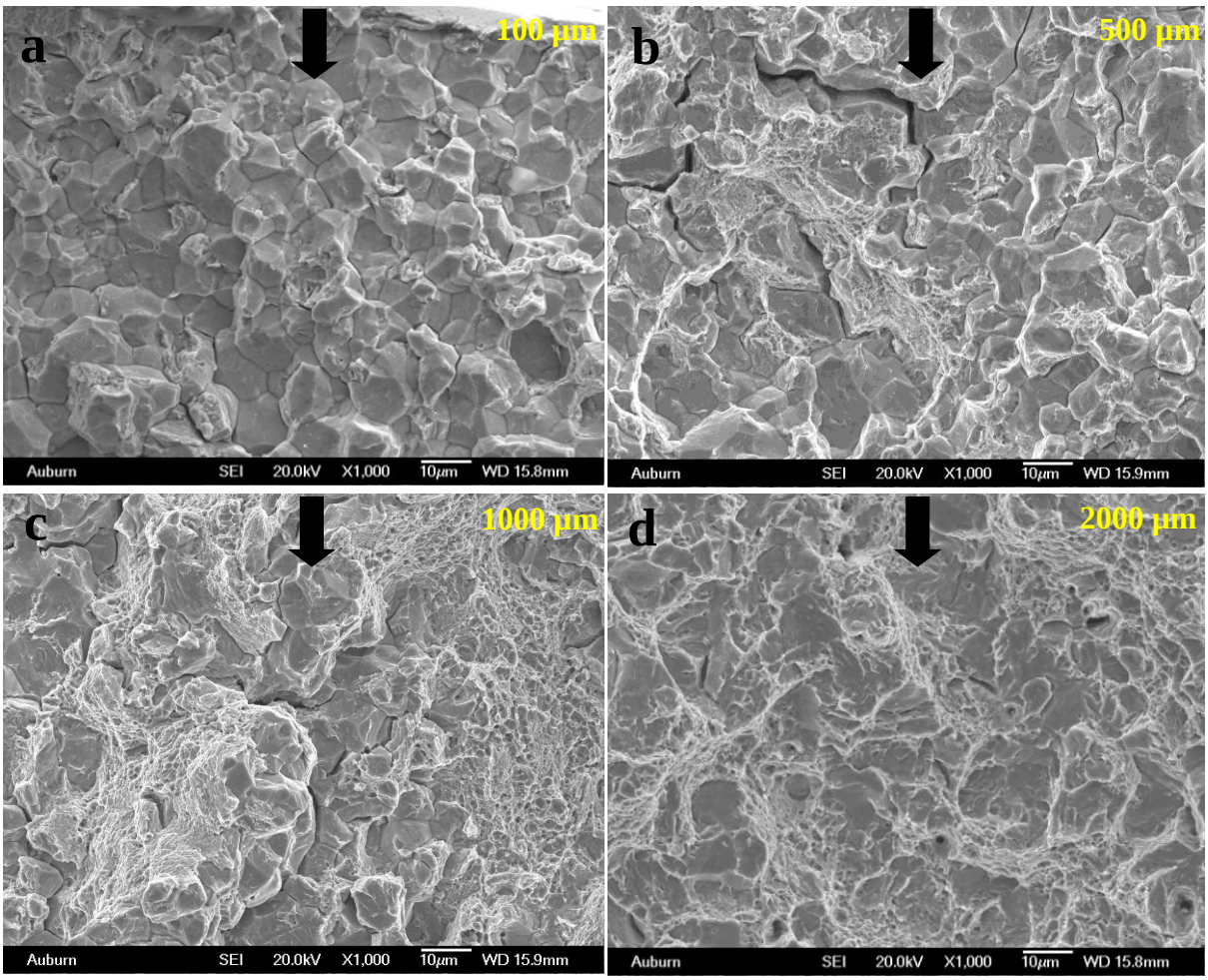

Fig 4.13. Fracture characteristics with increasing distance from the notch for 20 min hydrogenated 10µm PAGS, 52 HRC samples. Pictures taken from (a) 100µm, (b) 500 µm, (c) 1000µm and (d) 2000µm away from the notch. Arrows indicate the crack growth direction. Cross-head speed used: 0.01mm/min

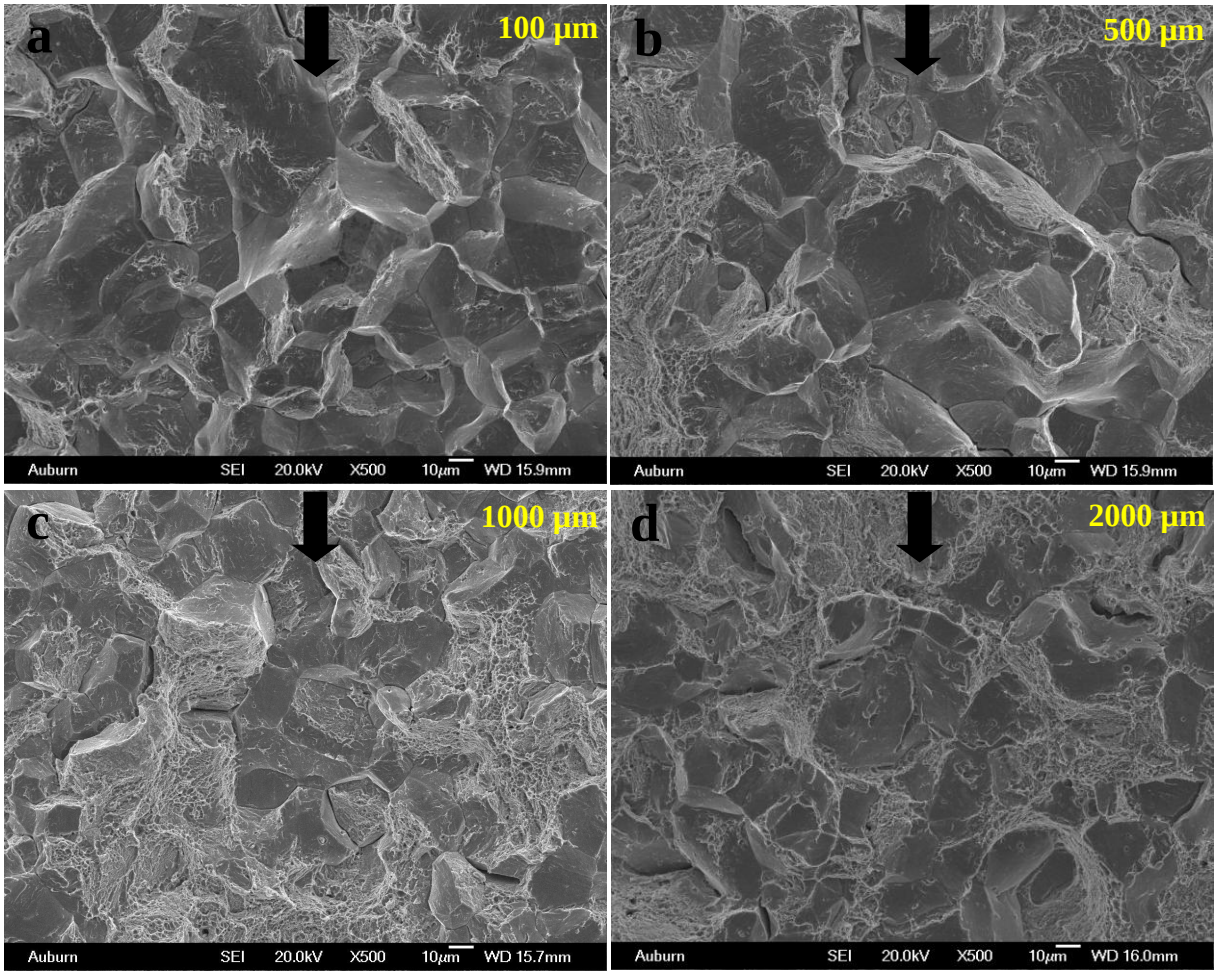

Fig 4.14. Fracture characteristics with increasing distance from the notch for 20 min hydrogenated 40µm PAGS, 50 HRC samples. Pictures taken from (a) 100µm, (b) 500 µm, (c) 1000µm and (d) 2000µm away from the notch. Arrows indicate the crack growth direction. Cross-head speed used: 0.01mm/min

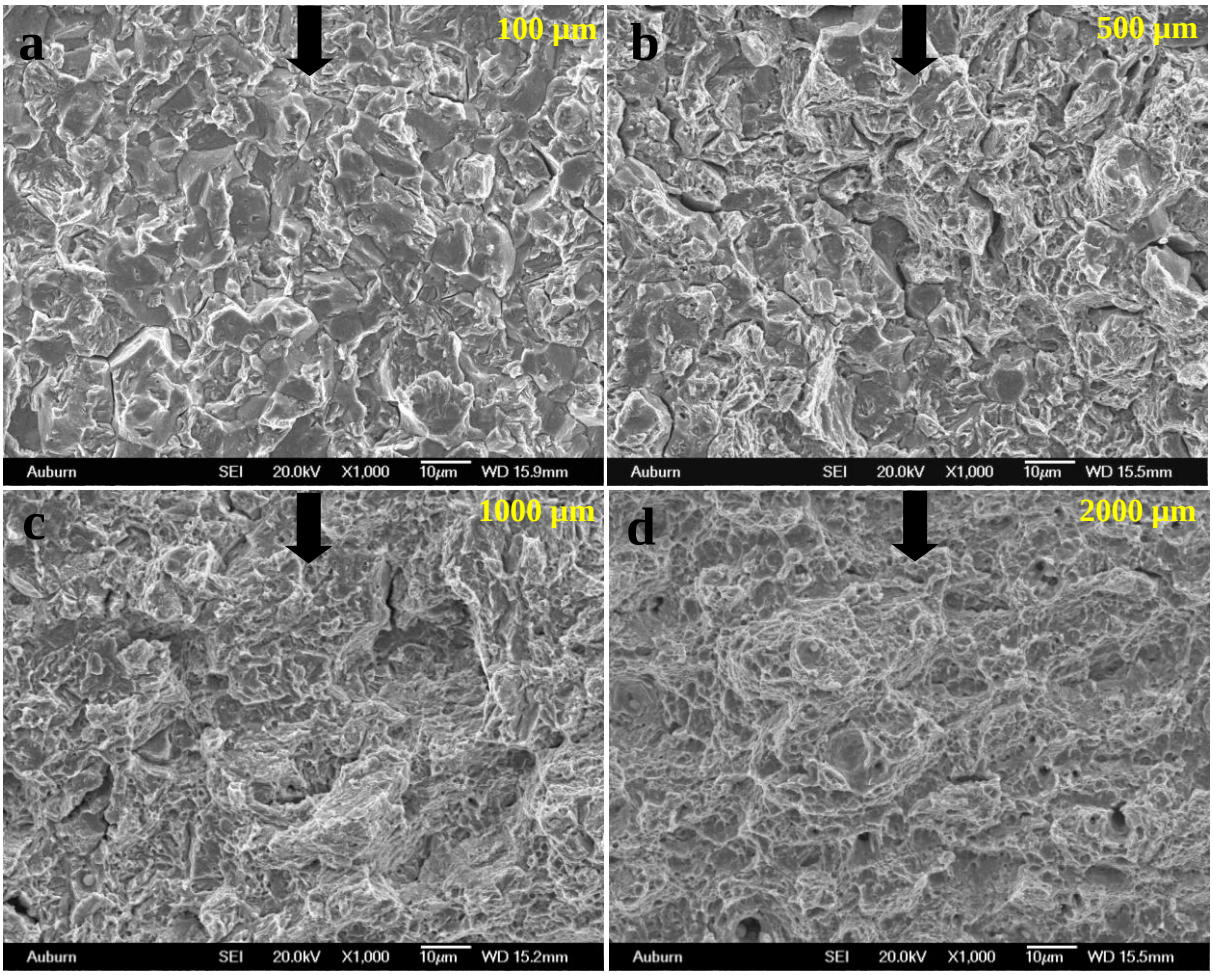

Fig 4.15. Fracture characteristics with increasing distance from the notch for 40 min hydrogenated 10µm PAGS, 45 HRC samples. Pictures taken from (a) 100µm, (b) 500 µm, (c) 1000µm and (d) 2000µm away from the notch. Arrows indicate the crack growth direction. Cross-head speed used: 0.01mm/min

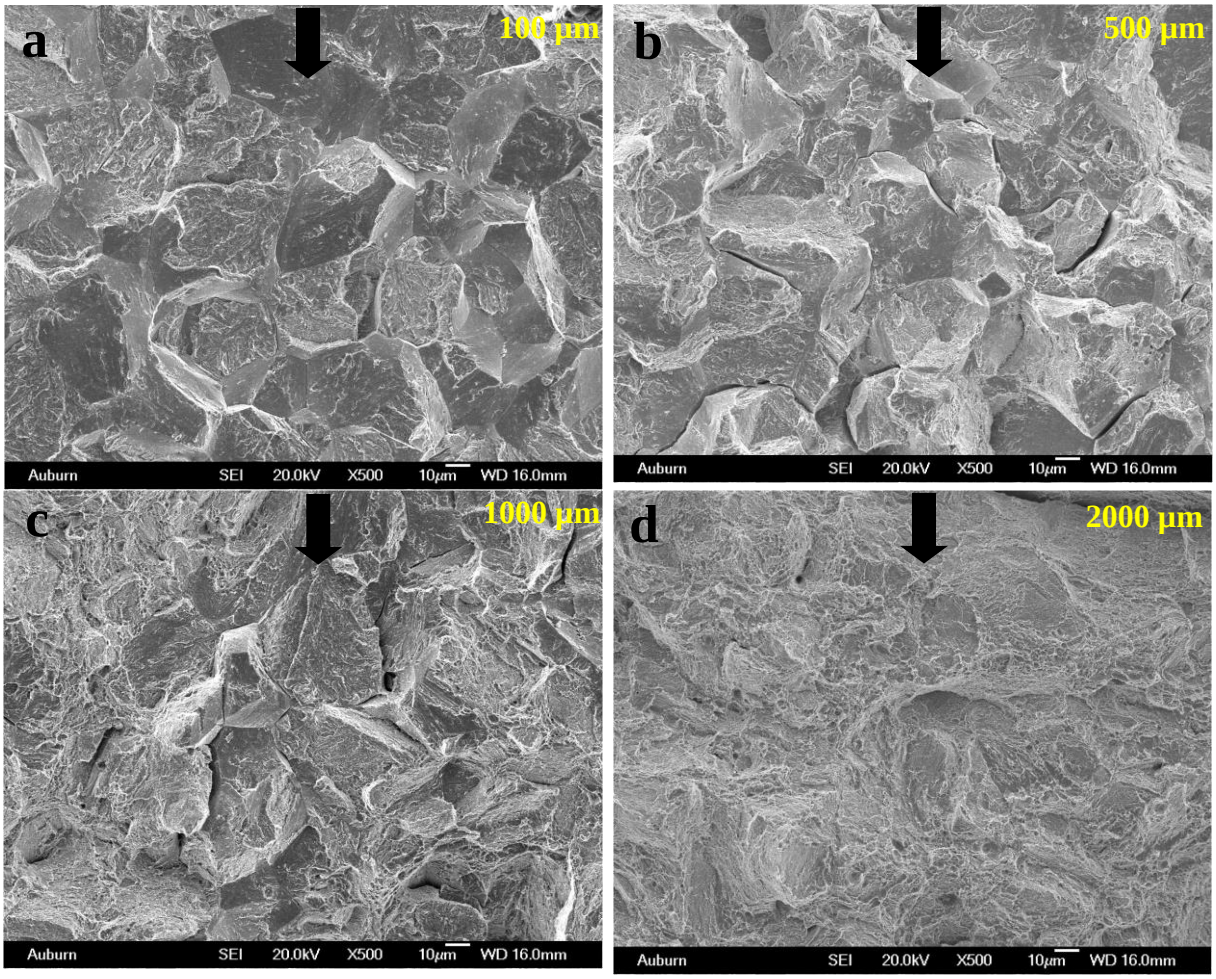

Fig 4.16. Fracture characteristics with increasing distance from the notch for 40 min hydrogenated 40µm PAGS, 43 HRC samples. Pictures taken from (a) 100µm, (b) 500 µm, (c) 1000µm and (d) 2000µm away from the notch. Arrows indicate the crack growth direction. Cross-head speed used: 0.01mm/min

The fracture behavior of large grain (~ 100 μm) samples was in agreement with their lower fracture strain. 100 μm PAGS large harder (~48 HRC) samples showed intergranular fracture along with relatively lower (< 15%) amount of quasi cleavage even without any hydrogen charging. Unlike the large PAGS harder samples, large PAGS softer (~41 HRC) did not show intergranular fracture. The large PAGS softer samples showed quasi-cleavage even in the absence of hydrogen charging. Hydrogen charging these samples even for short periods (e.g. 5-10 min) caused more extensive intergranular (harder sample) and quasi-cleavage (softer sample) fracture close to the notch.

The inferior mechanical property and evidence of intergranular and quasi-cleavage fracture for the large PAGS sample even without hydrogen charging is presumably due to bigger size of the martensitic lath packets associated to the grains as observed by Morito et al. in Fe – 0.2 wt% C – 2 wt% Mn alloy [85]. However, the predominant intergranular failure in case of harder samples is apparently due to the temper martensitic embrittlement favorable at the tempering temperature associated to it. It is mentioned in the earlier section that this tempered martensitic embrittlement could be due to the singular or combined effects of impurity (P, S, N, Sn, Sb) segregation and/or post tempering (>150^{o}C) carbide. Because of the larger grain size the density of the segregating alloying elements and/or carbide particle at the grain boundary is significantly high to result embrittlement though intergranular fracture even in absence of hydrogen. However, in case of the softer sample even though the grain size is similar to that of the sample the effect of temper embrittlement is not present due to its associated tempering temperature which falls beyond the margin of temper martensitic embrittlement. The inferior mechanical property (relatively better than similar grain size harder sample) in case of the large softer samples is presumably merely due to the bigger martensitic lath packets.

Fig. 4.17 shows representative fracture behavior from close to the notch (i.e ~100 µm depth) and sample centerline (i.e. ~ 2000 µm) for the 100µm PAGS harder (48 HRC) uncharged and 10 min charged samples. Uncharged sample within ~150 µm distance from the notch showed predominant dimple mode with relatively less intergranular mode with a small fraction of quasi cleavage. However, after this region up to the central line it showed predominant intergranular fracture mixed with small percent of dimples and quasi-cleavage. On the other hand 10 min hydrogenated 100 µm PAGS harder samples showed predominant intergranular fracture mixed with small percent of microvoid and quasi cleavage at all distances from the notch.

Representative fracture behavior for the softer (41 HRC) 100µm PAGS uncharged and 10 min charged sample from close to the notch (i.e ~100 µm depth) and sample centerline (i.e. ~ 2000 µm) are shown in Fig. 4.18. 100 µm PAGS softer uncharged sample within ~150 µm distance from the notch showed predominant dimple mode with relatively less quasi-cleavage. After ~ 150 µm from the notch up to the central line it showed mixture quasi-cleavage and dimples. After 10 min hydrogenation 100 µm PAGS softer showed predominant quasi-cleavage close to the notch and mixture of almost equal percent of microvoid and quasi cleavage away from the notch.

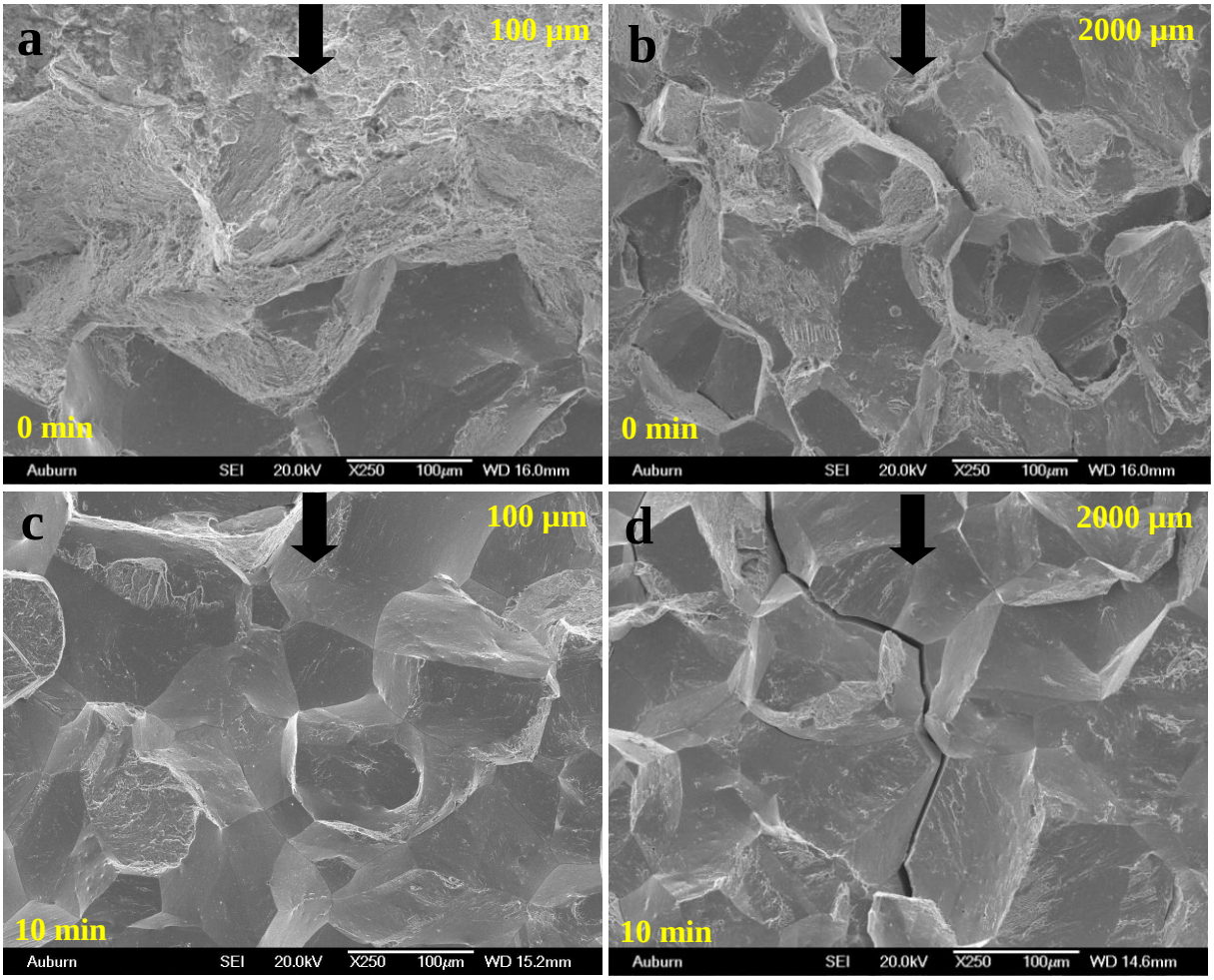

Fig. 4.17. Fracture characteristics for 0 and 10 min hydrogen charged 100 µm PAGS harder (48HRC) samples. Charging times are shown in the respective images : (a) and (c) ~ 100 µm from the notch, (b) and (d) ~ 2000 µm away µm from the notch. Arrows indicate the crack growth direction. Cross-head speed used: 0.01mm/min

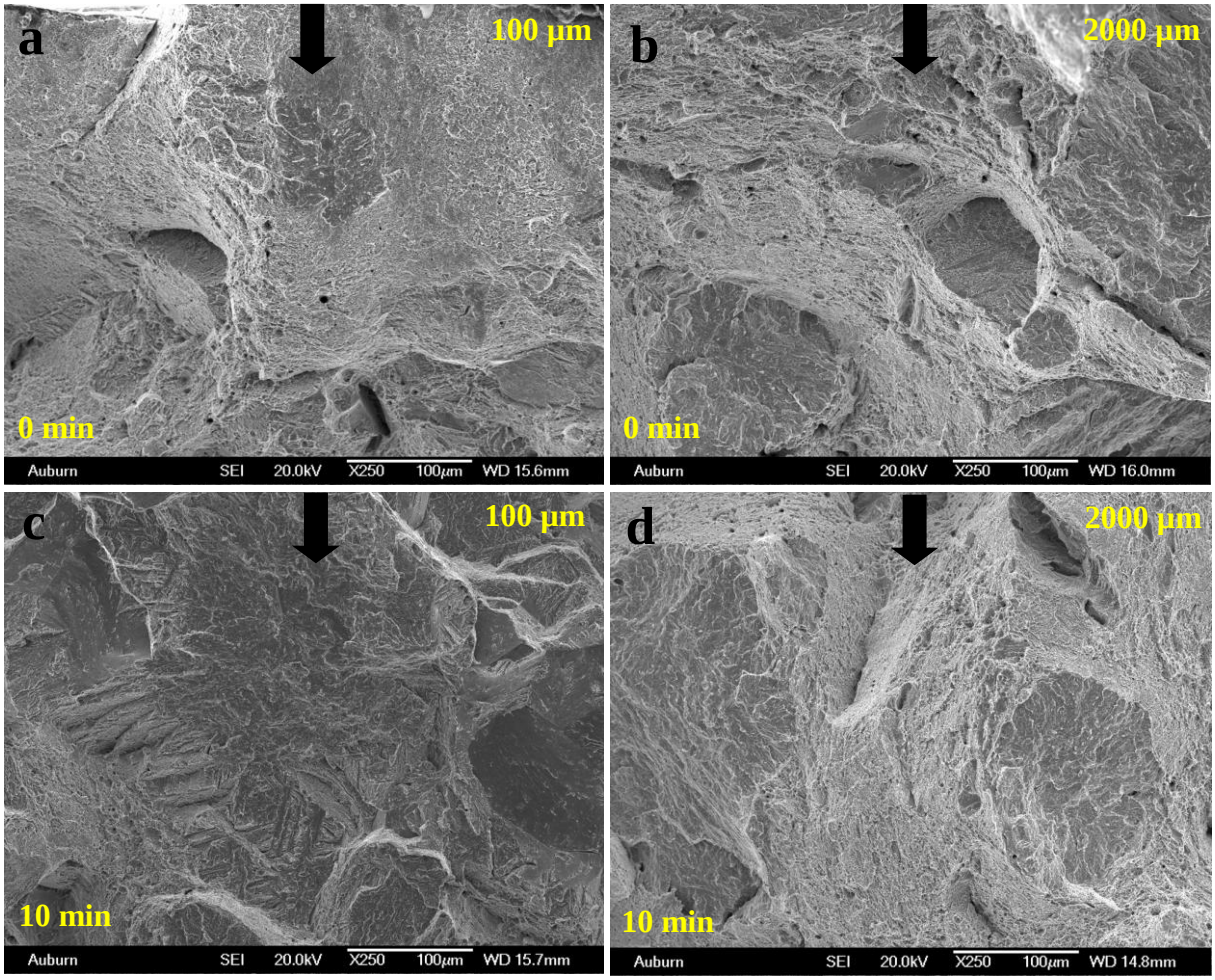

Fig. 4.18. Fracture characteristics for 0 and 10 min hydrogen charged 100 µm PAGS softer (41HRC) samples. Charging times are shown in the respective images : (a) and (c) ~ 100 µm from the notch, (b) and (d) ~ 2000 µm away µm from the notch. Arrows indicate the crack growth direction. Cross-head speed used: 0.01mm/min.

The quantitative variation of percentage intergranular fracture, percentage dimpled surface and percentage flat surfaces (featureless and smooth) with increasing distance from the notch were quantified by scanning electron microscopy for the range of experimental conditions investigated and the results are shown in Figs. 4.14- 4.16. Samples were loaded at a cross-head speed of 0.01 mm/min (strain rate : 8.55×10^{-6} s^{-1}).

Fig 4.19(a) and 4.19(b) present the quantitative variation of percent intergranular fracture and flat surfaces with increasing distance from the notch for the 10 µm 52 HRC samples hydrogen charged for 0, 5, 10 and 20 min while Fig 4.19(c) and 4.19(d) present similar results for the 40 µm, 50 HRC samples. The unhydrogenated samples did not show any evidence of intergranular failure while increasing the hydrogenation times showed an increasing level of intergranular failure which was observed to be most intense closer to the notch. For 10-40 µm 50-52 HRC samples, the rate of average decrease in percent intergranular fracture with increasing distance from the notch for 5 min charged samples was approximately 3 times greater than that for 20 min charged samples.

Fig 4.20(a) and 4.20(b) present the quantitative variation of percent intergranular fracture and quasi-cleavage with increasing distance from the notch for the 10 µm, 45 HRC samples hydrogen charged for 0, 20, 30 and 40 min while Fig 4.20(c) and 4.20(d) present similar results for the 40 µm, 43 HRC samples. The softer samples did not show any evidence of intergranular failure until after 30 min of hydrogen charging and then only in the vicinity of the notch. Evidence for quasi-cleavage fracture close to the notch was noted after 20 min of hydrogen charging. Increasing the hydrogen charging time above 20 min induced more evidence of both intergranular fracture and quasi-cleavage. However, quasi-cleavage was predominant. The intensity and depth of both these fracture modes away from the notch was generally observed to

increase with increasing charging time. The softer samples, unlike their harder counterparts, did not exhibit any featureless flat surfaces away from the notch and rather showed fracture involving primarily microvoid coalescence.

The maximum percent intergranular fracture close to the notch was presumably the result of stress induced diffusion of hydrogen [96] which would increase the hydrogen concentration close to the notch where the triaxial stresses are a maximum. In addition, the observed similarity in mechanical and fracture behavior for the 10 and 40 μm PAGS samples indicates independency of grain size within this PAGS range, in agreement with the results of Lessar and Gerbarich [15]

Fig. 4.21 (a) and 4.21 (b) provide the full fractographic characterization of fracture mode for 20 min of hydrogen charging for 10μm and 40μm harder samples. Fig. 4.21 (c) and 4.21 (d) show the same for 40 min of hydrogen charging for 10μm and 40μm softer samples The harder samples exhibited intergranular fracture at much lower hydrogen charging times compared to the softer samples due to the commonly observed tempered martensitic embrittlement in commercial low alloy, high strength steel after tempering in the temperature range of 250-350^{o}C [16]. Samples tempered in this temperature range typically show grain boundary embrittlement due to the singular or combined effects of impurity (P, S, N, Sn, Sb) segregation and/or post tempering (>150^{o}C) carbide formation. However, the tempering temperature used for the softer samples in this work (500^{o}C) was too high to cause tempered martensitic embrittlement. Thus the loss of ductility observed for these samples was solely caused by hydrogen effects.

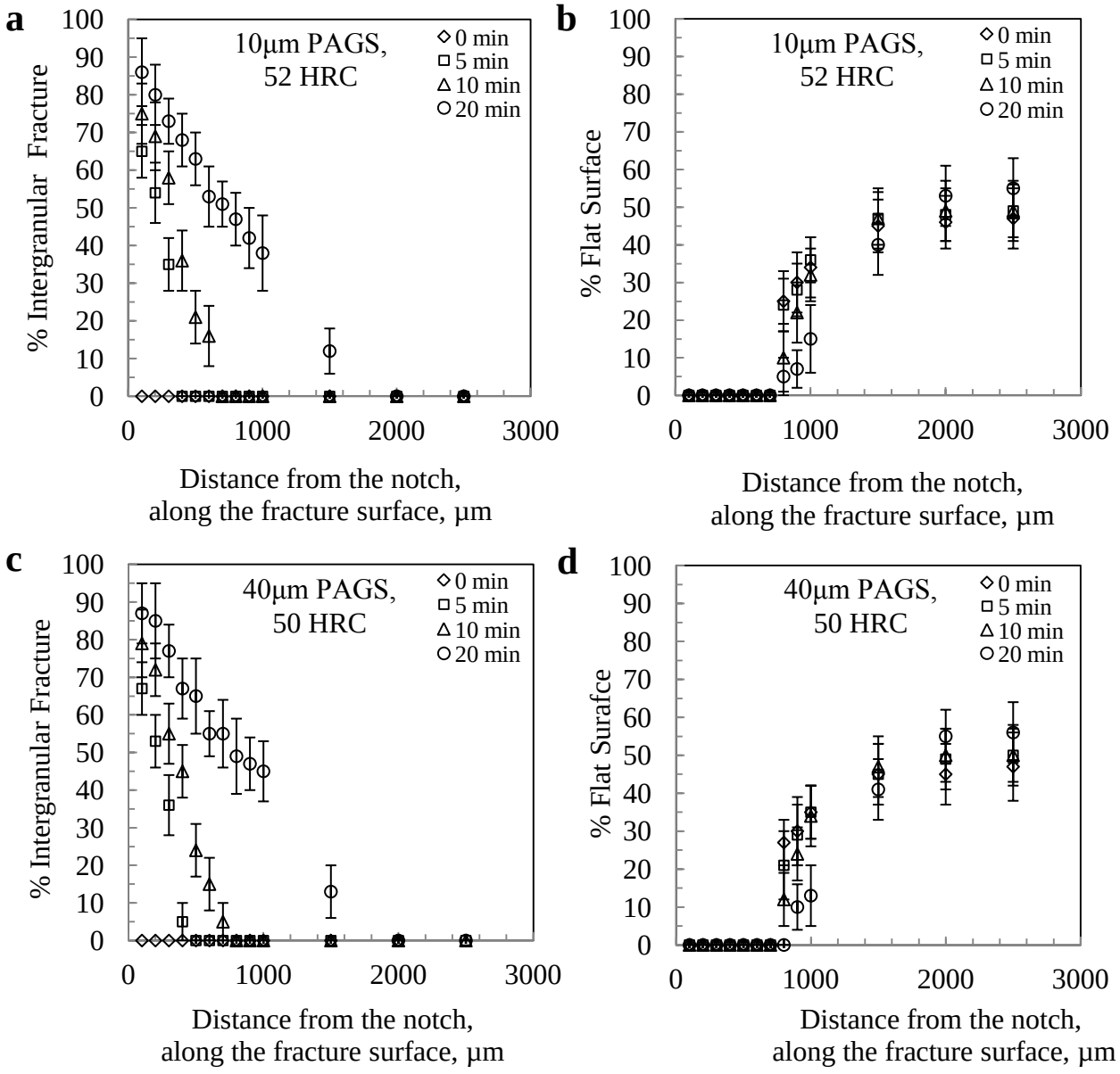

Fig 4.19. Quantitative variation of percent fracture modes with increasing distance from the notch for harder samples for 0, 5,10 and 20 min hydrogen charging: PAGS and hardnesses are shown in the respective pictures (a) and (c) intergranular, (b) and (d) flat surfaces. Each data point represents average of 4 samples. Error bars represent 2σ scatter. Cross-head speed used : 0.01mm/min

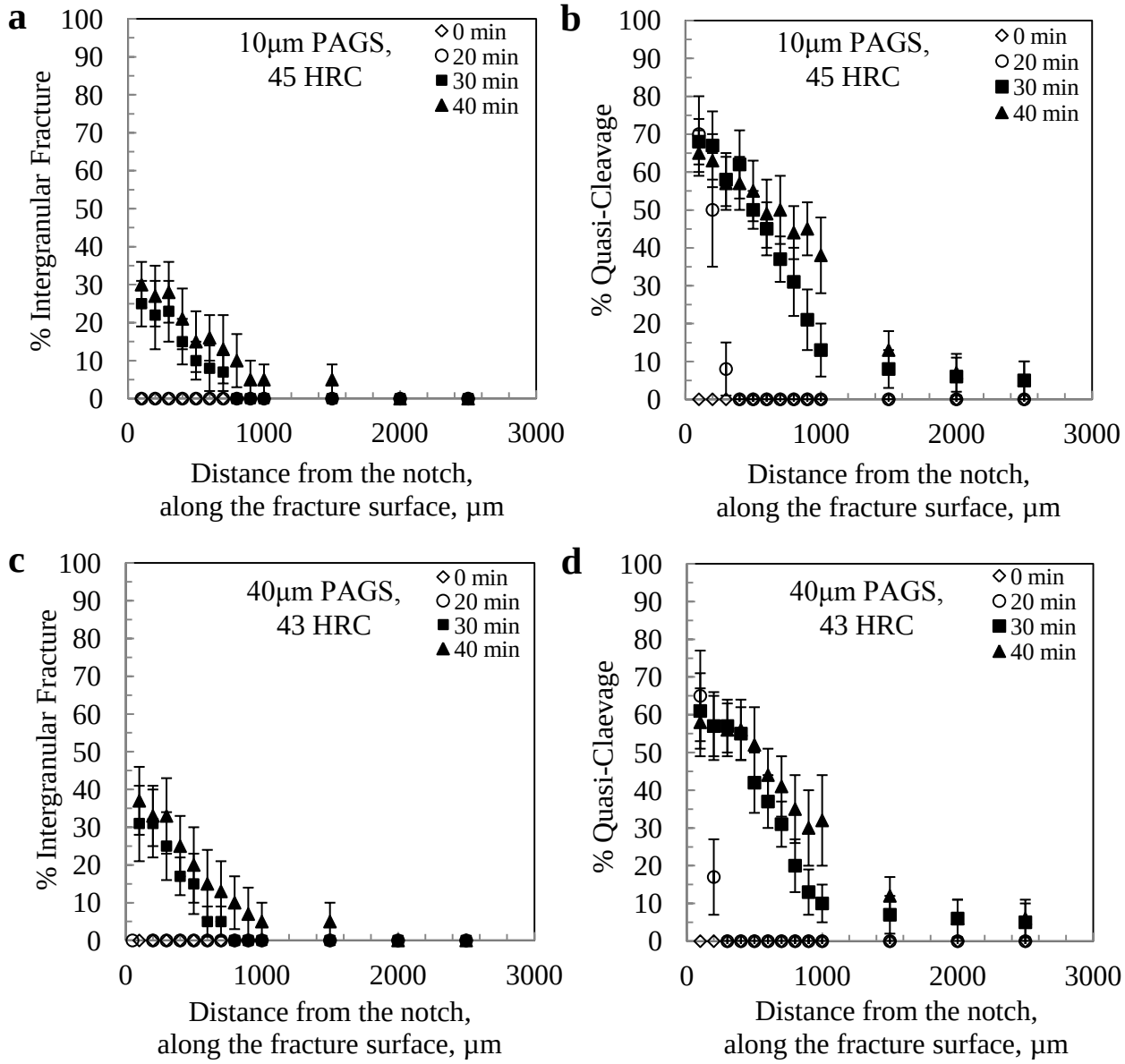

Fig 4.20. Quantitative variation of percent fracture modes with increasing distance from the notch for softer samples for 0, 20, 30 and 40 min hydrogen charging: PAGS and hardnesses are shown in the respective pictures (a) and (c) intergranular, (b) and (d) quasi-cleavage. Each data point represents average of 4 samples. Error bars represent 2σ scatter. Cross-head speed used : 0.01mm/min

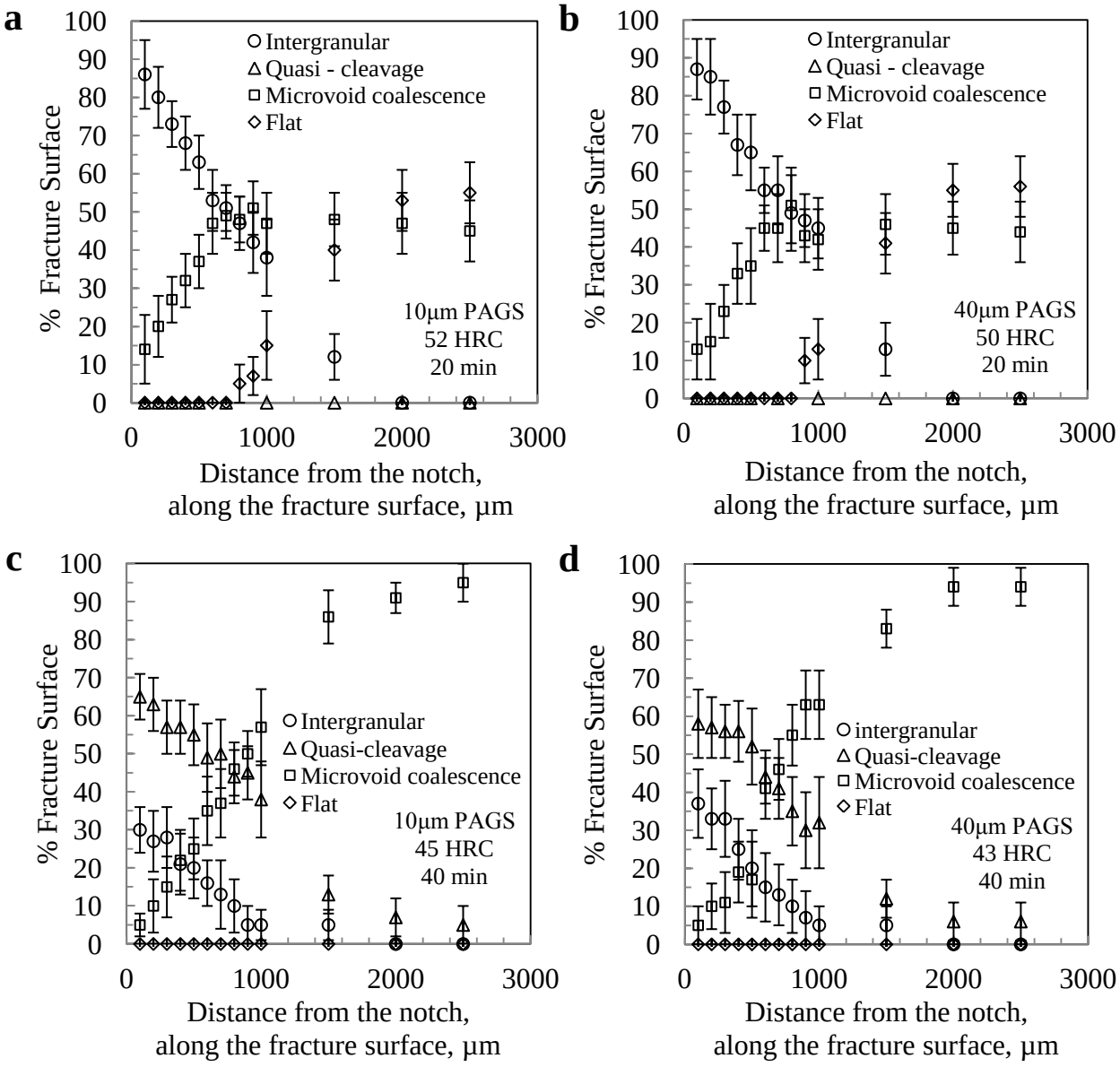

Fig 4.21. Quantitative variation of various fracture modes with increasing distance from the notch for 20 min charged (a) 10μm PAGS, 52 HRC samples (b) 40μm PAGS, 50 HRC and 40 min charged (c) 10μm PAGS, 45 HRC and (d) 40μm PAGS, 43 HRC. Samples loaded at a cross head speed of 0.01 mm/min. Each data point represents average of 4 samples. Error bars represent 2σ scatter.

Fig 4.22 (a) and 4.22(b) present the quantitative variation of percent intergranular fracture and quasi-cleavage with increasing distance from the notch for the 100 μm PAGS 48 HRC samples hydrogen charged for 0, 5 and 10 min while Fig 4.22 (c) and 4.22 (d) present the same results for the 100 μm PAGS 41 HRC samples. The softer samples did not show any evidence of intergranular fracture at any hydrogen charging condition used. Increasing the charging time generally increased the amounts of intergranular and quasi-cleavage fracture and these were found to be a maximum close to the notch for the charged samples.

Fig. 4.23 (a) and 4.23 (b) provide the full fractographic characterization of fracture mode for 10 min of hydrogen charging for 100μm harder and softer samples. The harder sample did not show much change in the various fracture modes as distance from the notch increased. However, the softer sample did show increase in quasi-cleavage mode closer to the notch.

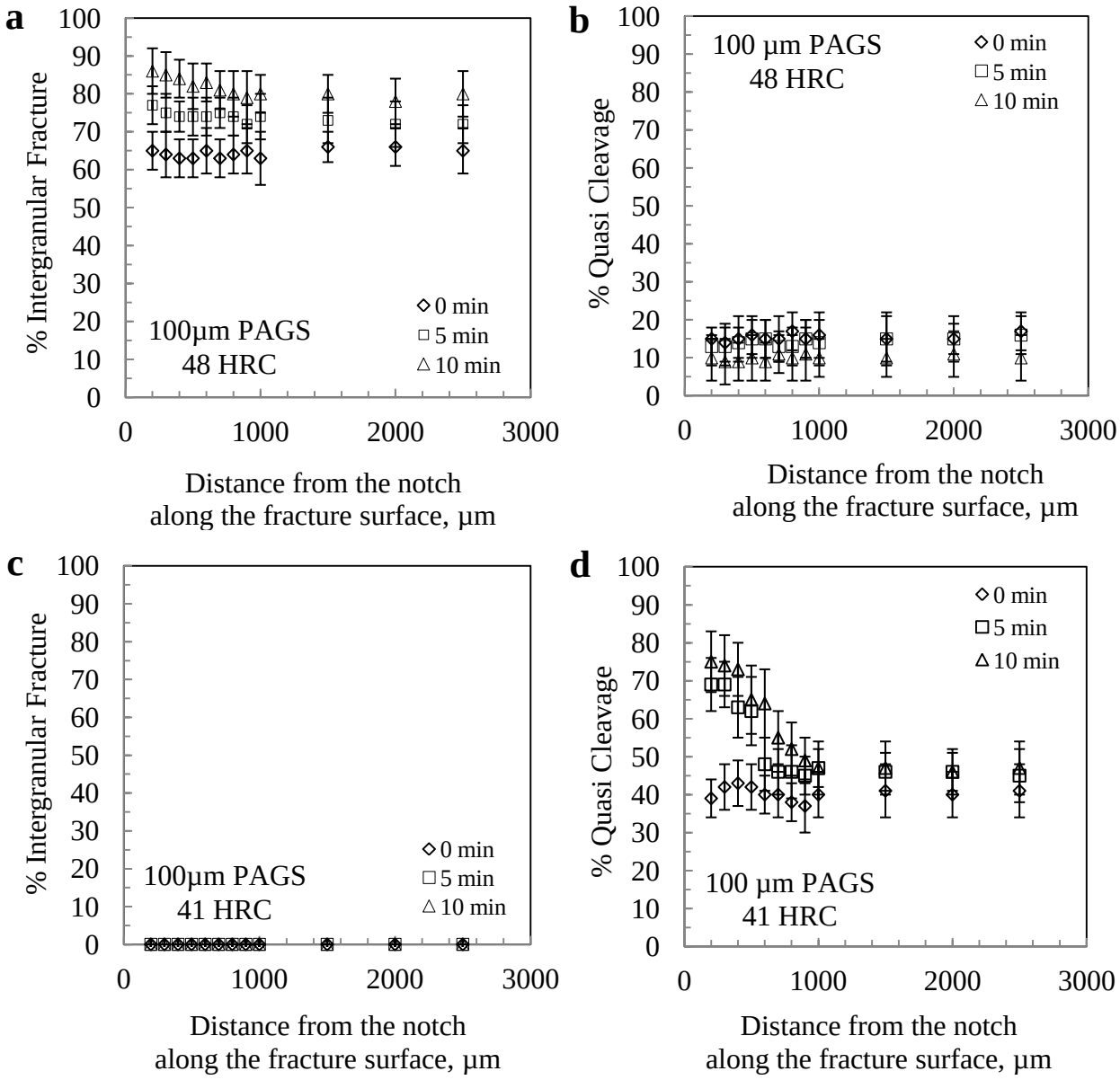

Fig. 4.22. Quantitative variation of percent fracture modes with increasing distance from the notch for harder and softer 100 PAGS samples for 0, 5 and 10 min hydrogen charging: Hardnesses are shown in the respective pictures (a) and (c) intergranular, (b) and (d) quasi-cleavage. Each data point represents average of 4 samples. Error bars represent 2σ scatter. Cross-head speed used : 0.01mm/min

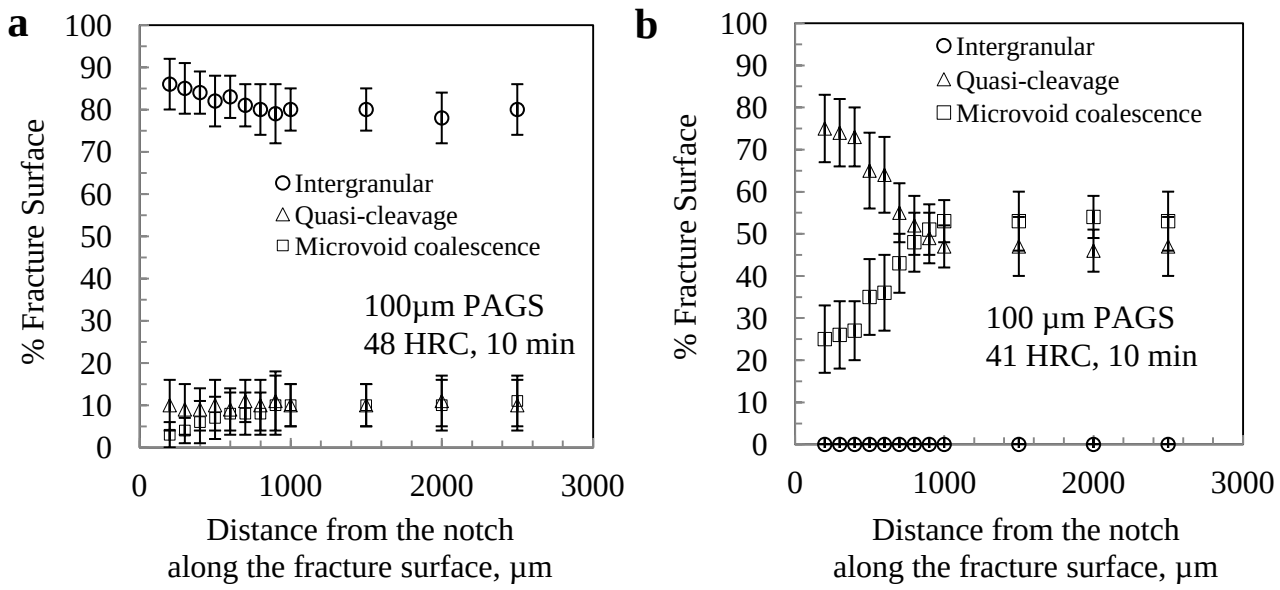

Fig. 4.23. Quantitative Variation of various fracture modes with increasing distance from the notch for 10 min charged, 100µm PAGS harder and softer samples. (a) Harder :48 HRC samples (b) Softer :41 HRC sample. Each data point represents average of 4 samples. Error bars represent 2σ scatter. Cross-head speed used: 0.01 mm/min.

4.3.2 Effects of Strain Rate

Two different strain rates: 2.85×10^{-6} (CHS: 0.01 mm/min) & 8.55×10^{-6} s^{-1} (CHS: 0.03 mm/min) were used in this study. The effects of strain rate were studied for the 10 and 40 µm PAGS samples.

4.3.2.1 Mechanical Response

The average failure strains at 0.01 and 0.03 mm/min cross head speeds are shown in Fig. 4.24 (a) 10 and 40 µm harder samples and Fig. 4.24(b) 10 and 40 µm PAGS softer samples. The failure strains for the control samples (not charged with hydrogen) at two different cross head speeds exhibited similar failure strains. However, the harder samples (52 and 50 HRC) experienced decreases in failure strain for both cross head speeds after only 5 min hydrogen charging. Statistically significant differences in failure strain for the softer samples were observed only above 10 min charging for the lower strain rate tests. Hydrogenated samples tested at the higher strain rate exhibited significantly reduced failure strains compared to the lower strain rate. No statistically significant (95% CL) differences in failure strain values were observed between the 10 and 40 µm PAGS samples.

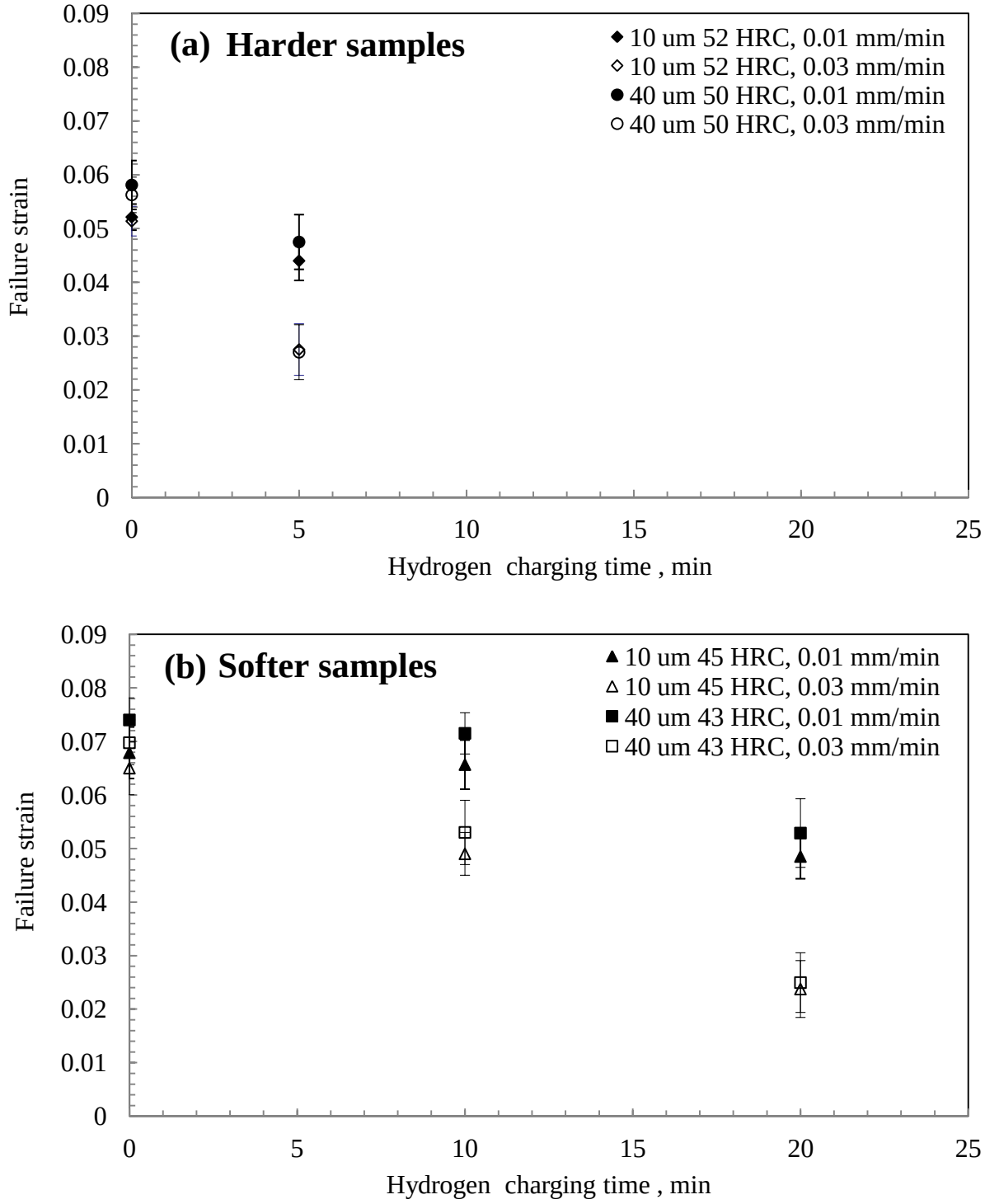

Fig. 4.24. Change in failure strain as function of two strain rates 2.85 x 10^{-6} s^{-1} (CHS: 0.01 mm/min) & 8.55 x 10^{-6} s^{-1} (CHS: 0.03 mm/min): (a) 10 and 40 µm harder samples (50-52 HRC) hydrogen charged for 0 and 5 min, (b) at 10 and 40 µm softer samples (43-45 HRC) hydrogen charged for 0,10 and 20 min. Error bars indicate 2σ scatter.

4.3.2.2 Fracture Behavior

Fig. 4.25 and Fig. 4.26 show representative fracture behavior from approximately 100, 500 µm (close to the notch) and ~ 2000 µm (close to sample centerline) for the uncharged 10 and 40 µm harder samples (50-52 HRC) loaded at two strain rates 2.85 x 10^{-6} s^{-1} (CHS: 0.01 mm/min) and 8.55 x 10^{-6} s^{-1} (CHS: 0.03 mm/min). At both strain rates the fracture surface of the uncharged samples of both grain sizes exhibited similar fracture surfaces dominated by dimples from microvoid coalescence up to a depth of ~ 750 µm and a mixture of dimples and flat surfaces were seen at distance > 750 µm from the notch. Some secondary cracking can be seen in the 40µm PGAS sample near the central line.

Fig. 4.27 and Fig 4.28 respectively show representative fracture behavior from approximately 100, 500 µm (close to the notch) and ~ 2000 µm (close to sample centerline) for the 5 min charged 10 and 40 µm harder samples (50-52 HRC) loaded at two strain rates 2.85 x 10^{-6} s^{-1} (CHS: 0.01 mm/min) and 8.55 x 10^{-6} s^{-1} (CHS: 0.03 mm/min). For 5 mins charging, even though both the samples showed evidence of intergranular fracture, the sample subjected to relatively higher strain rate exhibited greater amount of intergranular fracture close to the notch. However, away from the notch both samples showed fracture behavior similar to their uncharged counterparts under same conditions.

Fig. 4.29 and Fig 4.30 respectively show representative fracture behavior from approximately 100, 500 µm (close to the notch) and ~ 2000 µm (close to sample centerline) for the uncharged 10 and 40 µm softer samples (43-45 HRC) loaded at two strain rates 2.85 x 10^{-6} s^{-1} (CHS: 0.01 mm/min) and 8.55 x 10^{-6} s^{-1} (CHS: 0.03 mm/min).The uncharged softer samples at both strain rates showed dimples representative of microvoid coalescence at all distance from the notch with no evidence of flat surfaces away from the notch. However, the average value of

the flat surface fraction was observed to be more for higher strain rate apparently because of some existing hydrogen at the interior of the sample.

Fig. 4.31 and Fig 4.32 respectively show representative fracture behavior from approximately 100, 500 µm (close to the notch) and ~ 2000 µm (close to sample centerline) for the 20 min charged 10 and 40 µm softer samples (43-45 HRC) loaded at two strain rates 2.85 x 10^{-6} s^{-1} (CHS: 0.01 mm/min) and 8.55 x 10^{-6} s^{-1} (CHS: 0.03 mm/min). Sample loaded at lower strain rate showed no prominent evidence of intergranular fracture but only quasi-cleavage restricted within 200 µm from the notch. On the other hand, the sample loaded at higher strain rate exhibited evidence of both intergranular fracture and predominant quasi-cleavage. Both quasi-cleavage and intergranular fracture were observed to be maximum close to the notch and then decreased as the distance from the notch increased. For higher strain rates, evidence of small fraction (~10 %) of quasi cleavage also observed away from the notch presumably because of some existing hydrogen at the interior of the sample.

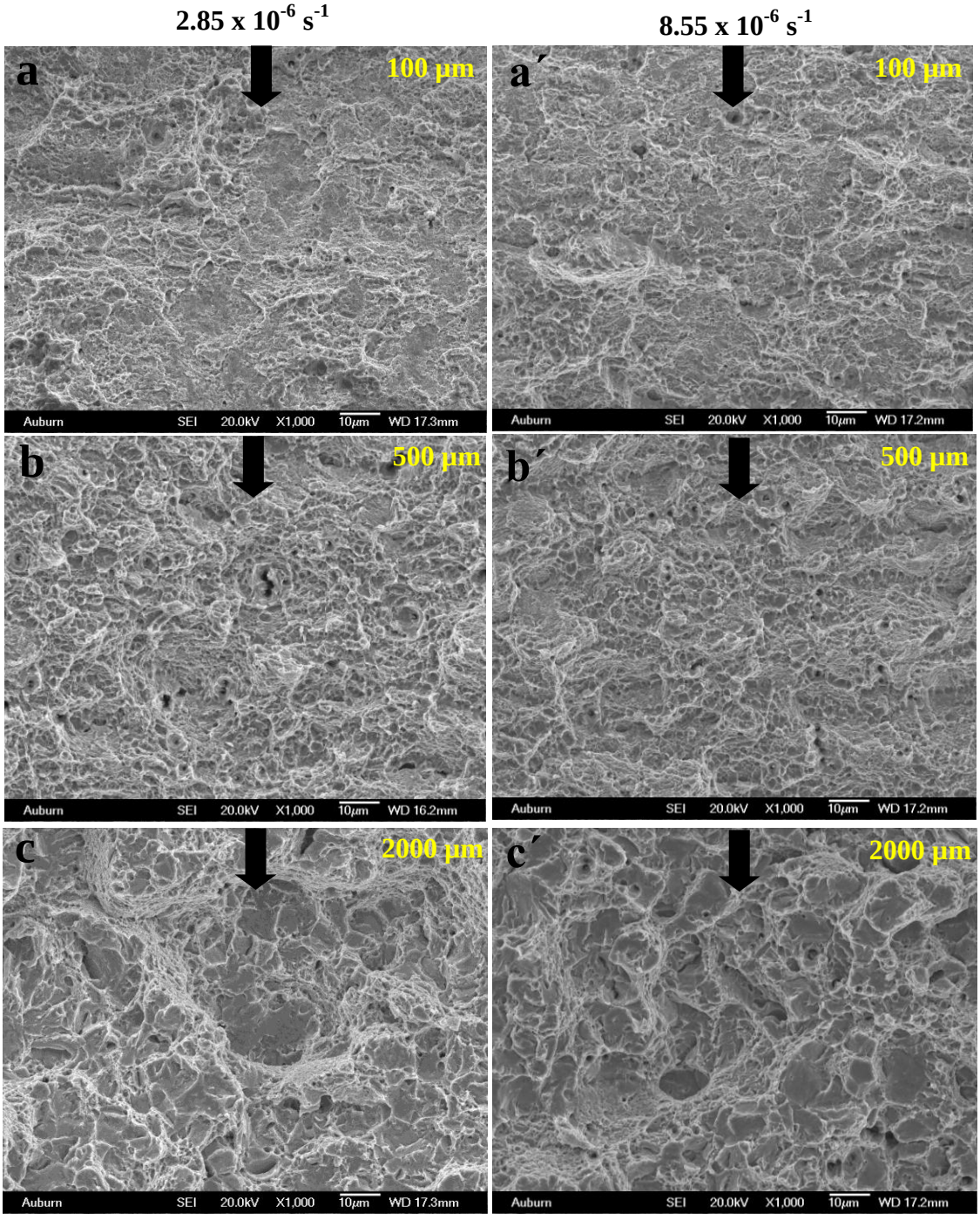

Fig. 4.25. Fracture characteristics with increasing distance from the notch for uncharged 10µm PAGS, 52 HRC samples for two different strain rates 2.85 x 10^{-6} s^{-1} (CHS: 0.01 mm/min) (a- c) and 8.55 x 10^{-6} s^{-1} (CHS: 0.03 mm/min) (a´- c´). Strain rates and distances from the notch are shown. Arrows indicate the crack growth direction.

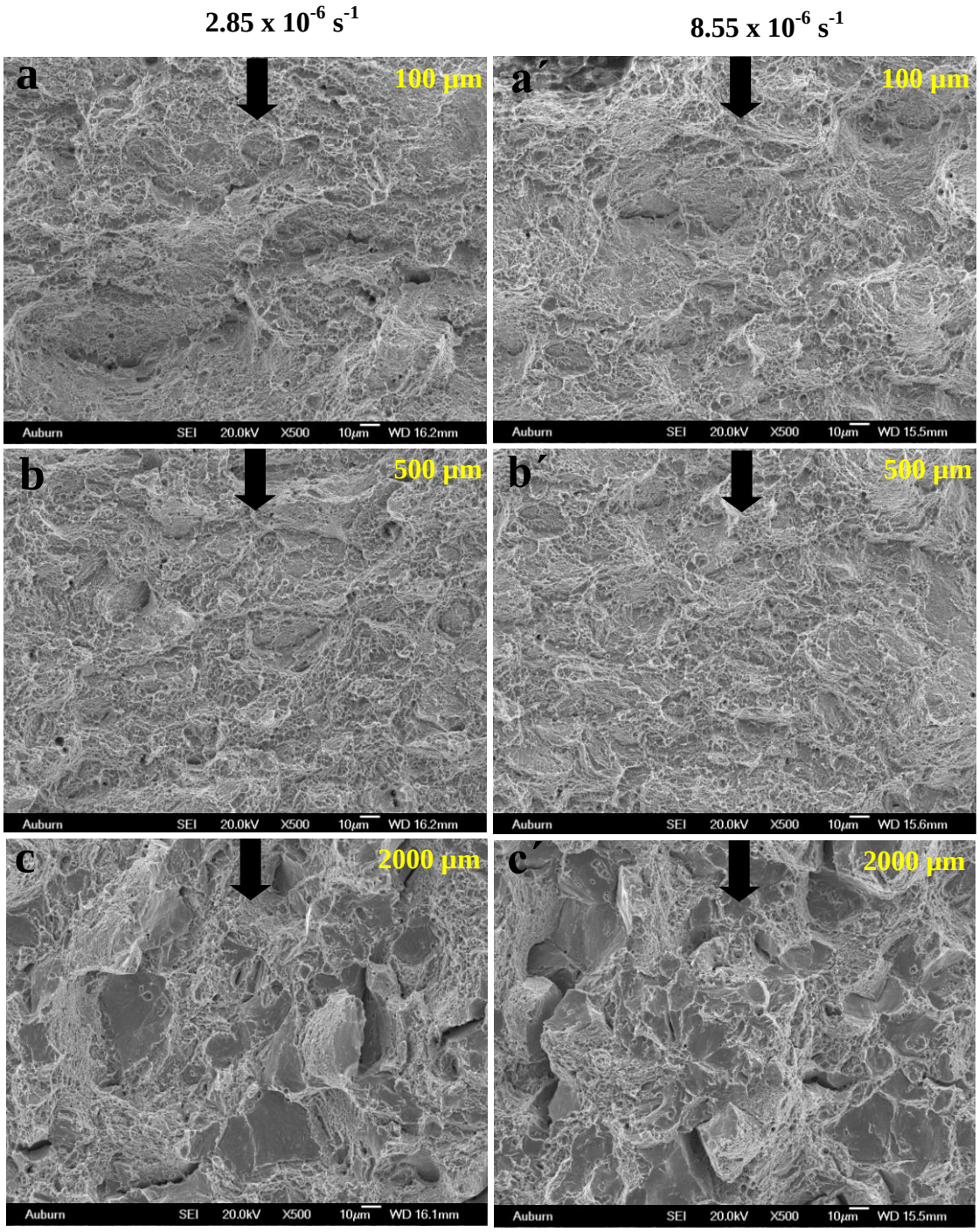

Fig. 4.26. Fracture characteristics with increasing distance from the notch for uncharged 40µm PAGS, 50 HRC samples for two different strain rates 2.85 x 10^{-6} s^{-1} (CHS: 0.01 mm/min) (a- c) and 8.55 x 10^{-6} s^{-1} (CHS: 0.03 mm/min) (a´- c´). Strain rates and distances from the notch are shown. Arrows indicate the crack growth direction.

.

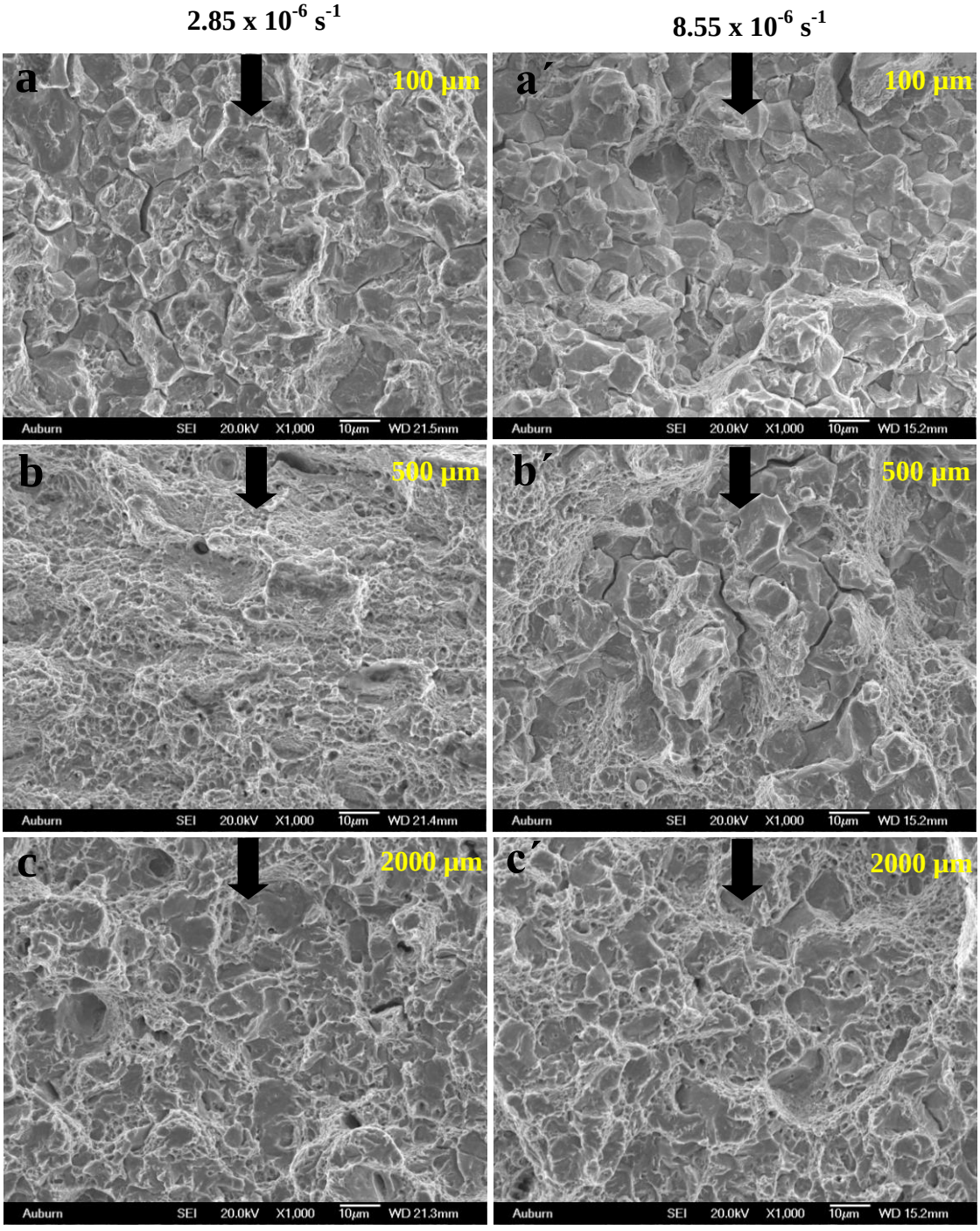

Fig. 4.27. Fracture characteristics with increasing distance from the notch for 5 min charged 10µm PAGS, 52 HRC samples for two different strain rates 2.85 x 10^{-6} s^{-1} (CHS: 0.01 mm/min) (a- c) and 8.55 x 10^{-6} s^{-1} (CHS: 0.03 mm/min) (a´- c´). Strain rates and distances from the notch are shown. Arrows indicate the crack growth direction.

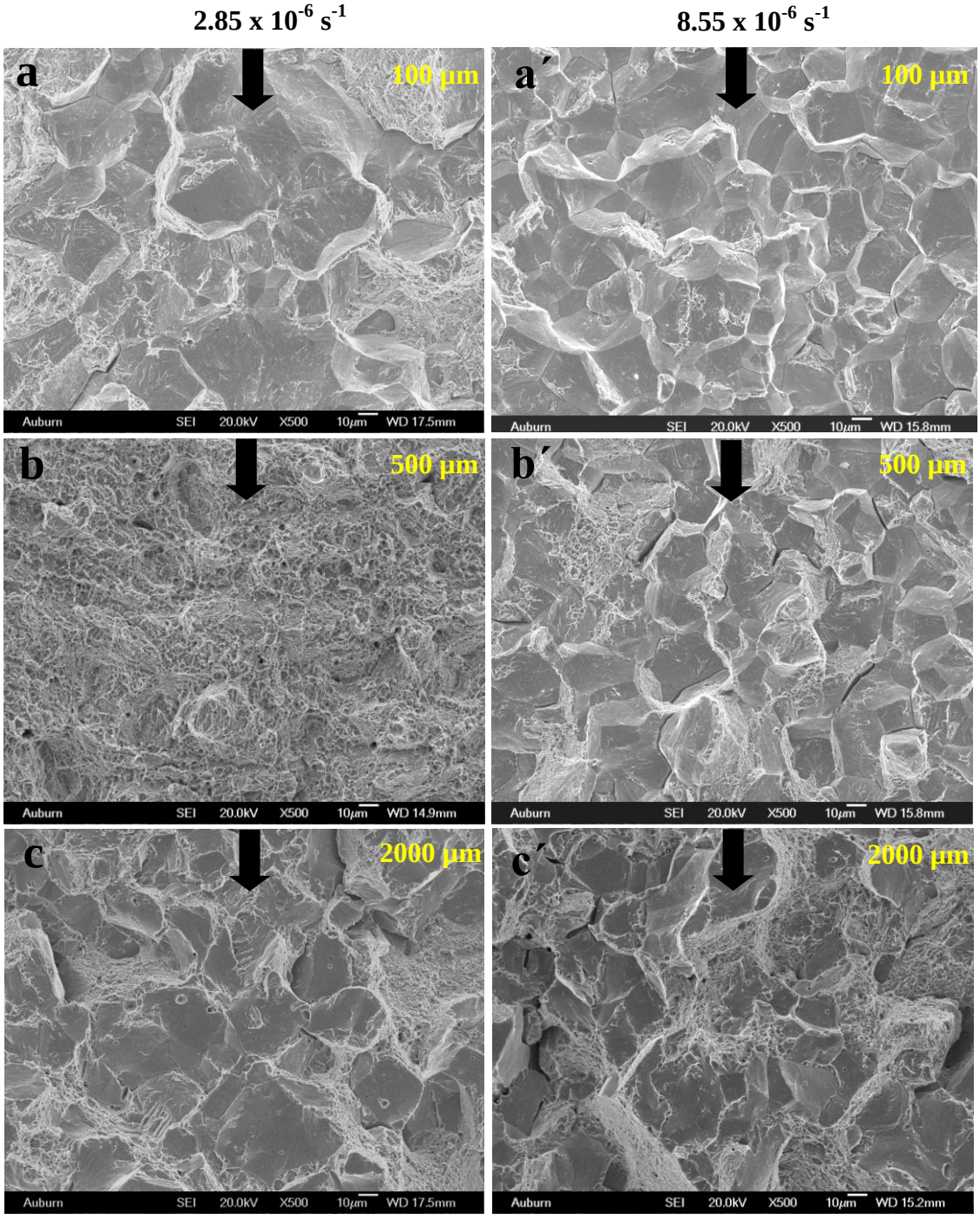

Fig. 4.28. Fracture characteristics with increasing distance from the notch for 5 min charged 40µm PAGS, 50 HRC samples for two different strain rates 2.85 x 10^{-6} s^{-1} (CHS: 0.01 mm/min) (a- c) and 8.55 x 10^{-6} s^{-1} (CHS: 0.03 mm/min) (a´- c´). Strain rates and distances from the notch are shown. Arrows indicate the crack growth direction.

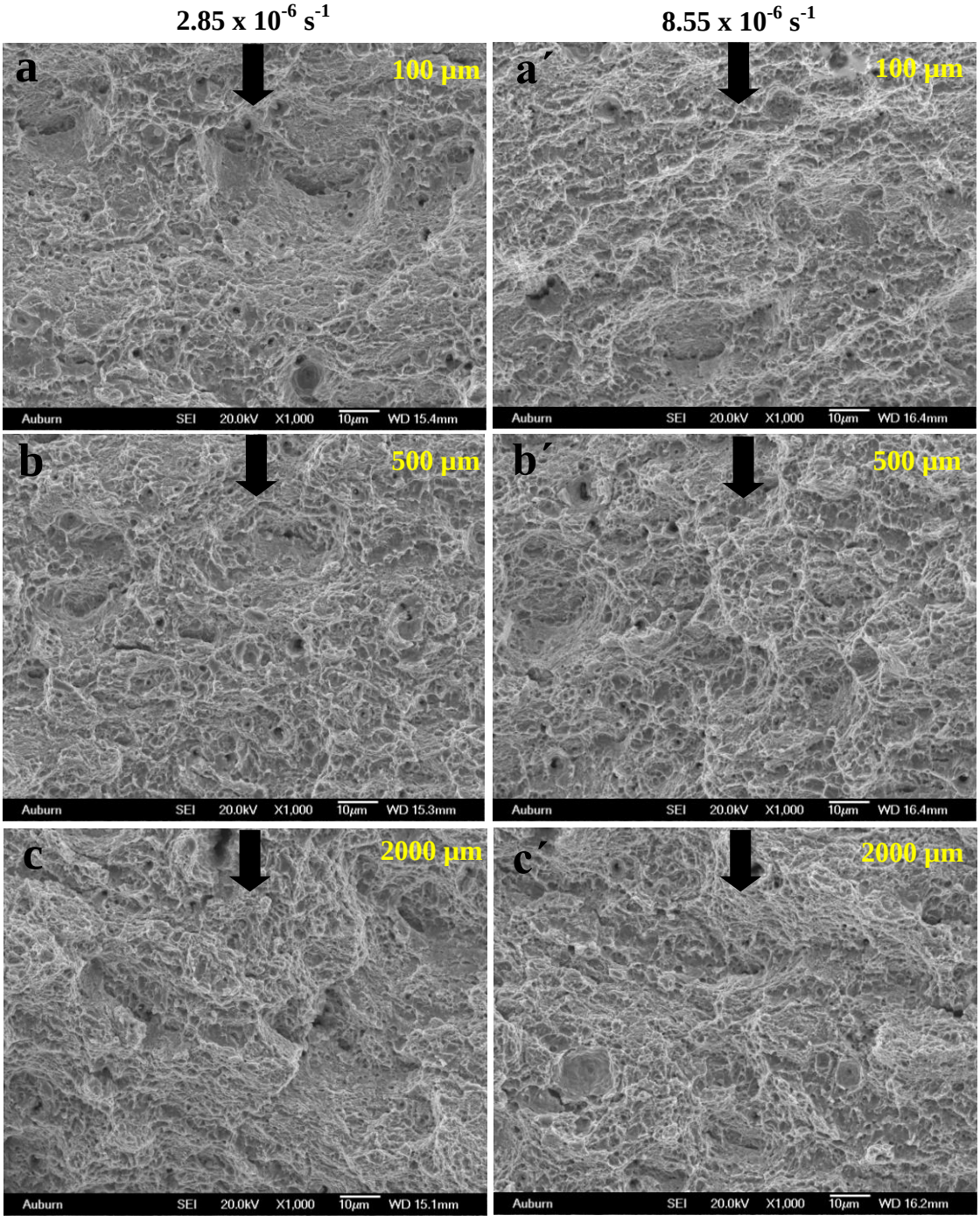

Fig. 4.29. Fracture characteristics with increasing distance from the notch for uncharged 10µm PAGS, 45HRC samples for two different strain rates 2.85 x 10^{-6} s^{-1} (CHS: 0.01 mm/min) (a-c) and 8.55 x 10^{-6} s^{-1} (CHS: 0.03 mm/min) (a´ - c´). Strain rates and distances from the notch are shown. Arrows indicate the crack growth direction.

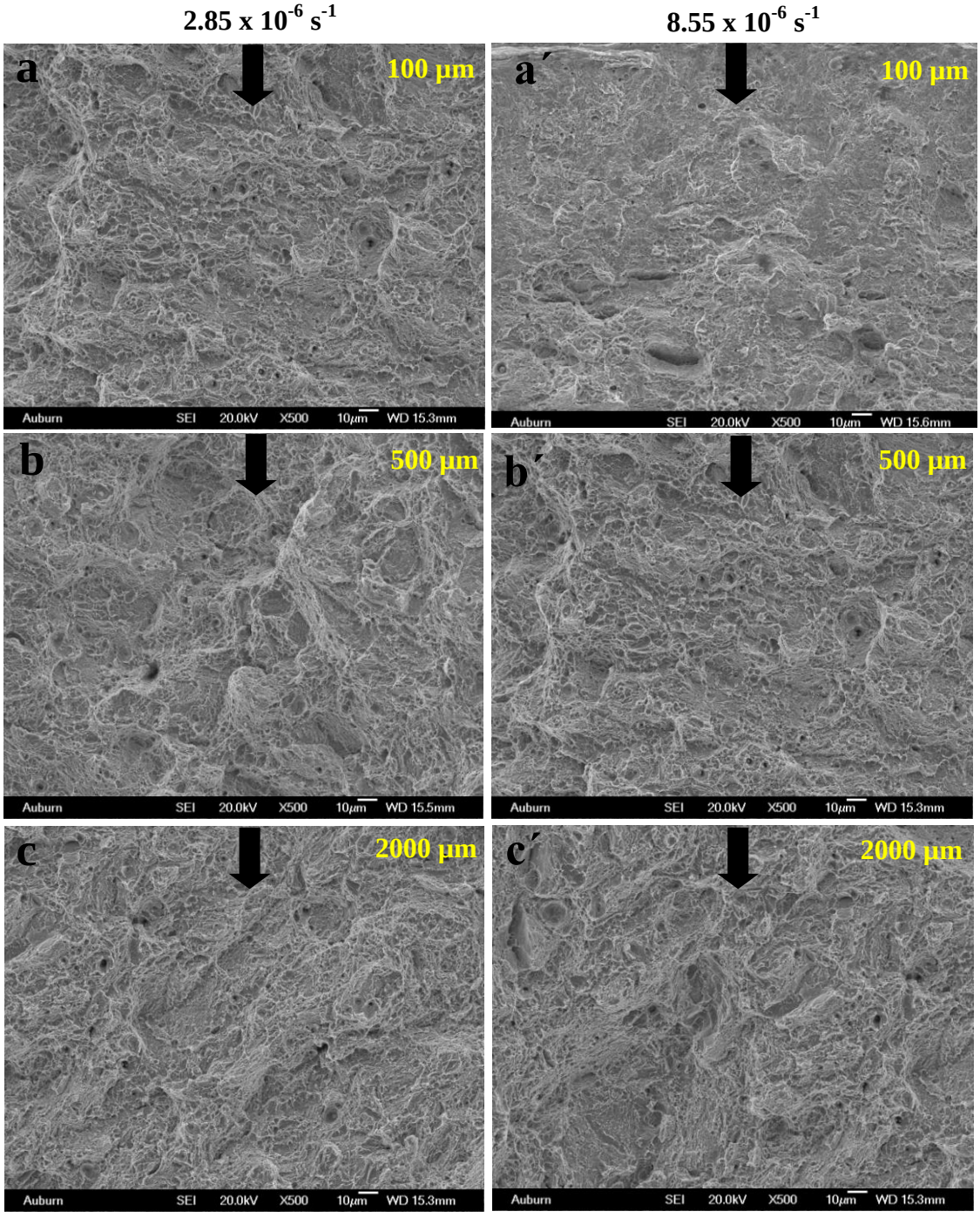

Fig. 4.30. Fracture characteristics with increasing distance from the notch for uncharged 40µm PAGS, 43HRC samples for two different strain rates 2.85 x 10^{-6} s^{-1} (CHS: 0.01 mm/min) (a-c) and 8.55 x 10^{-6} s^{-1} (CHS: 0.03 mm/min) (a´ - c´). Strain rates and distances from the notch are shown. Arrows indicate the crack growth direction.

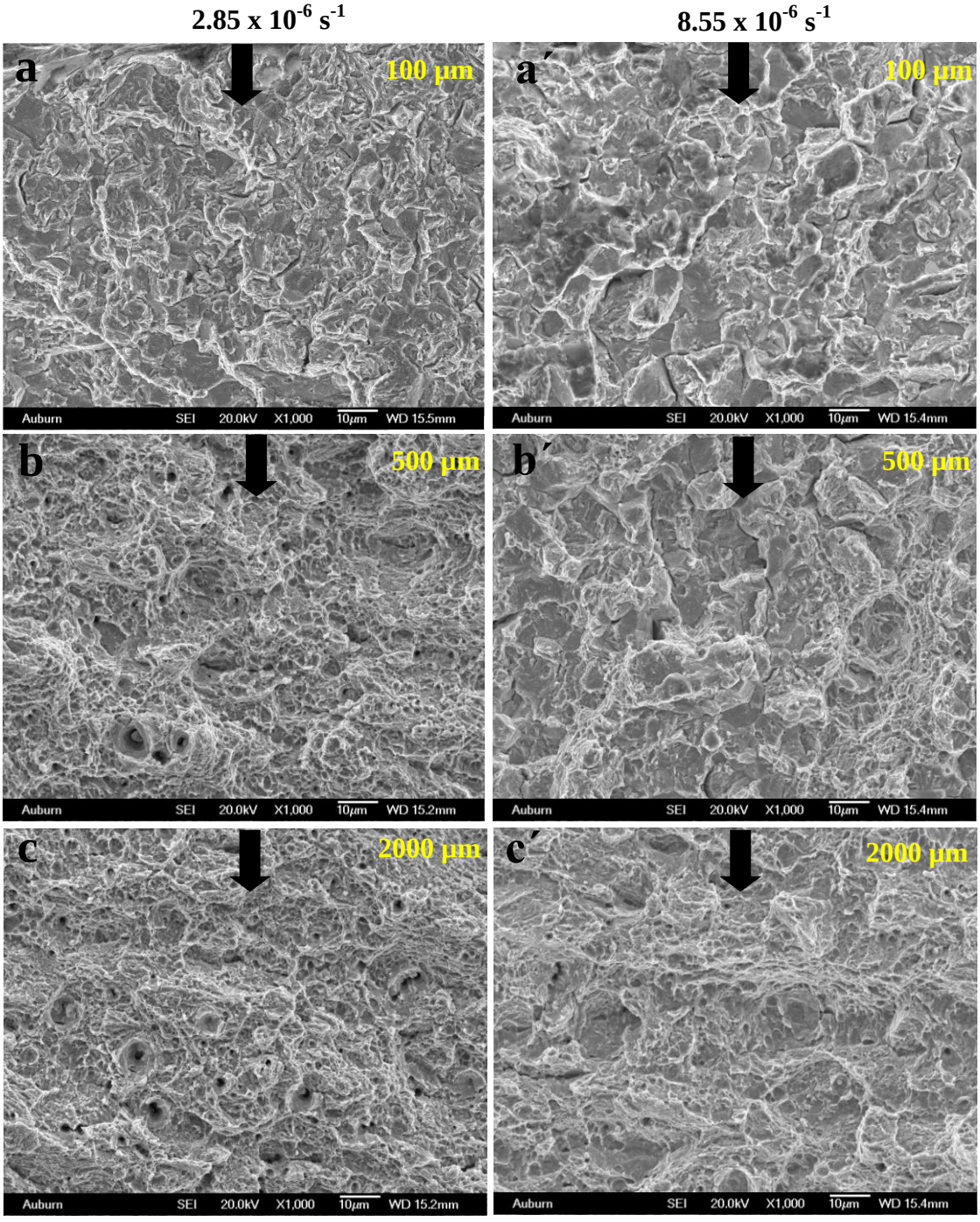

Fig. 4.31. Fracture characteristics with increasing distance from the notch for 20 min charged 10µm PAGS, 45HRC samples for two different strain rates 2.85 x 10^{-6} s^{-1} (CHS: 0.01 mm/min) (a-c) and 8.55 x 10^{-6} s^{-1} (CHS: 0.03 mm/min) (a´ - c´). Strain rates and distances from the notch are shown. Arrows indicate the crack growth direction.

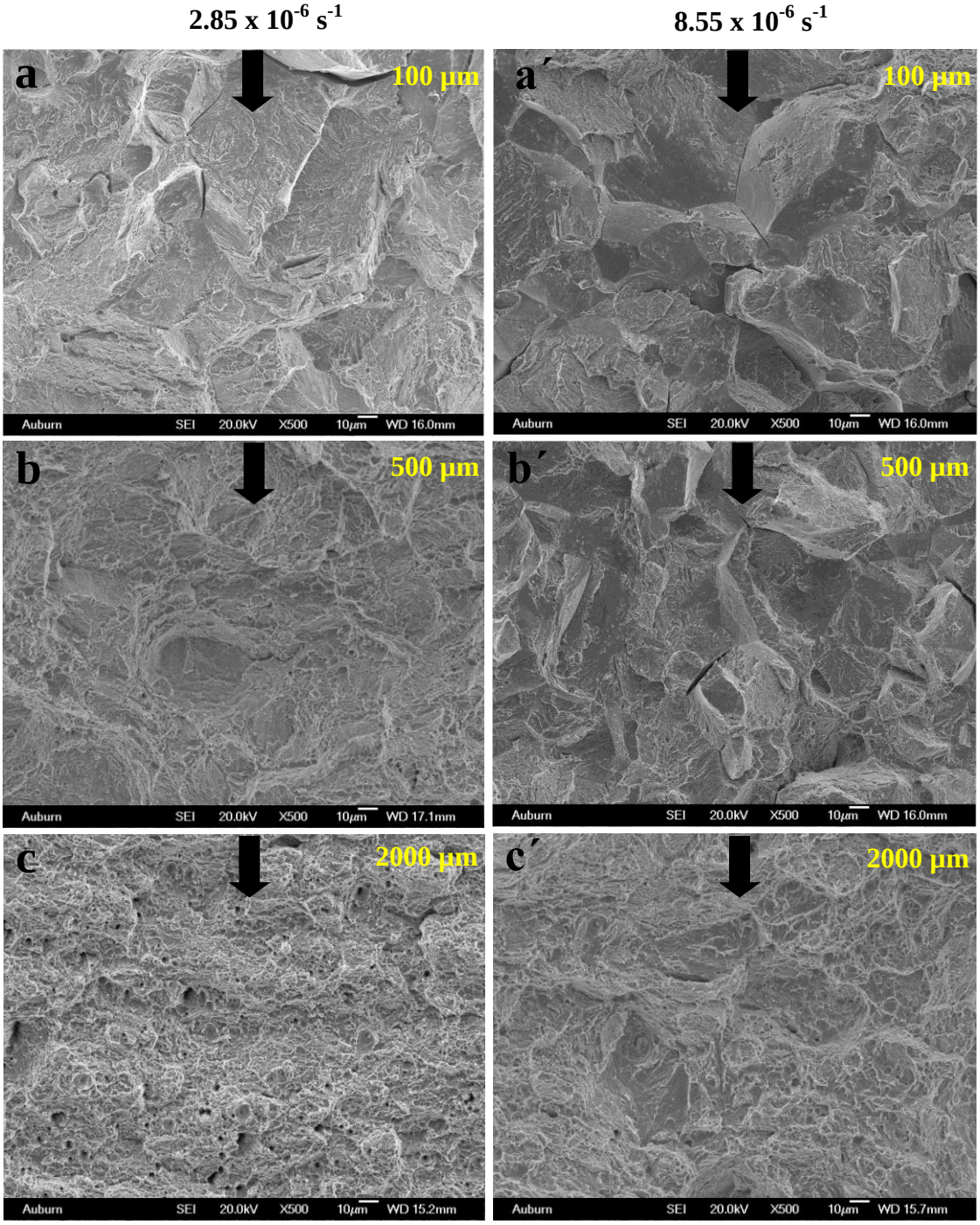

Fig. 4.32. Fracture characteristics with increasing distance from the notch for 20 min charged 40µm PAGS, 43HRC samples for two different strain rates 2.85 x 10^{-6} s^{-1} (CHS: 0.01 mm/min) (a-c) and 8.55 x 10^{-6} s^{-1} (CHS: 0.03 mm/min) (a´ - c´). Strain rates and distances from the notch are shown. Arrows indicate the crack growth direction.

Fig 4.33 (a) and Fig 4.33 (b present the quantitative variation of percent intergranular fracture and flat surfaces with increasing distance from the notch for the 10 µm, 52 HRC samples hydrogen charged for 0 and 5 min and loaded strain rates of 2.85 x 10^{-6} s^{-1} and 8.55 x 10^{-6} s^{-1} . Fig 4.33 (c) and 4.33 (d) present the same results for the 40 µm, 50 HRC samples. The unhydrogenated samples did not show any evidence of intergranular failure at either of the strain rates used while the 5 min hydrogenated sample did exhibit evidence of intergranular failure. However, the amount of intergranular fracture was intensity and depth of the intergranular fracture were observed to increase for the sample subjected to the higher strain rate (8.55 x 10^{-6} s^{-1}).

Fig. 4.34 (a) and 4.34 (b) provide the full characterization of fracture mode for 5 min charged 10 µm, 52 HRC samples at strain rates of 2.85 x 10^{-6} s^{-1} and 8.55 x 10^{-6} s^{-1} respectively. Fig. 4.34 (c) and 4.34 (d) provide the same result for 5 min charged 40 µm, 50 HRC samples. The 5 min charged samples tested at the lower strain rate showed intergranular fracture only up to a ~ 300-400 µm away from the notch while the 5 min charged samples tested at the higher strain rate showed significant intergranular fracture up to 700 µm away from the notch.

Fig 4.35 (a) and Fig 4.35b(b) show the quantitative variation of percent intergranular and quasi-cleavage fracture with increasing distance from the notch for the 10 µm, 45 HRC samples hydrogen charged for 0 and 20 min and loaded strain rates of 2.85 x 10^{-6} s^{-1} and 8.55 x 10^{-6} s^{-1} . Fig 4.35 (c) and 4.35 (d) present the same results for the 40 µm, 43 HRC samples. The unhydrogenated samples did not show any evidence of intergranular failure or quasi-cleavage at any of the strain rates used while the 20 min hydrogenated samples at higher strain rate exhibited evidence of both intergranular failure as well as quasi-cleavage with the later being predominant. However, no significant intergranular fracture was observed for the 20 min

hydrogenated sample loaded at lower strain rate. The amount of intergranular fracture was observed to increase for the sample subjected to relatively higher strain rate (8.55×10^{-6} s^{-1}). This is presumably because of the lower loss of hydrogen from the sample before the stress level reached the required critical value in order to cause fracture.

Fig. 4.36 (a) and 4.36 (b) present the full characterization of fracture mode for the 20 min charged 10 µm, 45 HRC samples at strain rates of 2.85×10^{-6} s^{-1} and 8.55×10^{-6} s^{-1}, respectively. Fig. 4.36 (c) and 4.36 (d) provide the same result for 20 min charged 40 µm, 43 HRC samples. For samples loaded at lower strain rates, intergranular fracture was not observed and quasi-cleavage was only observed within ~200 µm from the notch. Depth greater than ~200 µm away from the notch only exhibited ductile fracture via microvoid coalescence. The 20 min charged softer samples subjected to the higher strain rate showed a mixture of quasi-cleavage and intergranular fracture up to a distance ~ 1000 µm from the notch. Thereafter the fracture mode was dominated by microvoid coalescence. No flat featureless surfaces, unlike the harder samples away from the notch, were observed in the softer samples.

The amount of intergranular fracture (5 min hydrogenated harder samples) and quasi-cleavage (20 min hydrogenated softer samples) were observed to increase for the samples subjected to relatively higher strain rate (8.55×10^{-6} s^{-1}).This is presumably because of the lower loss of hydrogen from the sample before the stress level reached the required critical value in order to cause embrittlement. In the case of the higher strain rate, the required critical stress level would be reached earlier than the case of the lower strain rate due to: (i) more hydrogen left inside the sample before diffusion out, (ii) stress level increased at a faster rate because of the higher strain rate. Therefore in the case of the higher strain rate the critical combination of

hydrogen concentration and stress applied would be reached more quickly than that in the case of the lower strain rate.

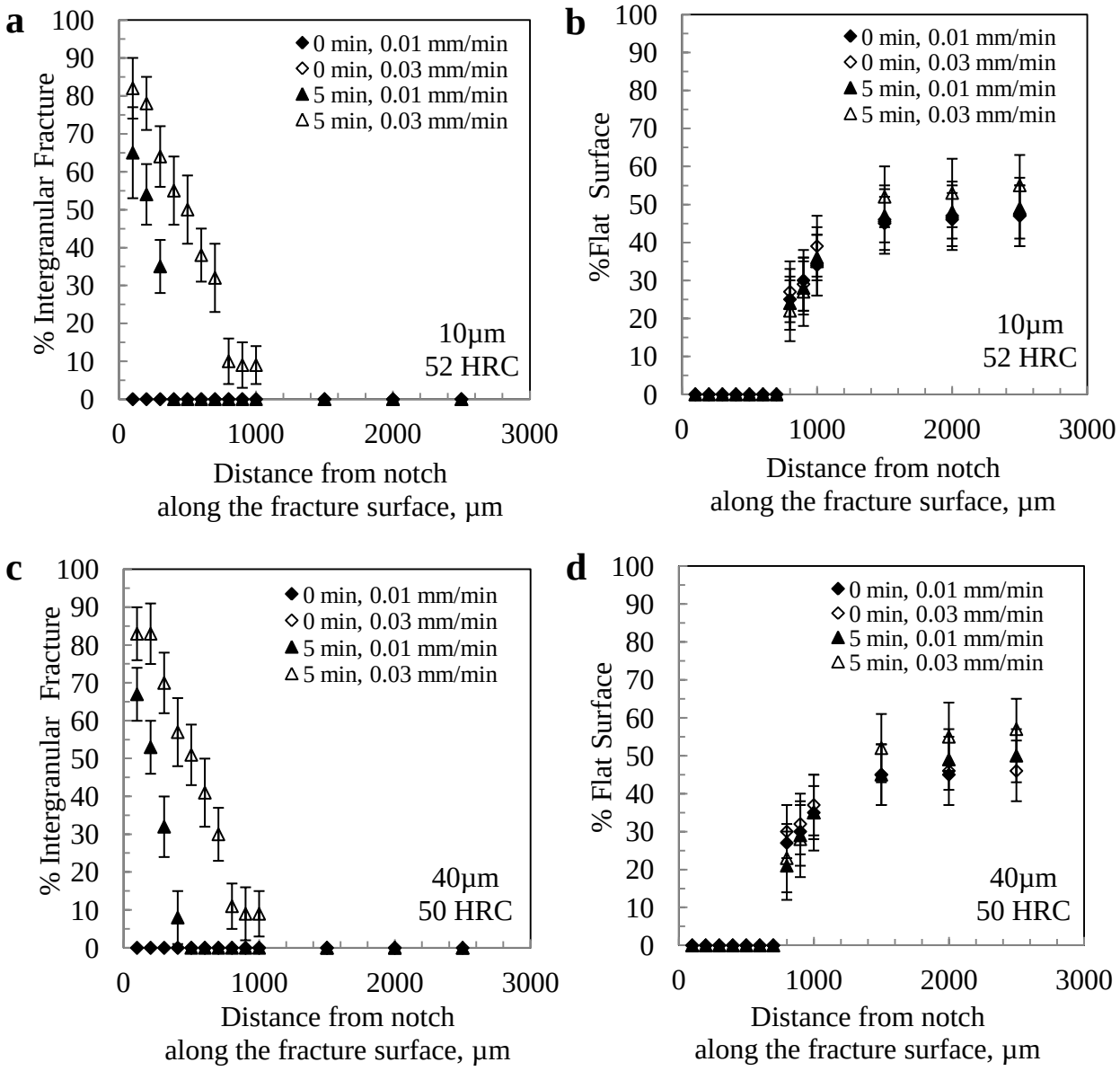

Fig. 4.33. Quantitative variation of percent intergranular and flat surface modes with increasing distance from the notch for 10 and 40 µm PAGS harder (50-52 HRC) samples for two different strain rates speeds of 2.85×10^{-6} s^{-1} (CHS: 0.01 mm/min) and 8.55×10^{-6} s^{-1}(CHS: 0.03 mm/min) after 0 and 5 min hydrogen charging. (a) and (c) intergranular , (b) and (d) flat surfaces. Each data point represents average of 4 samples. Error bars represent 2σ scatter.

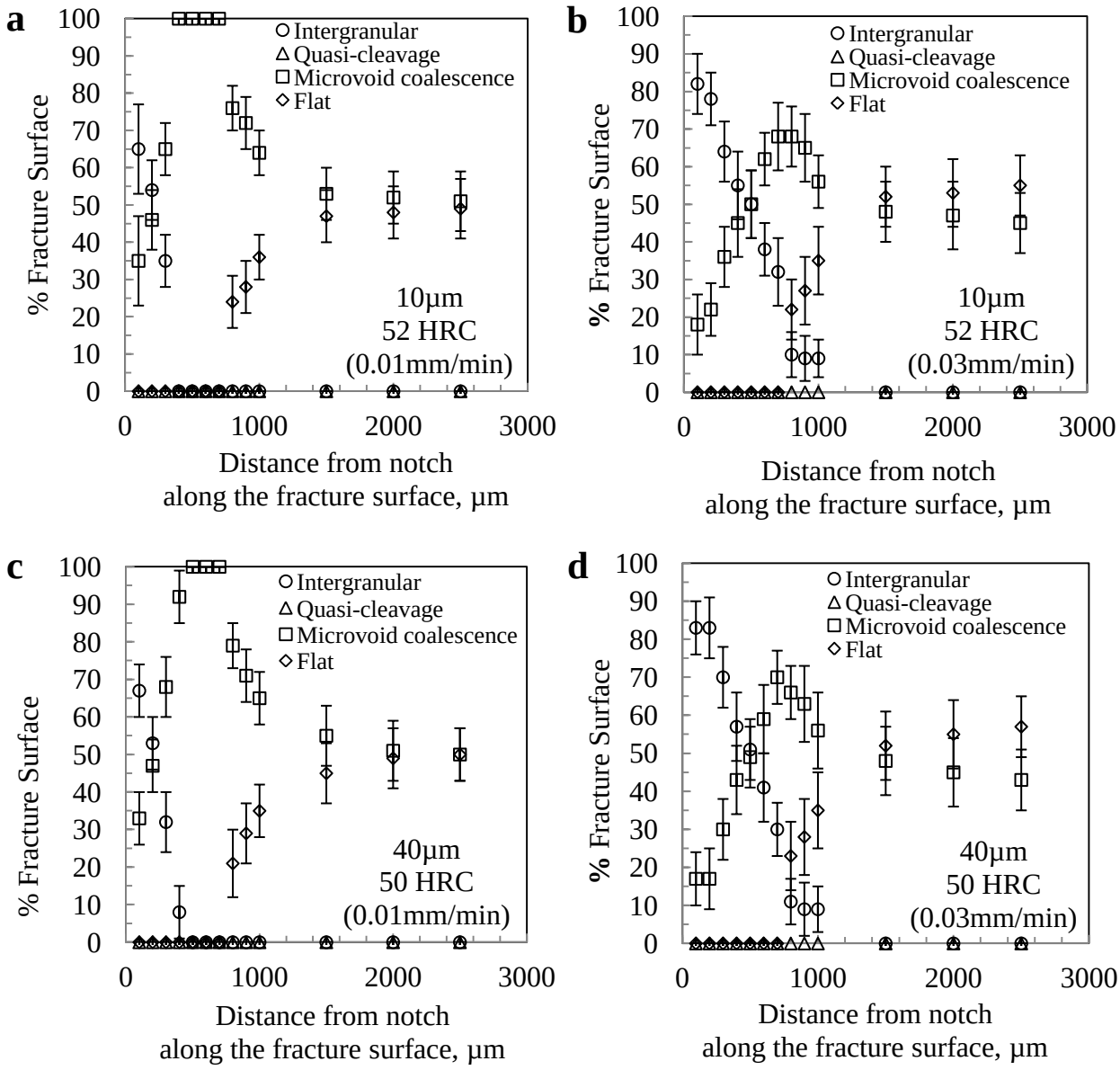

Fig. 4.34. Quantitative variation of various fracture modes with increasing distance from the notch 10 and 40 µm harder (50-52 HRC) samples for two different strain rates speeds of 2.85×10^{-6} s^{-1} (CHS: 0.01 mm/min) and 8.55×10^{-6} s^{-1}(CHS: 0.03 mm/min) after 5 min hydrogen charging. Each data point represents average of 4 samples. Error bars represent 2σ scatter.

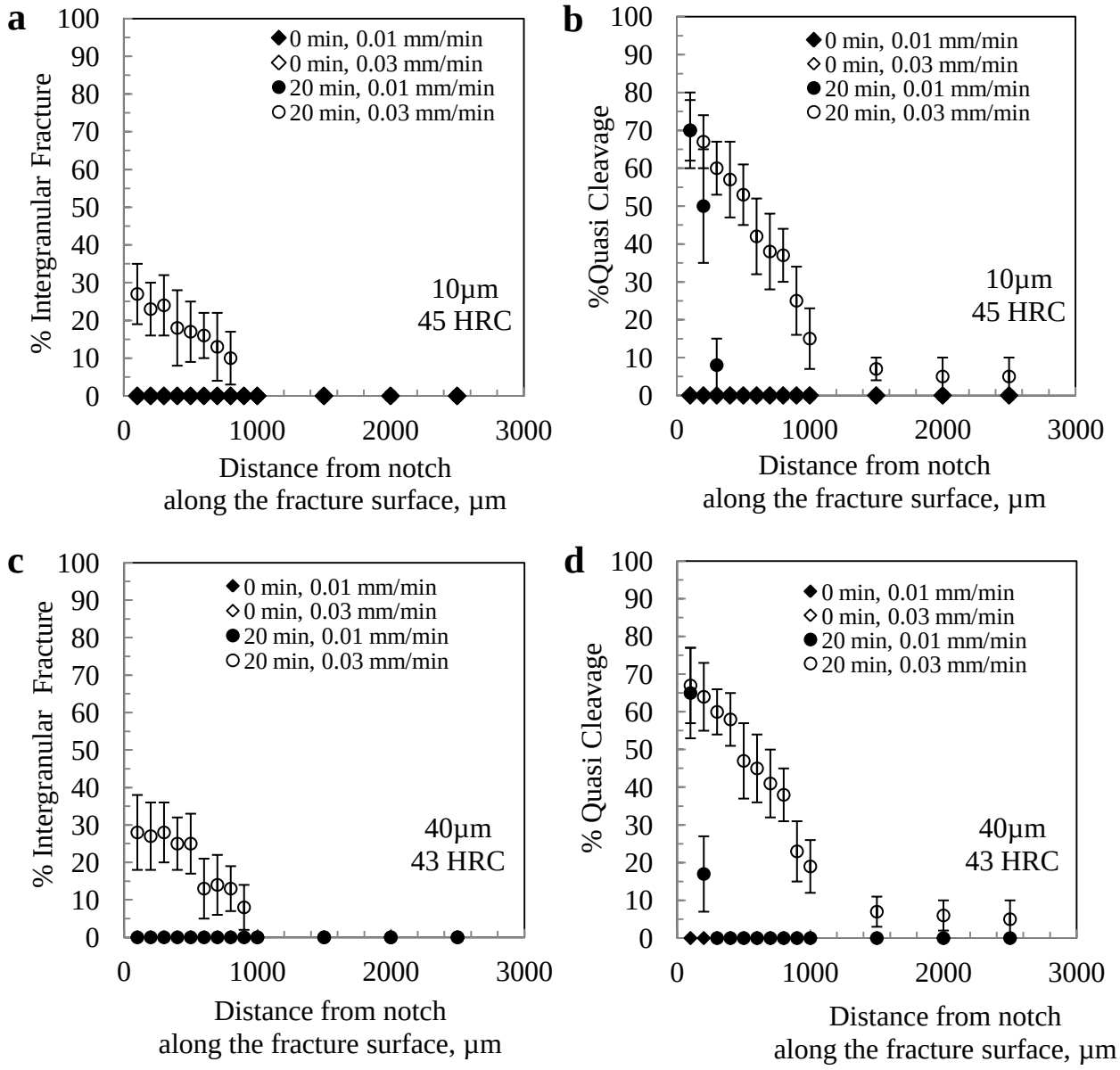

Fig. 4.35. Quantitative variation of percent intergranular and flat surface modes with increasing distance from the notch for 10 and 40 µm PAGS softer (43-45 HRC) samples for two different strain rates speeds of 2.85×10^{-6} s^{-1} (CHS: 0.01 mm/min) and 8.55×10^{-6} s^{-1}(CHS: 0.03 mm/min) after 0 and 20 min hydrogen charging. (a) and (c) intergranular , (b) and (d) quasi-cleavage surfaces. Each data point represents average of 4 samples. Error bars represent 2σ scatter.

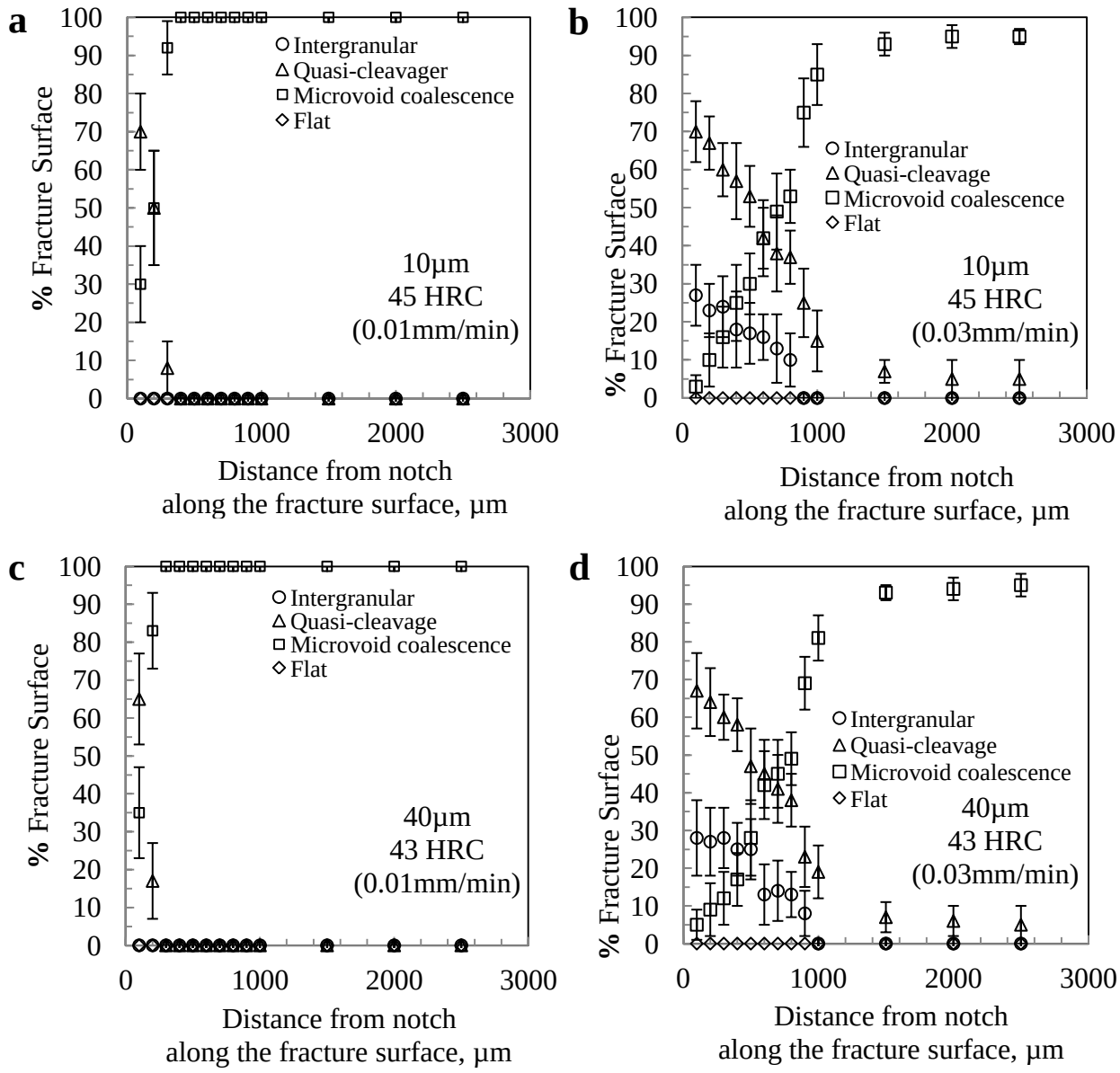

Fig. 4.36. Quantitative variation of various fracture modes with increasing distance from the notch 10 and 40 µm softer (43-45 HRC) samples for two different strain rates speeds of 2.85×10^{-6} s^{-1} (CHS: 0.01 mm/min) and 8.55×10^{-6} s^{-1}(CHS: 0.03 mm/min) after 20 min hydrogen charging. Each data point represents average of 4 samples. Error bars represent 2σ scatter.

5. Summary Remarks and Conclusions

5.1. VHP Treatment

Exposure of low-alloy, high strength 4340 steel to water vapor with 500 or 1000ppm hydrogen peroxide vapor as well as 35 wt.% liquid H_2O_2 for 4.8 h did not lead to hydrogen embrittlement per ASTM 519E-06. However, the operation of vaporized hydrogen peroxide decontamination processes at 1300 or 1600ppm hydrogen peroxide concentration can lead to significant condensation with very high concentrations of H_2O_2 (60–70 wt.% H_2O_2) in the condensed liquid. In fact, vaporized hydrogen peroxide treatments at 1600ppm hydrogen peroxide concentration for 4.8 h led to extensive condensation of high H_2O_2 concentration (~ 64 wt.% H_2O_2) in the process chamber and hydrogen embrittlement of the steel per ASTM 519E-06.

5.2. Electrochemical Hydrogenation

Effects of hydrogen on embrittlement characteristics of low alloy 4340 steel was studied using double-notched tensile samples that were electrochemically charged in-situ with hydrogen in a 0.5 M H_2SO_4 + 5 mg/l As_2O_3 solution. The mechanical response and fracture behavior of samples with prior austenitic grain sizes of 10-100 μm, with martensitic hardness of 41-52 HRC were examined after hydrogen charging times of 0-40 min. Two different cross head speeds (0.01 mm/min and 0.03 mm/min) generating strain rates of 2.85×10^{-6} & 8.55×10^{-6} s^{-1} were employed. Data quantifying the observed fracture modes were observed using scanning electron microscopy (i.e., intergranular, quasi-cleavage, flat cleavage-like or ductile microvoid dimples).

The observed failure strain (ε_f) generally decreased with increasing hydrogen charging time. For similar prior austenitic grain sizes, failure strains of the softer samples were noticeably

larger than the failure strains of the harder samples. The softer samples did not show any statistically significant difference in failure strain before 20 min hydrogen charging. No statistically significant difference in failure strain was observed between the 10 and 40 μm PAGS samples. However, further increases of grain size to 100 μm resulted in significant decreases in ε_f.

For 10 and 40 μm grain size harder samples decreases in ε_f were significant even after 5 min of hydrogen charging and were accompanied by intergranular fracture at their fracture surfaces. Harder samples at these grain sizes showed increase in percent intergranular fracture with increase in hydrogen charging time. Intergranular fracture was predominant closer to the notch while a combination of ductile and flat, cleavage-like fracture was exhibited away from the notch.

Softer samples with grain sizes 10 and 40 μm showed statistically significant decreases in ε_f and noticeable changes in fracture behavior compared to their uncharged counterparts only after 20 min of hydrogen charging. Softer samples charged for greater than 20 mins showed mainly quasi-cleavage mixed with intergranular fracture close to the notch and increasingly ductile fracture as distance from the notch increased.

100 μm grain size harder as well as softer samples showed brittle behavior even in absence of hydrogen, in agreement with their low failure strains. However, presence of hydrogen in 100 μm grain size samples enhanced the brittle behavior and further deterioration of the mechanical properties. The 100 μm harder samples showed significant evidence of intergranular fracture mixed with relatively small quasi cleavage while the 100 μm softer sample showed a mixture of quasi-cleavage and dimples. However, the presence of hydrogen enhanced the

intergranular fracture mode in 100µm harder sample and the percent quasi cleavage in 100µm softer samples.

Increasing the strain rates of 2.85×10^{-6} and 8.55×10^{-6} s^{-1} (CHS: from 0.01 to 0.03 mm/min) did not show any significant change in the failure strain and fracture behavior for the uncharged samples. However, charging the sample with hydrogen led to decreases in the failure strains and increases of the amount of intergranular failure and quasi-cleavage failure. The percentages of intergranular fracture (hard samples) and quasi-cleavage fracture (softer samples) were found to be a maximum close to the notch and then decrease as the distance from the notch increased. The higher strain rate samples (CHS: 0.03 mm/min) in both cases exhibited greater amounts of embrittled failure (i.e., intergranular or quasi-cleavage) than the lower strain rate samples (CHS: 0.01 mm/min).

Harder samples tend to fail primarily via intergranular fracture mode along the prior austenitic grain boundaries while the softer samples tend to fail via quasi-cleavage fracture mode across martensitic lath planes and/or along martensitic lath boundaries.

References

1. J. Kafle and D. Qu, "Enhancement of Hydrogen Insertion into Carbon Interlayers by Surface Catalytic Poisoning", *J. Phys. Chem. C,* Vol 11 , 2010, pp.19108–19115
2. M R. Louthan, Jr, "The Effect of Hydrogen on Metals", *Corrosion Mechanism*, F Mansfield, Editor Marcel Dekker Inc. NY 1987
3. P. Novak, R. Yuan,, B.P. Somerday, P. Sofronis, R.O. Ritchie, "A statistical, physical-based, micro-mechanical model of hydrogen-induced intergranular fracture in steel", *J. Mech. Phys. Solids*, Vol 58, 2010, pp 206-226
4. I.O. Shim, and J.G Byrne,. "A study of hydrogen embrittlement in 4340 steel I: Mechanical aspects", *Mat. Sci. Eng. A*, Vol 123,1990, pp 169-180
5. M.H. Sk, R.A. Overfelt, R.L. Haney and J.W. Fergus, "Hydrogen Embrittlement of 4340 Steel due to Condensation during Vaporized Hydrogen Peroxide Treatment", *Mat. Sci. & Eng A*, Vol 528, 2011, 3639-3645
6. A.W. Thompson, and I.M Bernstein, "Advances in Corrosion Science and Technology", *eds. R.W. Staehle and M.Fontana,* 7, 1980
7. C. J. McMahon Jr., "Hydrogen-induced intergranular fracture of steels", *Eng. Fract. Mech.* Vol 68, 2001, pp.773–*788*
8. A. Gourmelon, "Effect of hydrogen on the plastic deformation and fracture of iron", *Memoires Scientifiques de la Revue de Metallurgie,* Vol 72, (1975), 475-489
9. H.K Birnbaum, P. Sofronis, "Hydrogen Enhanced Localized Plasticity – a mechanism for hydrogen related Fracture", *Mat. Sci. Eng A*, Vol 176, pp. 191-202
10. M. Martin, A. Fenske, G. Liu, P. Sofronis, I. Robertson, "On the formation and nature of quasi-cleavage fracture surfaces in hydrogen embrittled steels, *Acta Mat.,* 59,1601 (2011)
11. Nagao, C. Smith, M. Dadfarnia, P. Sofronis, I. Robertson "The role of hydrogen in hydrogen embrittlement fracture of lath martensitic steel, *Acta Mat*. 60, 5182 (2012)
12. S.P. Lynch, "Interpreting hydrogen-induced fracture surfaces in terms of deformation processes: A new approach," *Scripta Mat*., 65, 851 (2011).
13. R.P.M. Proctor and H.W. Paxton., "T*he effect of prior austenite grain size* on *cracking susceptibility of AISI 4340 steel",Trans ASM*, Vol 62, 1969, pp. 989-999
14. E.Quadrini, " Effect of Prior austenitic grain size on the hydrogen embrittlement susceptibility of UNI 40NiCr Mo_7", *J. Materials Chemistry and Physics*, Vol 15, 1886, pp 155-165
15. J, F Lessar. and W.W Gerbarich, "Grain Size Effects in Hydrogen-Assisted Cracking", *Met. Trans*., Vol 4, 1976, pp 953- 960
16. S.K. Banerji, C.J. McMahon. Jr., and H.C. Feng, "Intergranular Fracture in 4340-type Steels: Effect of Impurities and Hydrogen", *Met Trans A*, Vol 9A, 1978, pp 237-247
17. Toh T, Baldwin W. M, " Ductility of Steel with Varying Concentrations of Hydrogen', Stress Concentration Cracking and Embittlement, ed, *W.D. Robertson, Wiley New York* (1956) 176-186

18. I.M. Robertson, J. Fenske, M. Martin, M. Briceno, M. Dadfarnia, P. Novak, D.C. Ahn, P. Sofronis, J.B. Liu, and D.D. Johnson, Understanding How Hydrogen Influences the Mechanical Properties of Iron and Steel, *2nd International Symposium of Steel Science 2009*, K. Higashida and N. Tsuji, Editors. 2009, The Iron and Steel Institute of Japan: Kyoto, Japan. p. 63-72
19. Brown, J.T. and Baldwin. W. M., **"**Hydrogen embrittlement of steels", *Jr.*, Journal of Metals (1954), 6(AIME Trans. 200), 298- 303
20. T. Michler, M. Lindner, U. Eberle, and J. Meusinger, Assessing hydrogen embrittlement in automotive hydrogen tanks., in Gaseous hydrogen embrittlement of materials in energy technologies Volume 1: The problem, its characterisation and effects on particular alloy classes, R.*P. Gangloff and B.P. Somerday, Editors, Woodhead Publishing.* (2012) p. 94-125.
21. N.A. Klapes and D. Vesley, "Vapor-Phase Hydrogen Peroxide as a Surface Decontaminant and Sterilant," *Appl.Environ. Microbiol*., 56 (1990) 503-506
22. A. L. Cummings, R.W. Childers and T.J. Mielnik, "Flow through vapor phase sterilization system, U.S. Patent No. 4,909,999, (1990)
23. B. Unger-Binczok, V. Kottke, C. Hertel and J. Rauschnabel, " The Influence of Humidity, Hydrogen Peroxide Concentration, and Condensation on the Inactivation of *Geobacillus stearothermophilus* Spores with Hydrogen Peroxide Vapor," *J. Pharm. Innov*., 3 (2008) 123-133.
24. D. Watling, C. Ryle, M. Parks and M. Christopher, " Theoretical Analysis of the Condensation of Hydrogen Peroxide Gas and Water Vapour as Used in Surface Decontamination," *PDA J. Pharm. Sci. Technol*., Vol 56. No. 6 (2002) 291-299.
25. J.V. Rogers, C.L. Sabourin, M.L. Taylor, K. Riggs, Y.W. Choi, W.R. Richter and D.C. Rudnicki, "Environmental Technology Verification Report - BIOQUELL Clarus C Hydrogen Peroxide Gas Generator," EPA/600/R-04/145, Washington, DC, March 2004
26. M.F. Verce, B. Jayaraman, T.D. Ford, A.J. Gadgil and T.M. Carlsen, "Minimizing Decomposition of Hydrogen Peroxide for Biological Decontamination of Galvanized Steel Ducting," *Environ. Sci. Technol*., Vol. 42, No. 15 5765-5771, (2008)
27. S. Chung, R. Kern, R. Koukol, J. Barengoltz and H. Cash, " Vapor hydrogen peroxide as alternative to dry heat microbial reduction," *Adv. Space Res*., 42 1150-1160. (2008)
28. W.F. Gale, H.S. Gale, J. Watson, "Field Evaluation of whole Airliner Decontamination Technologies for a Narrow-Body Aircraft," FAA Office of Aerospace Medicine, Washington, D.C., DOT/FAA/AM-08/2, 2008
29. R.M. Shaftstall, R.P. Garner, J. Bishop, L. Cameron-Landis, D.L. Eddington, G. Hau, S. Spera, T. Mielnik, J.A. Thomas, "Vaporized Hydrogen Peroxide (VHP) Decontamination of a Section of a Boeing 747 Cabin," FAA Office of Aerospace Medicine, Washington, D.C., DOT/FAA/AM-06/10, 2006.
30. W.F. Gale, H.S. Gale, J. Watson, "Field Evaluation of whole Airliner Decontamination Technologies - Wide-Body Aircraft with Dual Use Application for Railcars," FAA Office of Aerospace Medicine, Washington, D.C., DOT/FAA/AM-08/4, 2008
31. S.F. Chou, N.I. Sofyan, R.A. Overfelt, M.H. Sk, W.F. Gale, H.S. Gale, C.G. Shannon, J.W. Fergus, J. Watson, "Evaluation of the Effects of Hydrogen Peroxide on Common Aviation Structural Materials**,"** DOT/FAA/AM- 09/23, December 2009

32. W.F. Gale, N.I. Sofyan, H.S. Gale, M.H. Sk, S.F. Chou, J.W. Fergus and C.G. Shannon, "Effect of vapour phase hydrogen peroxide, as a decontaminant for civil aviation applications, on microstructure tensile properties and corrosion resistance of 2024 and 7075 age hardenable aluminum alloys and 304 austenitic stainless steel," *Materials Science and Technology*, Vol. 25, No. 1 (2009) 76-84
33. S.F. Chou, R.A. Overfelt, W.F. Gale, H.S. Gale, C.G. Shannon, F. Buschle-Diller and J. Watson, "Effects of Hydrogen Peroxide on Common Aviation Textiles," DOT/FAA/AM-09/16, August 2009
34. S.F. Chou, W.F. Gale, H.S. Gale, C.G. Shannon, G. Buschle-Diller, and N.I. Sofyan, "An Evaluation of Airliner Cabin Textile Materials after Hydrogen Peroxide Decontamination – Physical and Structural Changes and their Influence on Mechanical Properties," *Material Science and Technology*, Vol. 26, No. 1 (2010) 66-80
35. M.D. Brickhouse, T. Lalain, P.W. Bartram, M. Hall, Z. Hess, L. Reiff, B. Mantooth, Z. Zander, D. Stark, P. Humphreys, B. Williams, S. Ryan, B. Martin, "Effects of Vapor-based Decontamination Systems on Selected Building Interior Materials: Vaporized Hydrogen Peroxide," EPA/600/R-08-074, Washington, DC, July 2008
36. Thompson, A.W., and Bernstein, I. M., Advances in Corrosion Science and Technology, eds. R. W. Staehle and M. Fontana, (1980) 7
37. R.J.H. Wanhill , S.A. Barter, S.P. Lynch and D.R. Gerrard, Corrosion Fatigue and Environmentally Assisted Cracking in Aging Military Vehicles, RTO-AG-AVT-140, 2011
38. Troiano A. R., "The Role of Hydrogen and Other Interstitials in the Mechanical Behavior of Metals", Trans ASM , Vol 52 (1960), p. 55
39. R. P. Frohnberg, W. J. Barnett, and A. R. Troiano, "Delayed failure and hydrogen embrittlement in *steel"Trans. AMS* 47 (1955) 892-923
40. Sims. C.E., Moore, G.A, Williams, D.W, "The Effect of Hydrogen on the Ductility of Cast Steel", Am. Inst. Mining Met. Engrs. Vol. 176 (1948) p. 260-278
41. S. Pillot and L. Coudreuse, Hydrogen-induced disbonding and embrittlement of steels used in petrochemical refining, in Gaseous hydrogen embrittlement of materials in energy technologies. Volume 1: The problem, its characterisation and effects on particular alloy classes, *R.P. Gangloff and B.P. Somerday, Editors. 2012, Woodhead Publishing*. p. 51-93.
42. D.P. Abraham and C.J. Altstetter, Effect of hydrogen on the yield and flow stress of an austenitic stainless steel. *Metallurgical and Materials Transactions A: Physical Metallurgy and Materials Science*, vol 26 A (1995) p. 2849-2858
43. J.P. Hirth, Effects of hydrogen on the properties of iron and steel. *Metallurgical Transactions A (Physical Metallurgy and Materials Science), Vol* 11A(Copyright 1980, IEE) (1980). p. 861-90.
44. R. Latanision and H. Opperhauser, The intergranular embrittlement of nickel by hydrogen: The effect of grain boundary segregation. *Metallurgical and Materials Transactions B*, Vol **5** (1974) p. 483-492
45. H.K. Birnbaum, Hydrogen effects on deformation - relation between dislocation behavior and the macroscopic stress-strain behavior. *Scripta Metallurgica et Materialia*, Vol **31(**1994) p. 149-153.

46. P.S. Lam, R.L. Sindelar, A.J. Duncan, and T.M. Adams, Literature survey of gaseous hydrogen effects on the mechanical properties of carbon and low alloy steels. *Journal of Pressure Vessel Technology, Transactions of the ASME,* Vol 131 **(**2009). p. 0414081-04140814.
47. A.W. Loginow and E.H. Phelps, Steels for seamless hydrogen pressure vessels. *Corrosion,* Vol 31 (1975) p. 404-412.
48. W.W. Gerberich and Y.T. Chen, Hydrogen-Controlled Cracking - An Approach to Threshold Stress Intensity. *Metallurgical Transactions A (Physical Metallurgy and Materials Science),* **6 A** (1975). p. 271-278
49. Lynch. S.P. "A Fractographic Study of Gaseous Hydrogen Embrittlement and Liquid-Metal Embrittlement in a Tempered-Martensitic Steel", Acta Metall, Vol 32 (1984) 79-90
50. Eliaz. N, Shachar. A, Tal. B, Eliezer. D, "Characteristics of Hydrogen Embrittlement, Stress Corrosion Cracking and Tempered Martensitic Embrittlement in High Strength Steel", *Engineering Failure Analysis* , Vol 9 (2002) 167-184
51 Qiao. L, Mao. X, " Hydrogen-Induced Cleavage Fracture of Fe_3Al-Based Intermetallics", *Metallurgical and Materials Transactions*, Vol 27 A (1996) 3949-3956
52. Kikuta, Y.; Araki, T.; Kuroda, T., "A fractographic approach to failure analysis on hydrogen assisted cracking in high strength steel and its weld", *International Symposium of the Japan Welding Society, [Proceedings]* (1978), 3(Criter. Prev. Serv. Failure Welded Struct.), 257-62
53. Beachem. C D, "A new Model for Hydrogen-Assisted Cracking (Hydrogen embrittlement)", Metallurgical Transactions Vol 3A (1972) 437-451
54. http://www.tech.plym.ac.uk/sme/interactive_resources/tutorials/failureanalysis/Fractography Fractography_Resource5.htm
55. C. A. Zapffe," Research Shows How Pickling Causes Brittleness in Stainless Steels", Materials and Methods 32 (1950) 58
56. D.G. Westlake, "A Generalized Model for H Embrittlement", *Trans ASM,* 62 (1969) 1000-1006
57. N. J. Petch and P. Stables, "Delayed Fracture of Metals Under Static Load", *Nature*, 169 (1952) 842-843
58. R.A. Oriani, "A Mechanistic Theory of Hydrogen Embrittlement of Steels", Ber. Bunsenges Phys. Chem., 76 (1972) 848-857
59. H. H. Johnson, J. G. Morlet, and A. R. Troiano, "*Hydrogen crack initiation, and delayed* failure m steel", Trans. Met. Soc. AIME, 212 (1958) 528-536
60. C.D. Beachem, "A New Model for Hydrogen Assisted Cracking (Hydrogen Embrittlement)", Metall. Trans., 3A (1972) 437-451
61. Yu Jagodzinski, H Hänninen, O Tarasenko, S Smuk, "Interaction of hydrogen with dislocation pile-ups and hydrogen induced softening of pure iron", Scripta Materialia, 43(2000) 245-251
62. Robertson, I.M., "The effect of hydrogen on dislocation dynamics",. Eng. Fract. Mech. 68 (2001) 671–692.
63. Shih D S, Robertson I M , Bimbaum H K, " Hydrogen embrittlement in α-Ti; in situ TEM studies", Acta Metall, 36 (1988)2639 - 2661
64. Ferreira P J, Robertson I M, Birnbaum H K, "Hydrogen effects on the interaction between dislocations", Acta Mater, 46 (1998) 1749-1757
65. P. Sofronis and H.K.Birnbaum, "Mechanics of the hydrogen-dislocation-impurity interactions. I: Increasing shear modulus", J. Mech. Phys. Solid 43 (1995) 49–90

66. Quadrini. E., " Effect of Prior austenitic grain size on the hydrogen embrittlement susceptibility of UNI 40NiCr Mo_7", J. Materials Chemistry and Physics, 15 (1886) 155-165
67. Banerji S. K., Mcmahon, C. J. Jr. and Feng H.C. " Intergranular Fracture in 4340-type Steels: Effects of Impurities and Hydrogen, *Metallurgical Transactions A* vol. 9 (1978). p. 237 - 247
68. Klingler, L. J.; Barnett, W. J.; Frohmberg, R. P.; Troiano, A. R. "The embrittlement of alloy steel at high temperatures**",** *Transactions of the American Society for Metals* , Vol. 46 (1954), pp 1557
69. Lement, B.S, Averbach, B.L., Cohen. M., **"**Microstructural changes on tempering iron-carbon alloys**,** *",Transactions of the American Society for Metals* , vol 46 (1954), pp. 851
70. Schrader, H.; Wiester, H. J.; Siepmann, H. "Embrittlement of hardened steels in tempering at 250-400°, Archiv fuer das Eisenhuettenwesen 21, (1950), pp. 21-31
71. Capus, J. M.; Mayer, G. "The mechanical properties of some tempered alloy martensites", Journal of the Iron and Steel Institute, London 196(Pt. 2) (1960), , pp. 149-58
72. Kula, E. B.; Anctil, A. A., "Tempered martensite embrittlement and fracture toughness in SAE 4340 steel**"** , Journal of Materials 4(4), (1969), pp. 817-41
73. Rellick, J. R.; McMahon, C. J., Jr. , "Intergranular embrittlement of iron-carbon alloys by impurities", Metallurgical Transactions, 5(11), (1974), pp. 2439-50
74. I.E. King, R.F. Smith *and* J.F. Knott, "Tempering of a Plain Carbon, Martensitic Steel", *Fracture 1977, ICF4,. Waterloo, Canada, Vol. 2, (1977) , p. 279*
75. Thomas, G, "Retained austenite and tempered martensite embrittlement", Metallurgical Transactions A: Physical Metallurgy and Materials Science (1978), 9A(3), 439-50
76. Horn, R. M.; Ritchie, Robert O. , "Mechanisms of tempered martensite embrittlement in low alloy steels", From Metallurgical Transactions A: Physical Metallurgy and Materials Science (1978), 9A(8), 1039-53
77. Krauss, G, Materkowski, J. P.; "Tempered martensite embrittlement in SAE 4340 steel", Metallurgical Transactions A: Physical Metallurgy and Materials Science 10A(11), (1979), pp. 1643-51.
78. Cotterill P, "Hydrogen embrittlement in metals", *Prog. Mat. ScL.*, 9 (1961) 205-301
79. Troiano. A.R, "The role of hydrogen and other interstitials in the mechanical behavior of metals", *Trans ASM*, 52 (1960) 54-80
80. Elsea, E.R., Fletcher M.N., "Hydrogen Induced Delayed Brittle *Failures of High Strength Steels" NASA Tech. Report* (1967)
81. Zackay, V.F, *E.R. Parker, W.E. Wood* "Influence of some microstructural features on the fracture toughness of high strength steels" *Proc. 3rd Int, Conf. on Strength of Metals and Alloys, England* (1973) 175-188
82. Wood, E.W.,"Effect of Heat Treatment on the *Fracture* Toughness of Low Alloy. Steels", *Eng. Frac. Mech.* 7 (1975) 219-234
83. Lai G L, Wood W E, Clark R A, Zackay VF, Parker E R , "Effect of austenitizing temperature on the microstructure and mechanical properties of as-quenched 4340 steel *Metallurgical Transactions* Vol 5 (1974), 1663-1670
84. Parker, E.R., Zackay, V.F., "Enhancement of fracture toughness in high strength steel by microstructural control", *Eng., Frac. Mech.*, 5 (1973) 163-165
85. S. Morito, H. Yoshida, T. Maki and X. Huang, " Effects of Block Size on the Strength of Lath Martensite in Low Carbon Steel", Materials Science and Engineering A, Vol 438-440 (2006), pp. 237-240

86. Morris J. W., Kinney C, Pytlewski K, Adachi Y, " Microstructure and Cleavage in Lath Martensitic Steels", Sci. Technol Adv. Mater. Vol 14 (2013), pp 014208
87. Park S. G, Lee K H, Kim M C, Lee B S, " Effects of Boundary Characteristics on Resistance to Temper Embrittlement and Segregation Behavior of Ni-Cr-Mo Low Alloy Steel", Materials Science and Engineering A , Vol 561 (2013), pp. 277-284
88. Nagao A, Smith C. D, Dadfarnia M, Sofronis P, Robertson I. M., " The Role of Hydrogen in Hydrogen Embrittlement Fracture on Lath martensitic Steel", Acta Materialia, Vol 60 (2012) pp. 5182-5189
89. *Maki T., Tsuzaki K.* and *Tamura* I., "The Morphology of Microstructure Composed of Lath Martensites in Steels," *Trans. ISIJ*, Vol 20 (1980), pp. 207-214
90. Swarr, T; Krauss, G, , "Effect of structure on the deformation of as-quenched and tempered martensite in an iron-0.2% carbon alloy " , Metallurgical Transactions A: Physical Metallurgy and Materials Science 7A(1) (1976), 41-48
91. ASTM F 519-06, Standard Test Method for Mechanical Hydrogen Embrittlement Evaluation of Plating Coating Processes and Service Environments, ASTM International, Philadelphia, PA, 2006
92. ASTM E8-00b, Standard Test Methods for Tension Testing of Metallic Materials, ASTM International, Philadelphia, PA, 2006
93. ASTM E112-96, "Standard Test Methods for Determining Average Grain Size", *ASTM International*, Philadelphia, PA, (1996)
94. C.E. Huckaba, F.G. Keyes, "The *accuracy of estimation of hydrogen* peroxide by potassium permangnate titration" *J. Am. Chem. Soc.* 70 (1948) 1640–1644
95. M.W. Chase Jr., , "Thermo-chemical Table, Journal of Physical and Chemical Reference Data", *NIST-JANAF*, Monograph No. 9, 4th ed., Part 2 (1998) 1330
96. J. C. M. Li, R. A. Oriani and L. S. Darken "The Thermodynamics of Stressed Solids" *Z. Physik. Chem. Neue Folge* Vol 49, (1966) 271-290

Appendix A : Quantitative estimation of the fracture modes using SEM image

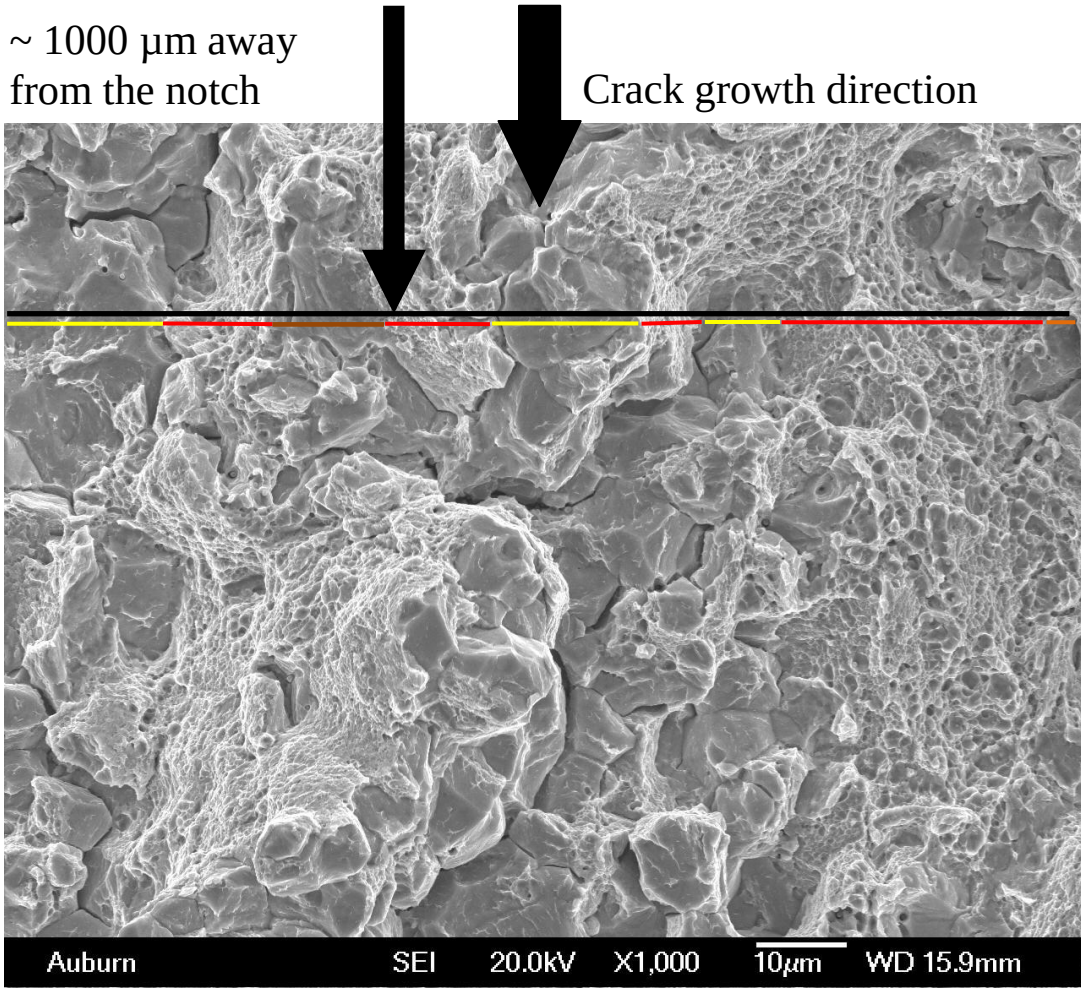

Fig. A-1. Demonstration of the quantitative estimation of various fracture features for 20 min hydrogenated 10 µm 52 HRC sample loaded at 0.01 mm/min. The yellow lines represent regions of intergranular fracture; red lines represent regions of microvoid coalescence and the brown lines represents regions of flat surfaces (unsure if they are intergranular or quasi) on the entire image length at a distance ~1000µm from the notch. Sum of each set of colored lines over the entire length (indicated by the black line) determines the fraction of each.

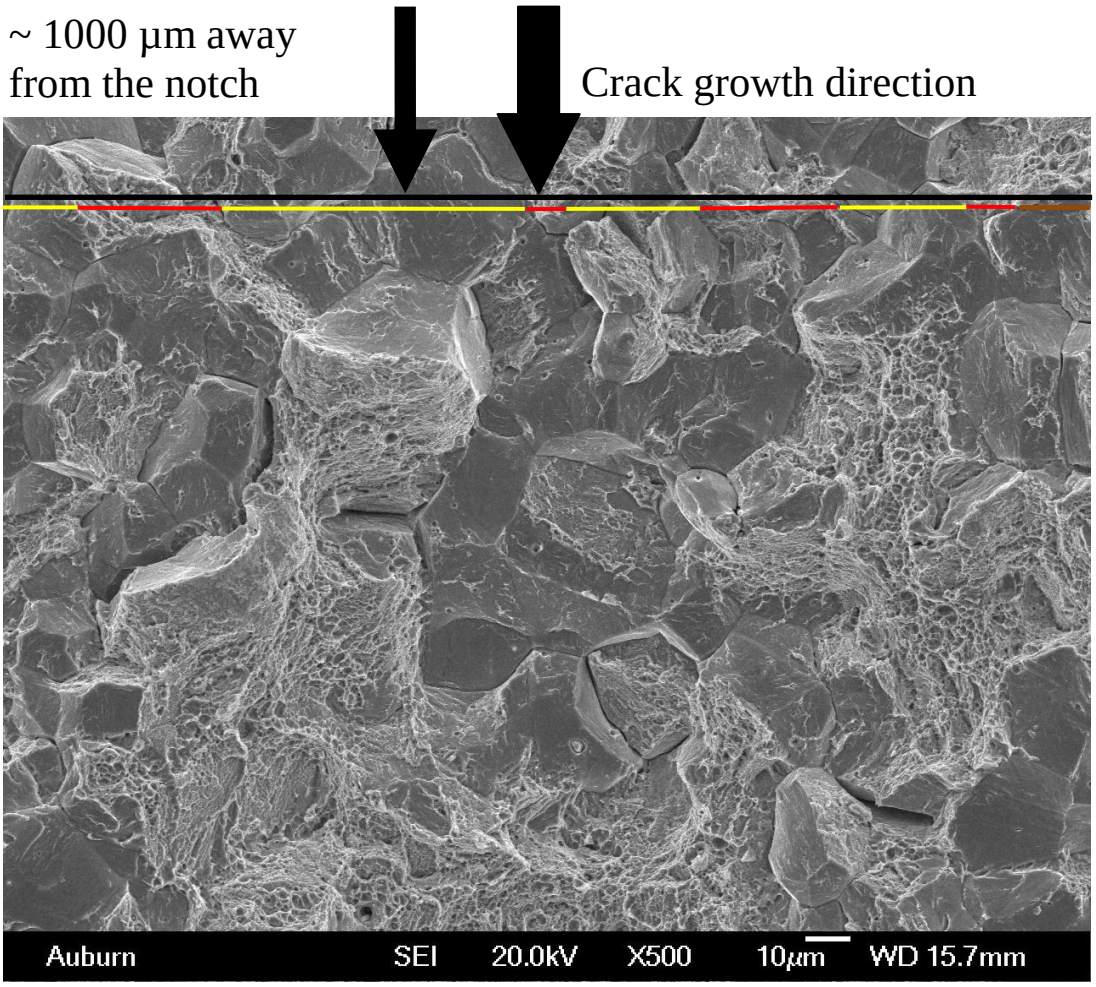

Fig. A-2. Demonstration of the quantitative estimation of various fracture features for 20 min hydrogenated 40 µm 50 HRC sample loaded at 0.01 mm/min. The yellow lines represent regions of intergranular fracture; red lines represent regions of microvoid coalescence and the brown lines represents regions of flat surfaces (unsure if they are intergranular or quasi) on the entire image length at a distance ~1000µm from the notch. Sum of each set of colored lines over the entire length (indicated by the black line) determines the fraction of each.

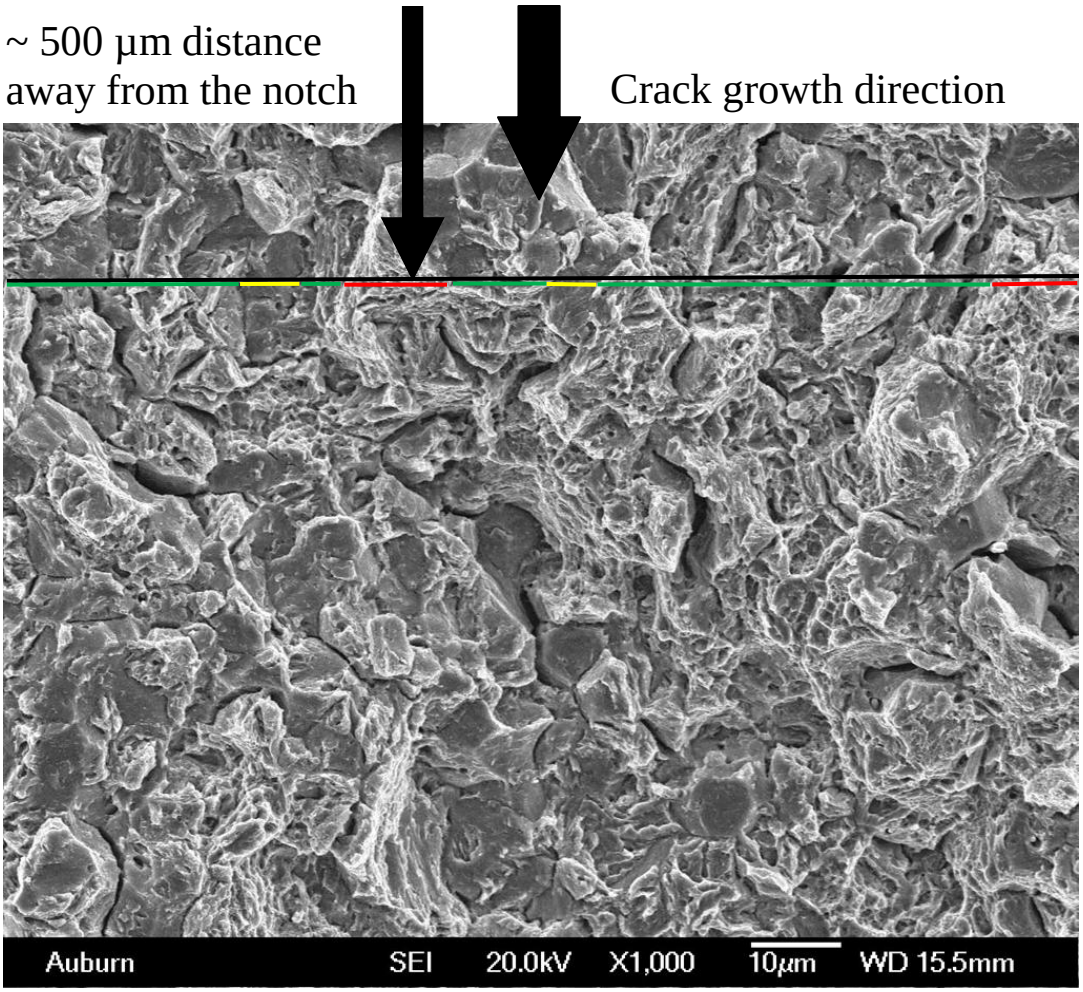

Fig. A-3. Demonstration of the quantitative estimation of various fracture features for 40 min hydrogenated 10 µm 45 HRC sample loaded at 0.01 mm/min. The yellow lines represent regions of intergranular fracture; red lines represent regions of microvoid coalescence and the green lines represent regions of quasi-cleavage surfaces and its associated smooth facets on the entire image length at a distance ~500 µm from the notch. Sum of each set of colored lines over the entire length (indicated by the black line) determines the fraction of each.

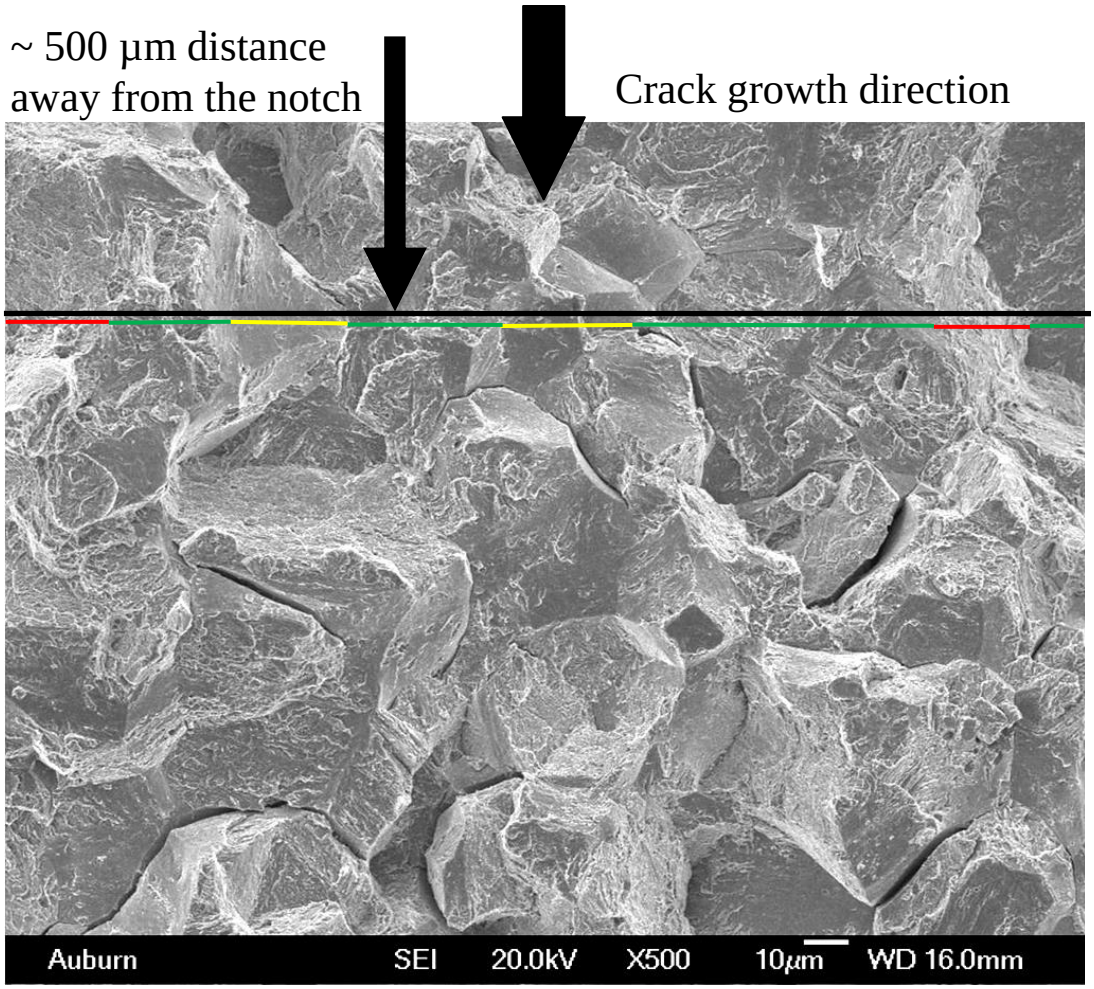

Fig. A-4. Demonstration of the quantitative estimation of various fracture features for 40 min hydrogenated 40 µm 43 HRC sample loaded at 0.01 mm/min. The yellow lines represent regions of intergranular fracture; red lines represent regions of microvoid coalescence and the green lines represent regions of quasi-cleavage surfaces and its associated smooth facets on the entire image length at a distance ~500 µm from the notch. Sum of each set of colored lines over the entire length (indicated by the black line) determines the fraction of each.

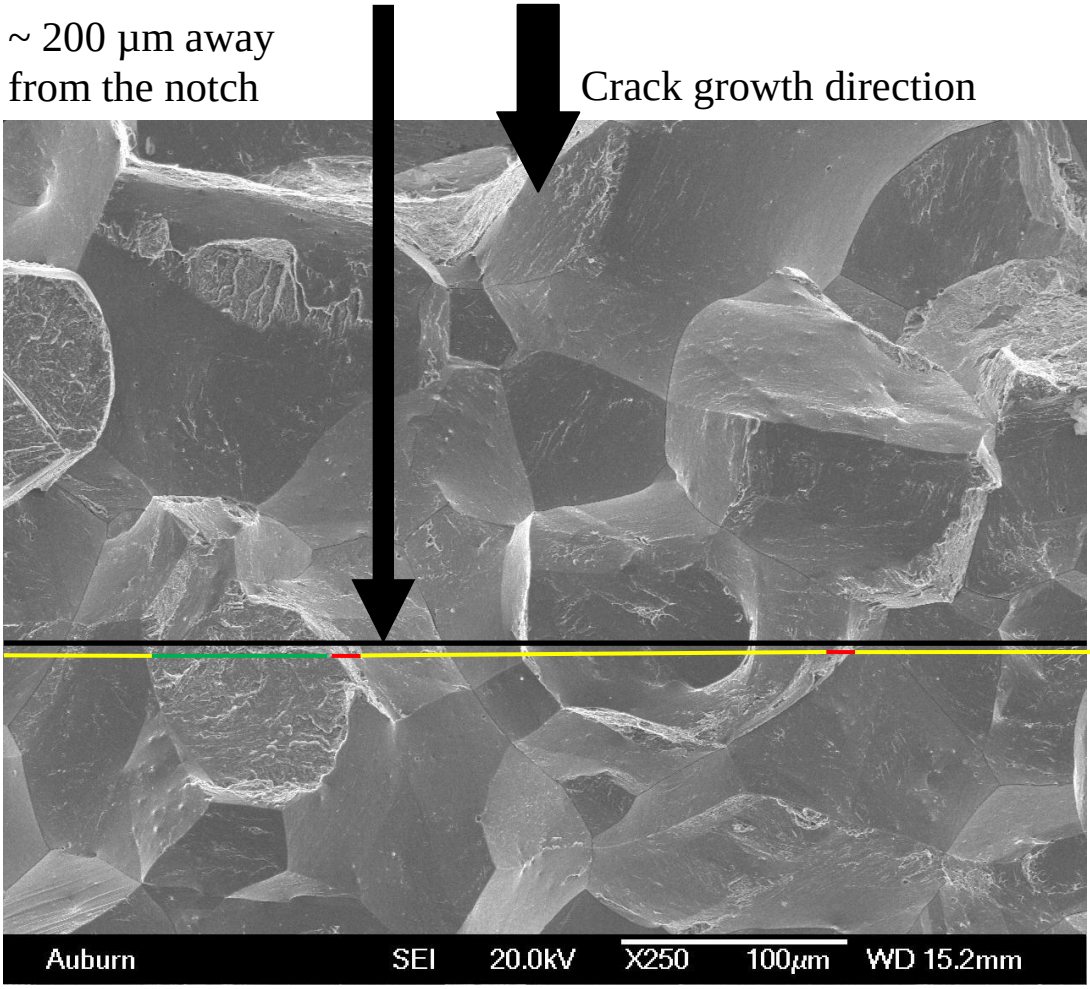

Fig. A-5. Demonstration of the quantitative estimation of various fracture features for 10 min hydrogenated 100 µm 48 HRC sample loaded at 0.01 mm/min. The yellow lines represent regions of intergranular fracture; red lines represent regions of microvoid coalescence and the green lines represent regions of quasi-cleavage surfaces on the entire image length at a distance ~200 µm from the notch. Sum of each set of colored lines over the entire length (indicated by the black line) determines the fraction of each.

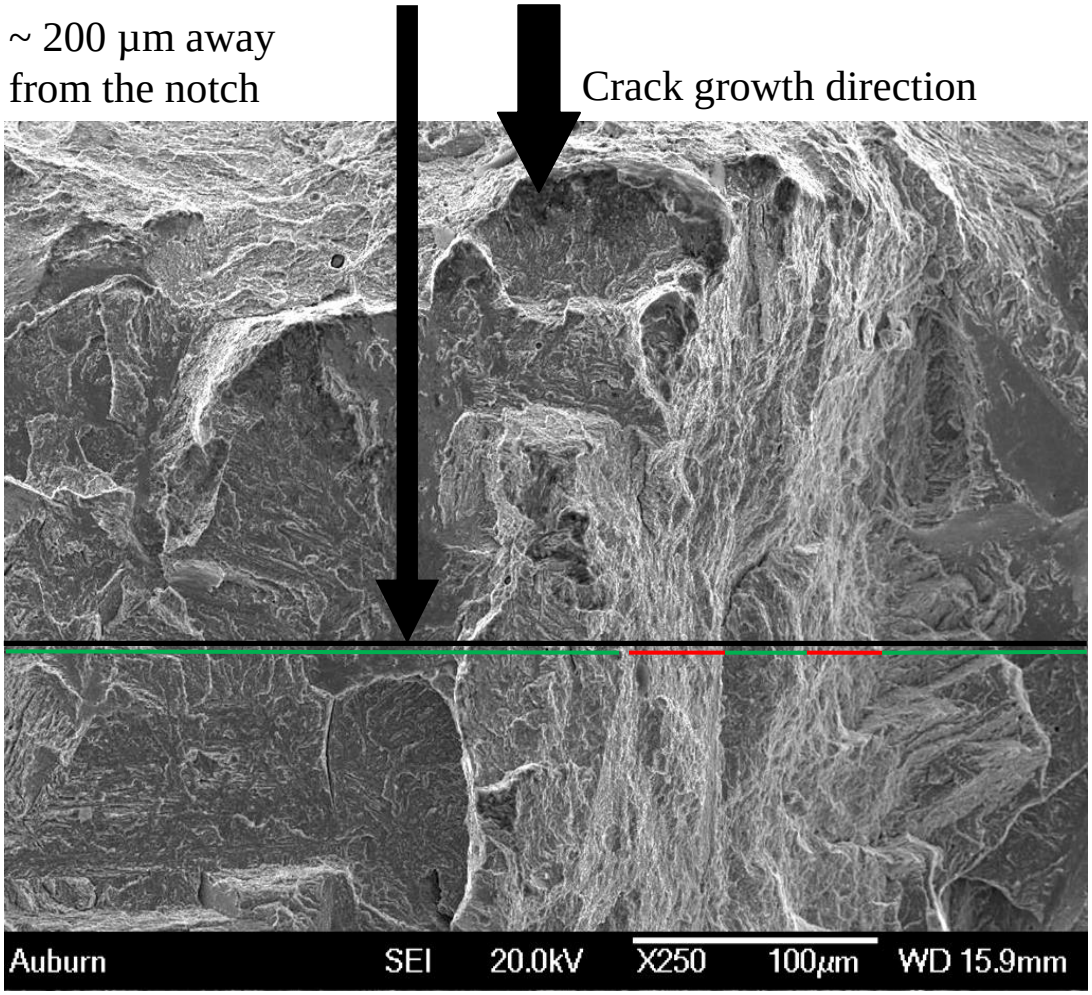

Fig. A-6. Demonstration of the quantitative estimation of various fracture features for 10 min hydrogenated 100 µm 41 HRC sample loaded at 0.01 mm/min. The red lines represent regions of microvoid coalescence and the green lines represent regions of quasi-cleavage surfaces on the entire image length at a distance ~200 µm from the notch. Sum of each set of colored lines over the entire length (indicated by the black line) determines the fraction of each.

Appendix B: Tensile Test Results

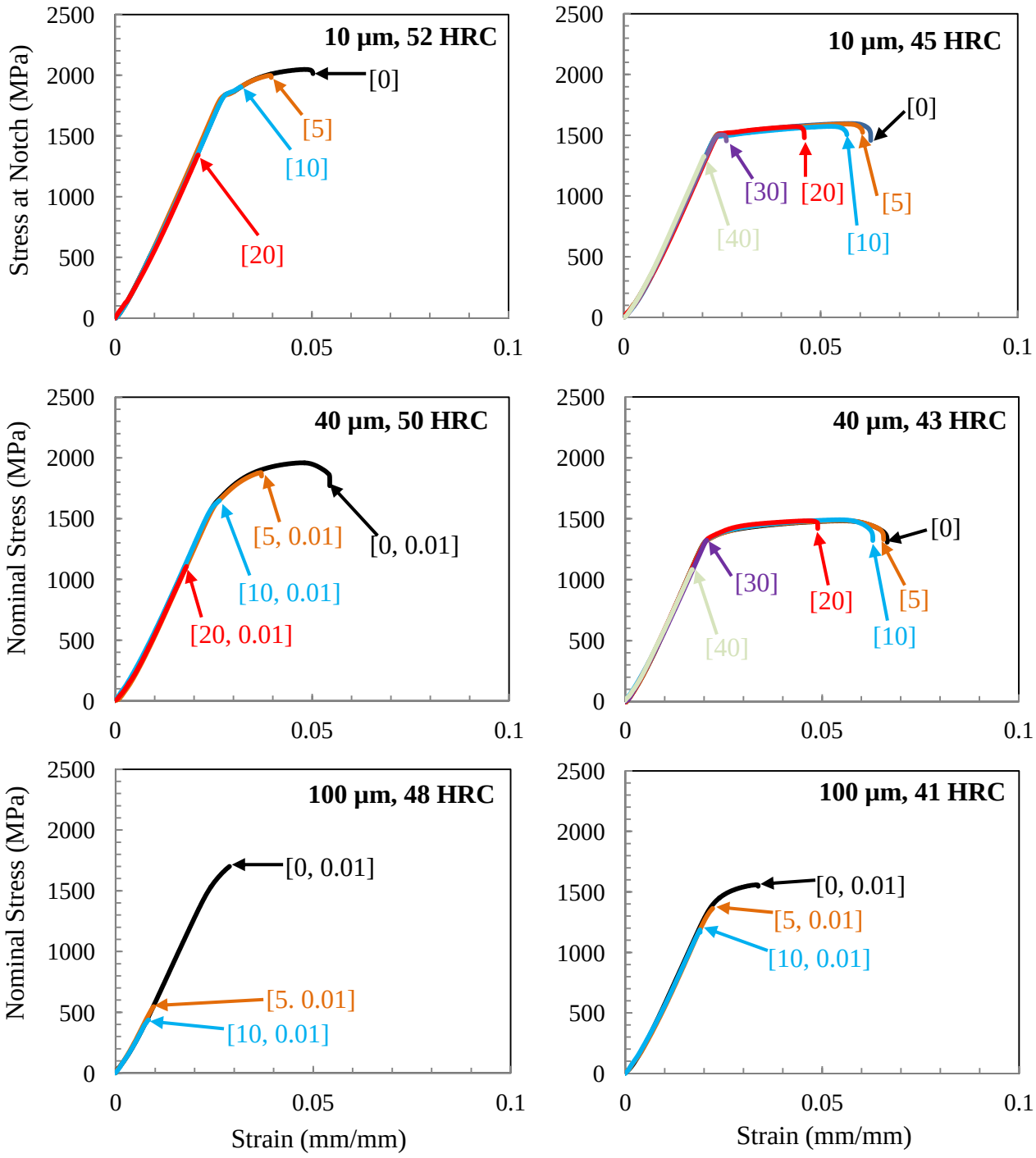

Fig. B-1 Representative tensile test result. 10-100 µm harder and softer samples hydrogenated for 0-40 min and loaded at a cross head speed of 0.01mm/min.

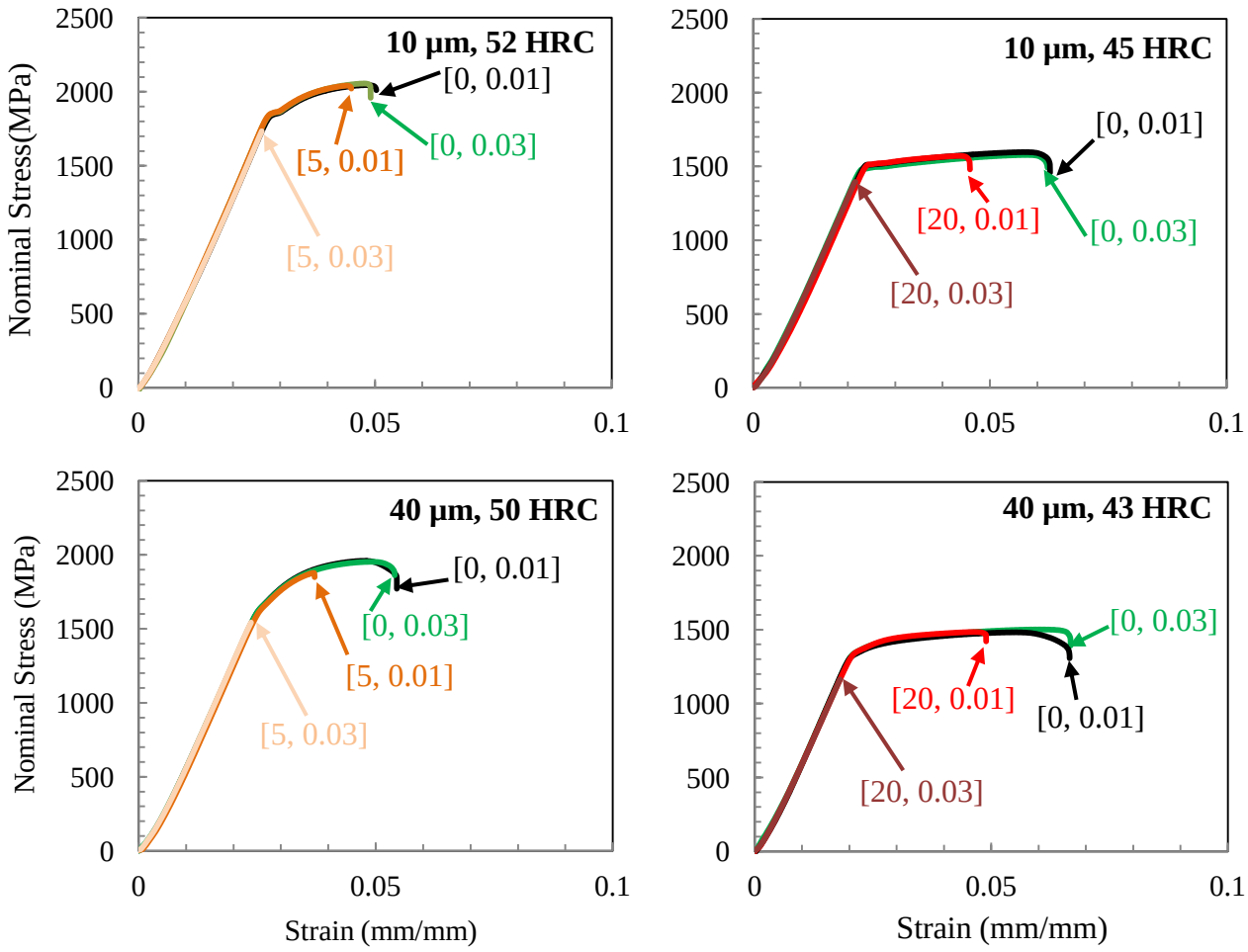

Fig. B-2 Representative comparison of the Tensile results at two different strain rates for 10-40 µm harder (charged for 0 and 5 min) and softer (charged for 0, 10 and 20 min) and loaded at a cross head speeds of 0.01mm/min and 0.03 mm/min. 100 µm samples were not subjected to loading at 0.03 mm/min.

Appendix C: Various Appearances of the Quasi-Cleavage and Mixed Mode Quasi Cleavage

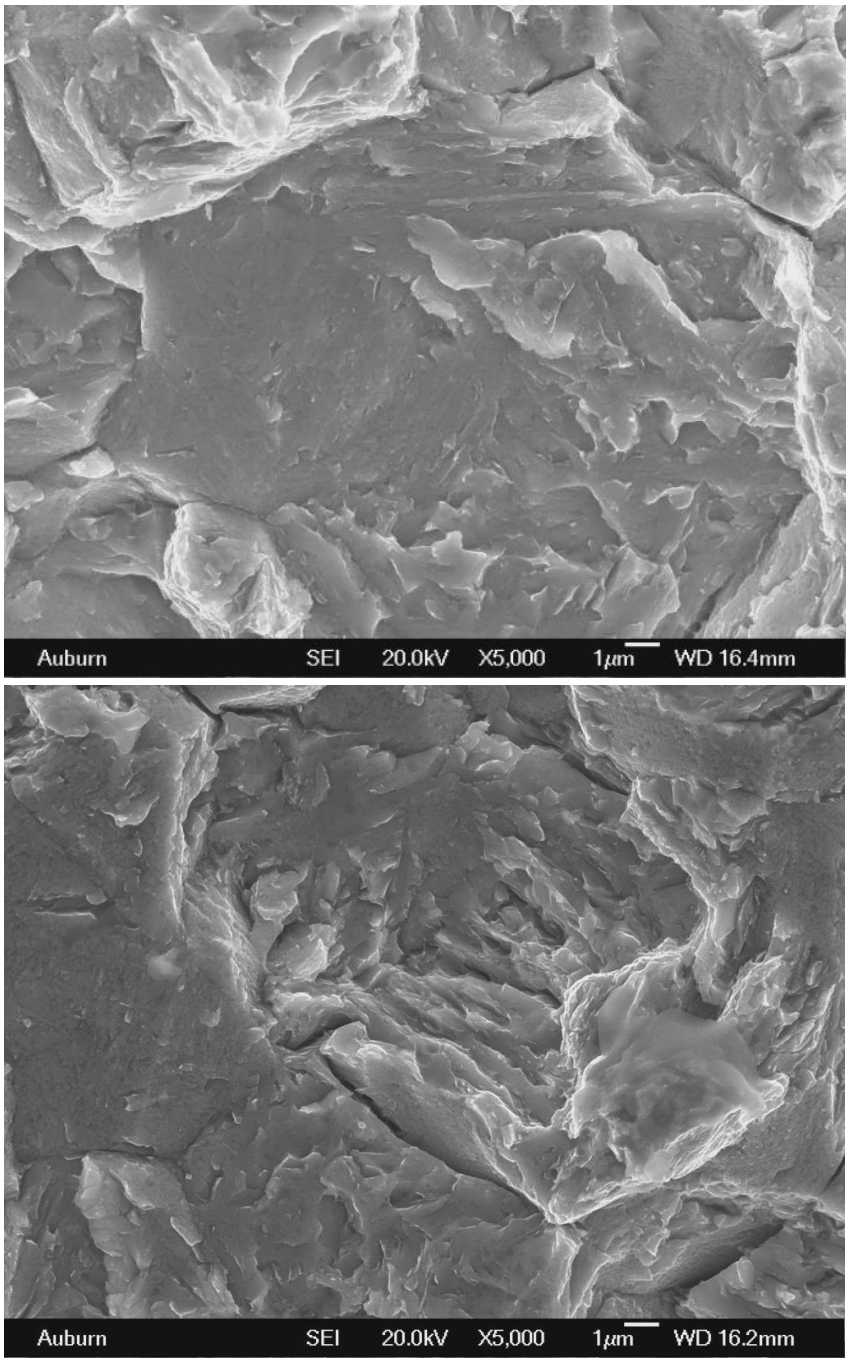

Fig. C-1 Typical quasi-cleavage features and smooth surfaces associated to it for 10 µm 45 HRC 40 min hydrogenated sample. The associated smooth surfaces are broken parts along the martensite lath boundaries. CHS : 0.01 mm/min

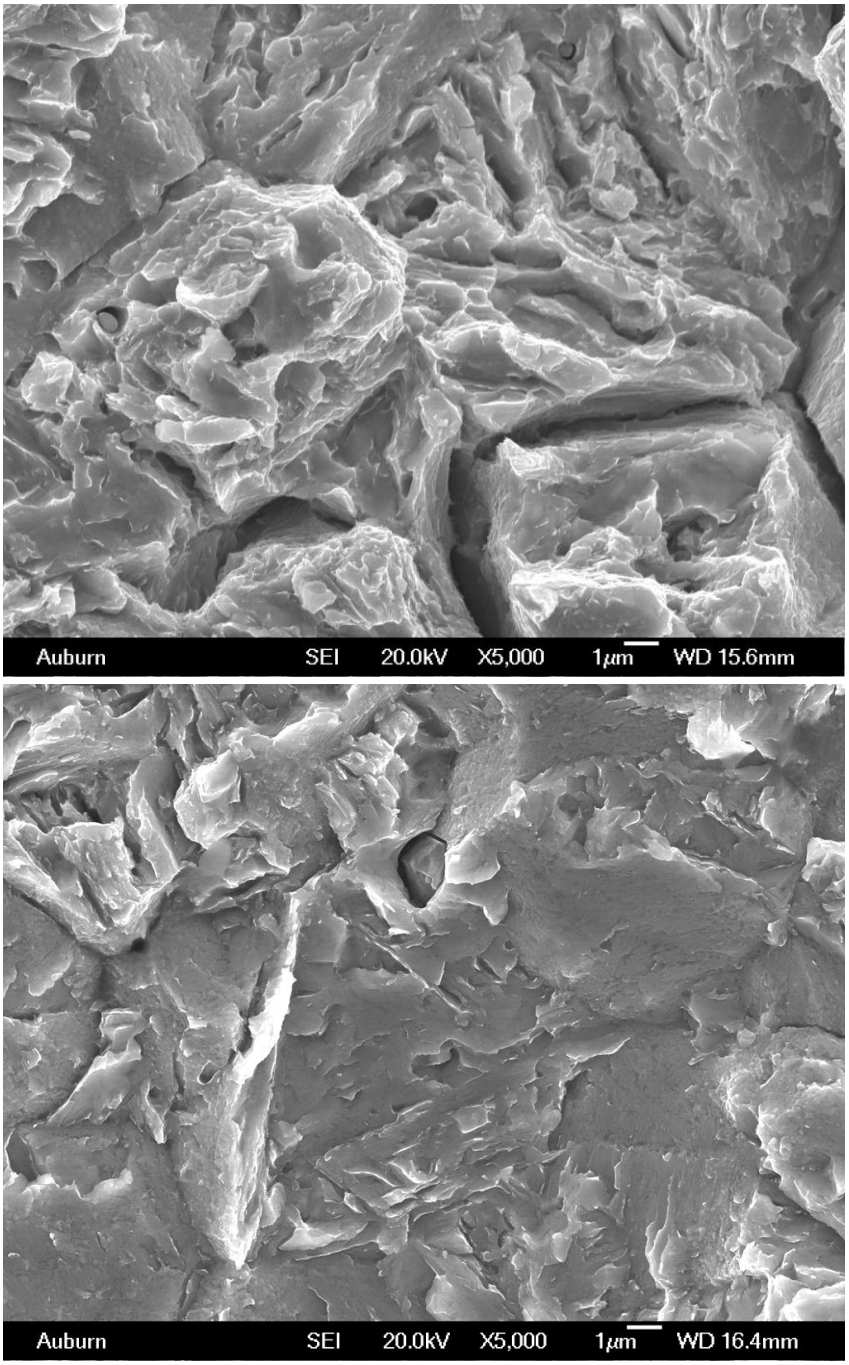

Fig. C-2 Typical quasi-cleavage features and smooth surfaces associated to it for 10 µm 45 HRC 40 min hydrogenated sample. The associated smooth surfaces are broken parts along the martensite lath boundaries. CHS : 0.01 mm/min.

.

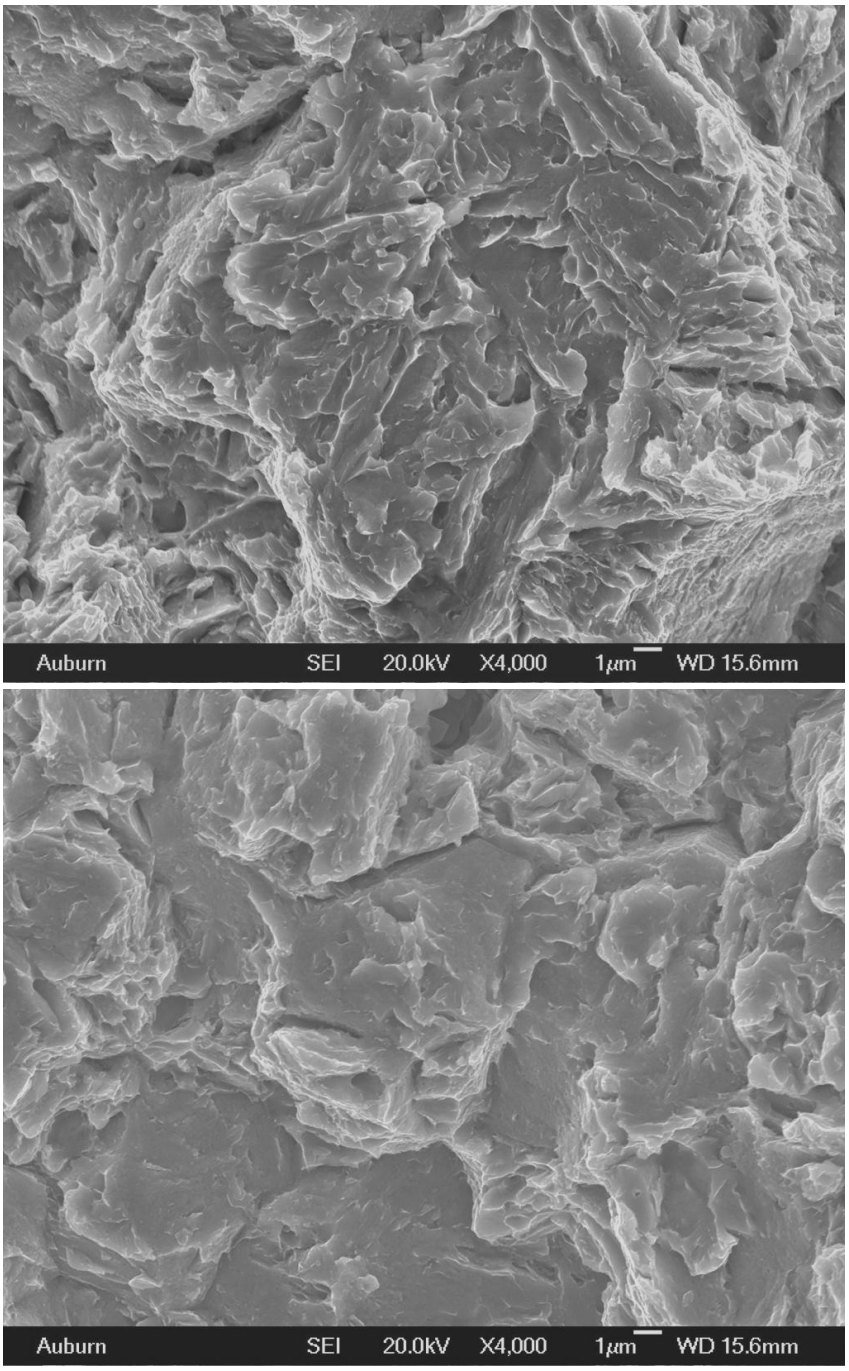

Fig. C-3 Typical quasi-cleavage features and smooth surfaces associated to it for 10 µm 45 HRC 20 min hydrogenated sample. The associated smooth surfaces are broken parts along the martensite lath boundaries.CHS : 0.01 mm/min

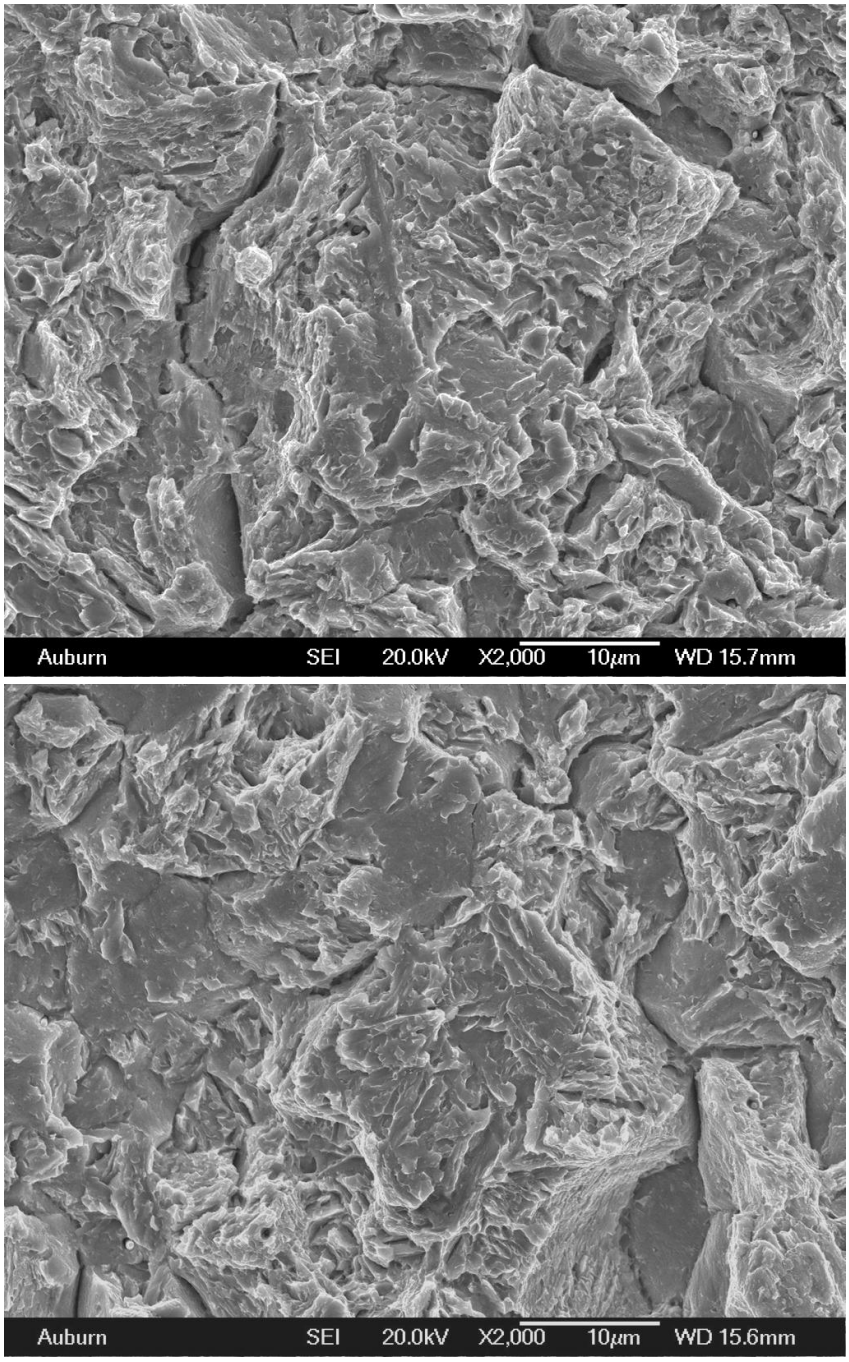

Fig. C-4 Typical quasi-cleavage features and smooth surfaces associated to it for 10 µm 45 HRC 20 min hydrogenated sample. The associated smooth surfaces are broken parts along the martensite lath boundaries.CHS : 0.01 mm/min

.

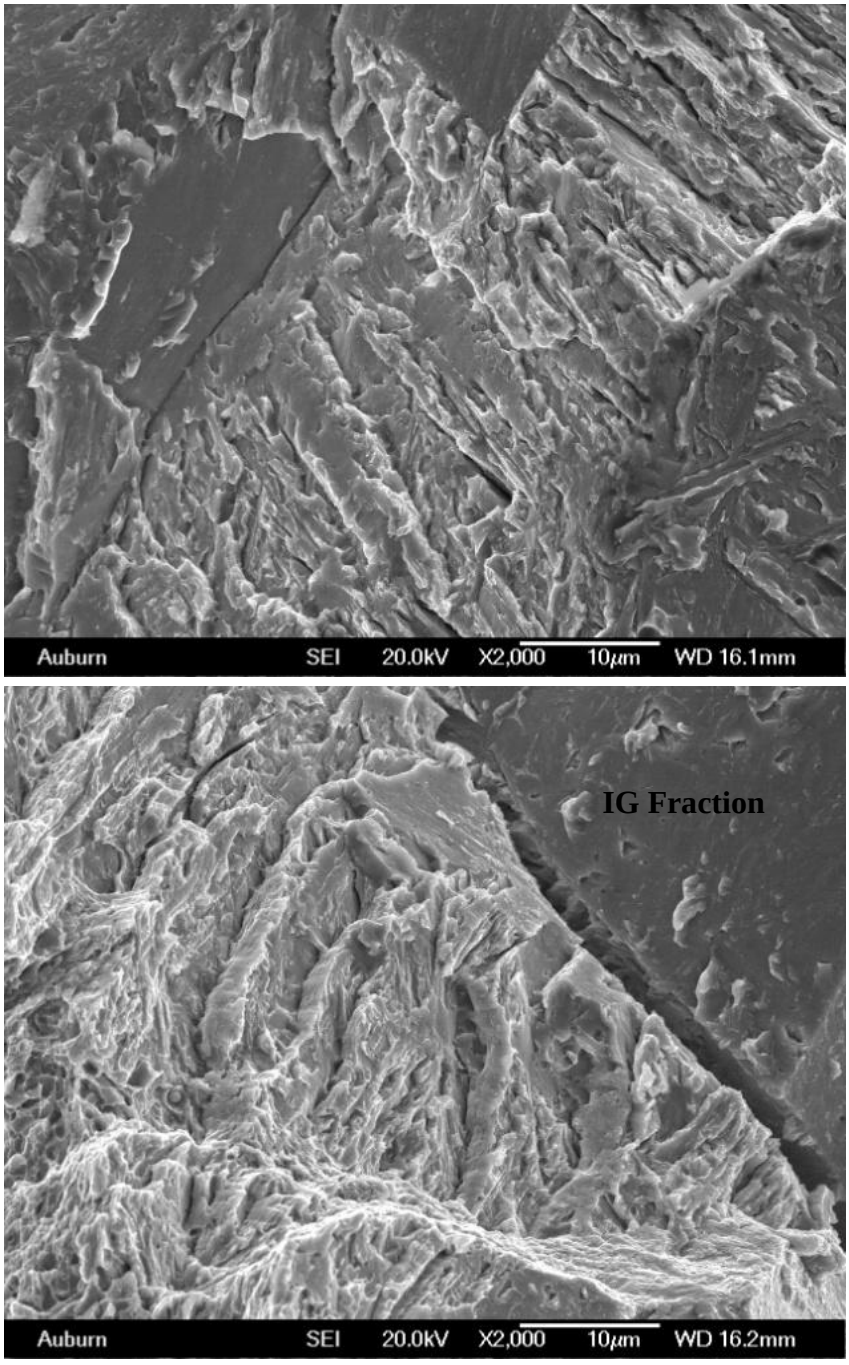

Fig. C-5 Typical quasi-cleavage features for 40 μm 43 HRC 40 min hydrogenated sample. CHS : 0.01 mm/min

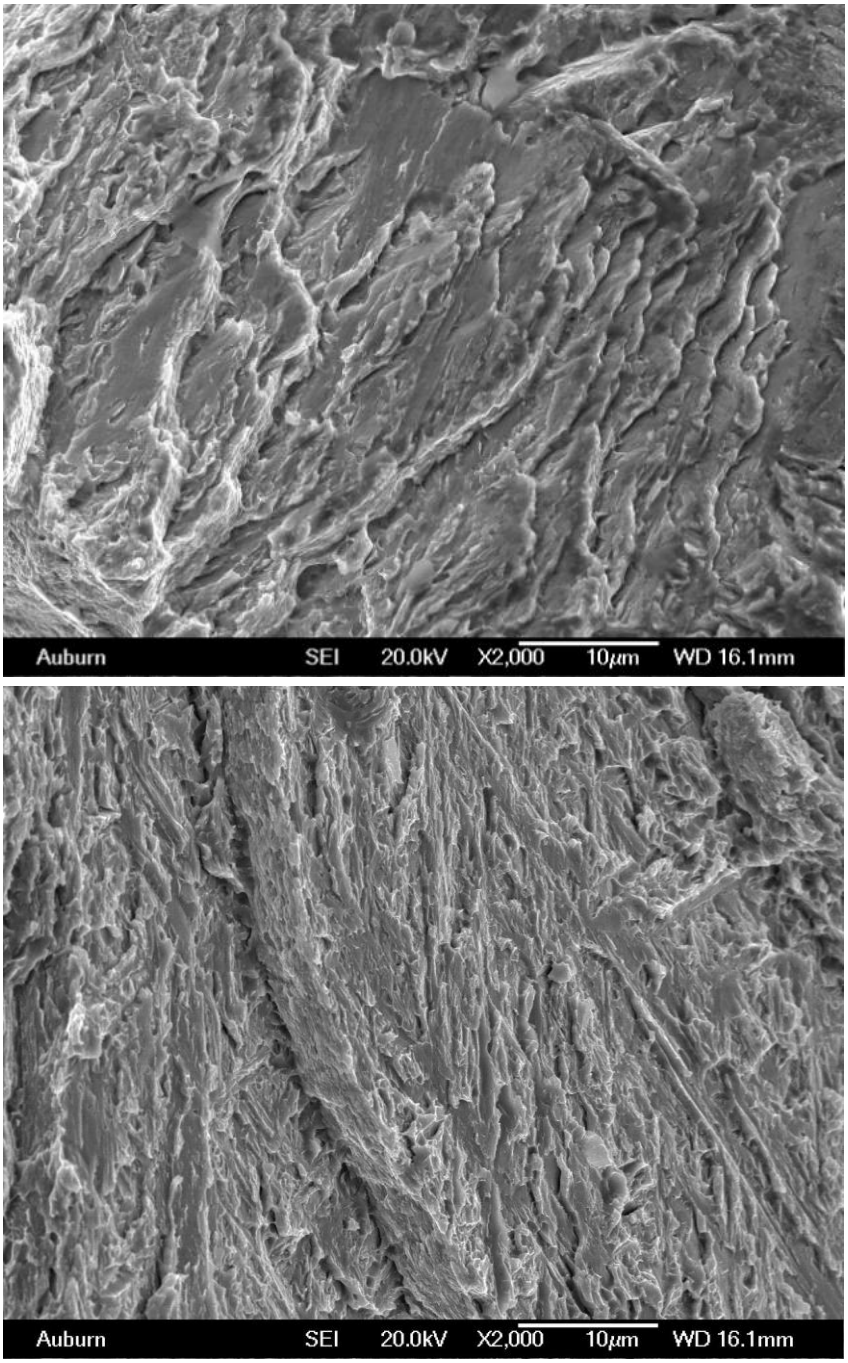

Fig. C-6 Typical quasi-cleavage features for 40 μm 43 HRC 40 min hydrogenated sample. CHS : 0.01 mm/min

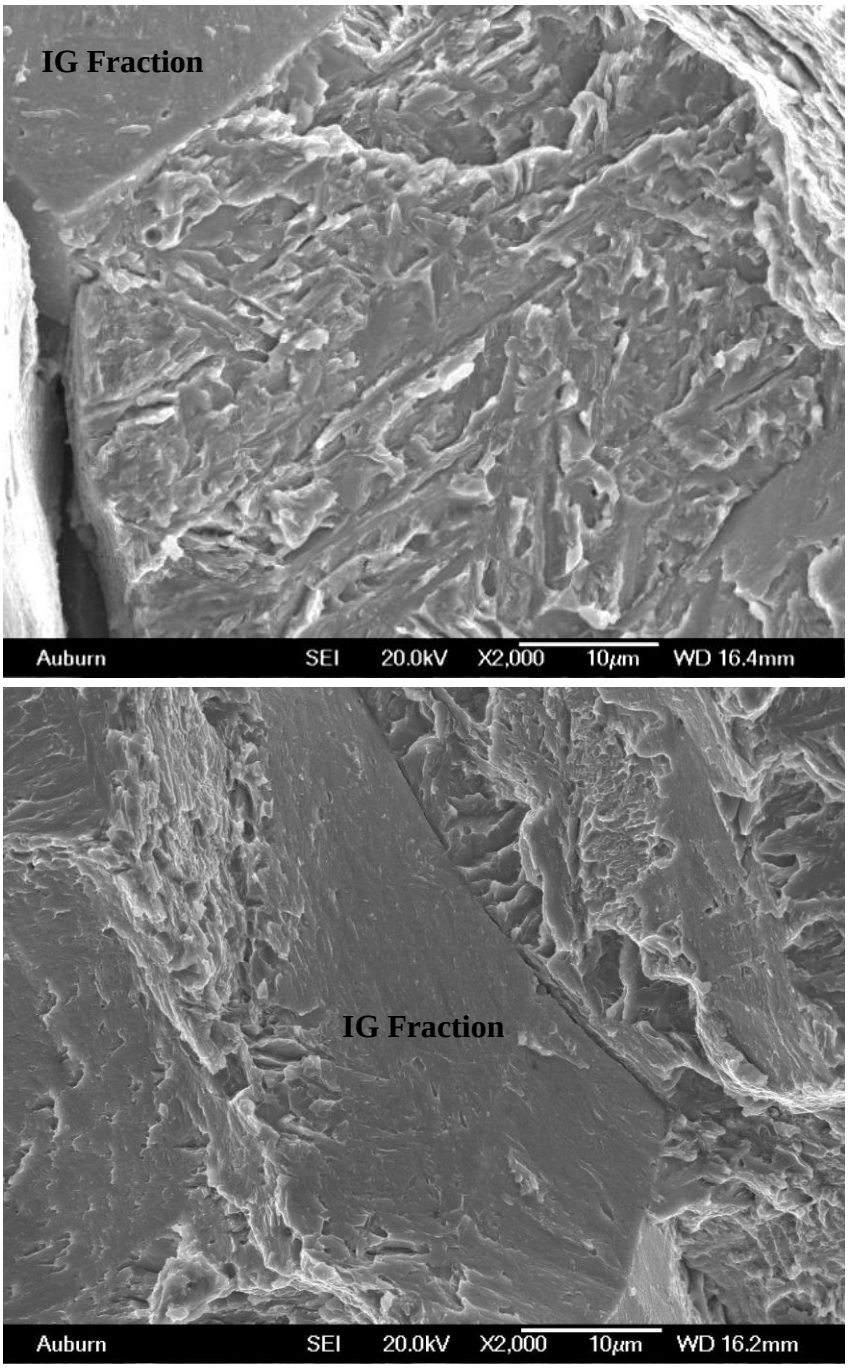

Fig. C-7 Typical quasi-cleavage features and smooth surfaces associated to it for 40 µm 43 HRC 40 min hydrogenated sample. CHS : 0.01 mm/min.